

# General Design of a Solar Thermal Power Plant

## 3.1 POWER PLANT DESIGN POINT

### 3.1.1 Significance of Design Point

Design point is a primary parameter in concentrating solar power (CSP, also known as solar thermal power) plant design and can be referred to when defining the area of the concentration field, thermal receiver capacity, thermal storage capacity, the rated capacity of the power generator unit, and the power plant's annual power output, as well as other key parameters such as the efficiencies of various equipment. The definition of design point is explained in detail in the chapter 1.2.3 of this book.

### 3.1.2 Calculation Examples of Applying the Design Point

Design point is related to the longitude and latitude of the power plant, annual mean ambient air temperature, local annual mean wind speed, annual mean solar direct normal irradiance (DNI), and other natural conditions. Normally, CSP plant design requires taking the solar time midday on typical days, such as the spring equinox, autumnal equinox, or summer solstice, during a typical year as the time mark for the design point. The Badaling CSP plant in China has a power generation capacity of 1 MW, which means that its power generation capacity at the design point is 1 MW.

Energy balances for various system units at the design point are shown in [Table 3.1](#).

TABLE 3.1 Energy Balances at Design Point for the Badaling Power Tower Plant

S/N	Item	Input Power (kW)	Loss (kW)	Residual (kW)	
1	Solar DNI Input in the heliostat field at the design point	10,000			
2	Concentration process: Shading and blocking, cosine effect, specular reflectance, atmospheric transmission loss, receiver intercept factor	10,000	3500	6500	
3	Thermal receiver process: Reflection, convection, radiation, thermal conduction	6500	1300	5200	
4	Thermal storage process: Thermal dissipation loss, thermal charging and discharging loss			(Not used)	
5	Transmission process	5200	90	5110	
6	Stream turbine working: Steam thermodynamic cycle loss, thermal dissipation	5110	4045	1065	
7	Self-dissipation loss: Consumption and loss of auxiliary system (rated operational conditions)	1065	Steam turbine 20  Concentration field and communication 20  DCS 5  Cooling tower pump 60  Others (high pressure feed pump, industrial water pump, feed booster pump) 50	155	910
8	Power plant net output			910	

## 3.2 HELIOSTAT FIELD EFFICIENCY ANALYSIS FOR POWER PLANTS

Under conditions corresponding to the design point, the energy flow of various system parts shall be balanced and calculated by applying the calculation method for the Yanqing (Badaling) 1 MW power plant as shown in [Table 3.1](#). According to [Table 3.1](#), solar concentration losses in the heliostat field rank second-largest among all losses and are caused primarily by cosine and interception errors. Cosine loss can be determined from the relationship between solar position and the concentrating field. Software currently available for calculating concentrating field efficiency for a solar tower power plant includes WinDELSOL, heliostat optical code (HOC) [18,19], and Fiat Lux.

The optical efficiency of the solar tower concentrator is important to the thermal performance of the entire solar tower collector. The aperture plane of a cavity receiver, and the (inner or external) absorbing surface of any central receiver, are key interfaces of energy flux. So it is necessary to simulate and analyze the concentrated time-changing solar flux density distributions on the flat or curved receiving surface of the collector with the main optical errors considered. The transient concentrated solar flux on the receiving surface is the superimposition of the flux density distributions of all normal working heliostats in the field.

### 3.2.1 Brief Introduction to Heliostat Optical Code for Solar Towers

HOC is a solar tower optics code developed by the Institute of Electrical Engineering, Chinese Academy of Sciences (IEE-CAS) that can be used for the layout and optimization design of heliostat fields and for optical performance analysis of partial and full heliostat fields on receiver apertures. HOC was developed with MATLAB and can be used for both cavity and external cylinder receivers. HOC is based on new backward ray tracing (BRT) and shading-and-blocking methods to simulate the transient concentrated solar flux on the receiving surface for a solar tower power plant [18,19].

### 3.2.2 Algorithmic Principles of Heliostat Optical Code

HOC uses the BRT method combined with the lumped effective solar cone to simulate the flux density map on the receiving surface. For BRT, bundles of rays are launched at the receiving-surface points of interest, strike directly on the valid cell centers among the uniformly sampled mirror cell centers in the mirror surface of the heliostats, and are then

directed to the effective solar cone around the incident sun beam direction after reflection. All optical errors are convoluted into the effective solar cone. The brightness distribution of the effective solar cone is here assumed to be circular and Gaussian. The mirror curvature can be adequately formulated using a certain number of local normal vectors at the mirror cell centers of the heliostat.

The principle of the BRT method coupled with the effective sun-shape (solar cone brightness distribution) is schematically illustrated by Fig. 3.1.

In Fig. 3.1, (O; North-East-Height) is the global coordinate system,  $\vec{s}_c$  is the unit solar vector,  $\vec{w}$  is the target surface normal at the target surface center  $T_0$ ,  $(u_j, v_j, w_j)$  are the coordinates of point  $T_j$  in the target surface coordinate system  $[T_0; \vec{u} - \vec{v} - \vec{w}]$ ,  $\vec{p}_j$  is the unit normal vector of target surface at point  $T_j$ ,  $(x_i, y_i, z_i)$  are the coordinates of the center point  $M_i$  of the  $i$ th mirror surface element in the mirror surface coordinate system  $[M_0; \vec{x} - \vec{y} - \vec{z}]$ ,  $\vec{n}_i$  is the mirror surface normal at the  $i$ th mirror point  $M_i$ ,  $-\vec{r}_i$  is the unit vector of the backward ray from target point  $T_j$  to mirror point  $M_i$ ,  $\vec{s}_i$  is the reflection unit vector for  $-\vec{r}_i$  after being reflected at point  $M_i$ , and the radial brightness distribution of the effective solar cone can be denoted as  $\phi_{eff}(\cdot)$  in  $\text{kW}/(\text{m}^2 \cdot \text{sr})$  integrated with  $\phi_{eff}(\cdot)$  over the full solid angle range equal to the value of DNI in  $\text{kW}/\text{m}^2$ . Following the denotations in Fig. 3.1, the concentrated solar flux density at the target surface point  $T_j(u_j, v_j, w_j)$  is  $F(u_j, v_j, w_j)$ . Here,  $\Delta x_i \Delta y_i$  and  $\rho_{m,i}$  are the area and specular reflectance of the  $i$ th mirror surface element,  $L_i$  is the distance from target point  $T_j(u_j, v_j, w_j)$  to mirror surface

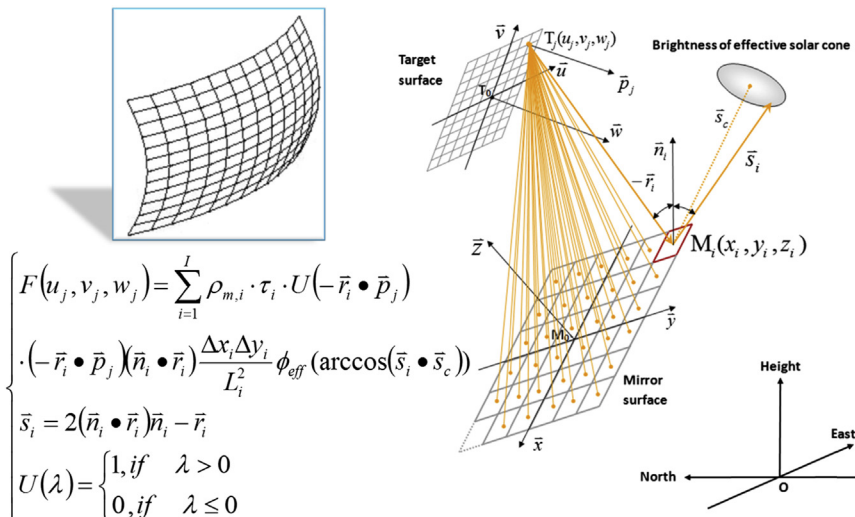


FIGURE 3.1 Principle of backward ray tracing to simulate the concentrated flux densities on the target surface.

point  $M_i(x_i, y_i, z_i)$ , and  $\tau_i$  is the absorptivity (absorption ratio) of the receiving surface. In Fig. 3.1, the grid element of the mirror surface at the lower corner marked with dotted lines is invalid, possibly due to shading and blocking by neighboring heliostats or the solar tower.

Fig. 3.1 schematically shows the BRT method's ray trace principle on the mirror surface plane and the target plane for simulating concentrated solar flux density at target surface point  $T_j(u_j, v_j, w_j)$ , but the equation shown in Fig. 3.1 is simply the general expression for the BRT method, with mirror surface normal  $\vec{n}_i$  changing with mirror point positions and the target surface normal  $\vec{p}_j$  changing with target surface positions.

Since the shading-and-blocking computation is the most complicated, time-consuming, and important optical computing section for the concentrated solar flux map on the receiving-surface for a field of heliostats, we also developed a new shading-and-blocking method to compute the shading-and-blocking factors (efficiencies) of all heliostats given a time or sun position in the sky. The shading-and-blocking mirror region of a heliostat by neighboring heliostats and solar tower shading on the heliostat mirror are all computed using a flat-ground-plane platform; i.e., the mirror contours and the envelope cylinder of the tower are projected onto the horizontal ground plane along the sunbeam incident direction or in the directions of the reflection. If the shading projection of a sampled mirror point of the current heliostat is inside the shade cast by a neighboring heliostat or in the shade cast by the tower, that mirror point should be shaded from the incident sun beam.

Fig. 3.2 illustrates the new model for identifying the invalid shading-and-blocking mirror region of a heliostat by neighboring heliostats and also the solar tower. The shading-and-blocking mirror region of a heliostat by neighboring heliostats and also the solar tower shading on the heliostat mirror are all computed on a flat-ground-plane platform; i.e., projecting the mirror contours and envelope cylinder of the tower onto the horizontal ground plane along the sunbeam incident direction or along reflection directions. In Fig. 3.2, the shading-and-blocking projections on the horizontal ground plane of the heliostat and solar tower contours are drawn with dashed lines. Fig. 3.2A shows the orientations of all normal-working heliostats around the circle cylinder solar tower marked in red given a solar vector, whereas the current heliostat, and the incident and reflected solar rays by the heliostat surface center, are marked with green lines. In this imaginary case, the field ground slopes from north to south. Fig. 3.2B shows the shading projections for all heliostat contours (including the current heliostat marked in green) and the solar tower cylinder contour together with heliostat plan positions. Fig. 3.2C shows the reflection-blocking projections for all heliostat contours (including the current heliostat marked in green) together with the heliostat plan positions. Fig. 3.2D is the partial enlarged drawing of Fig. 3.2B, in which the

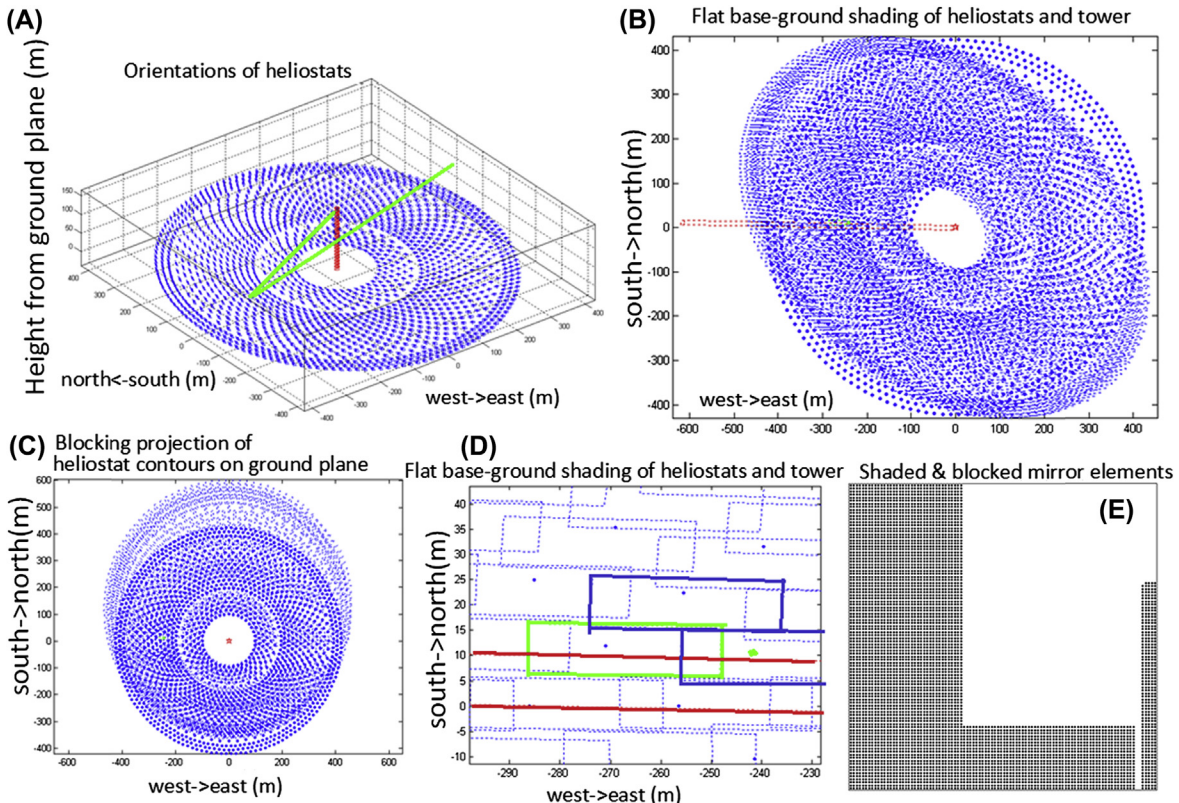


FIGURE 3.2 Illustration of the flat-ground-plane projection model for identifying a Heliostat's Shading-and-Blocking mirror region caused by neighboring heliostats and the solar tower shading region of the heliostat mirror.

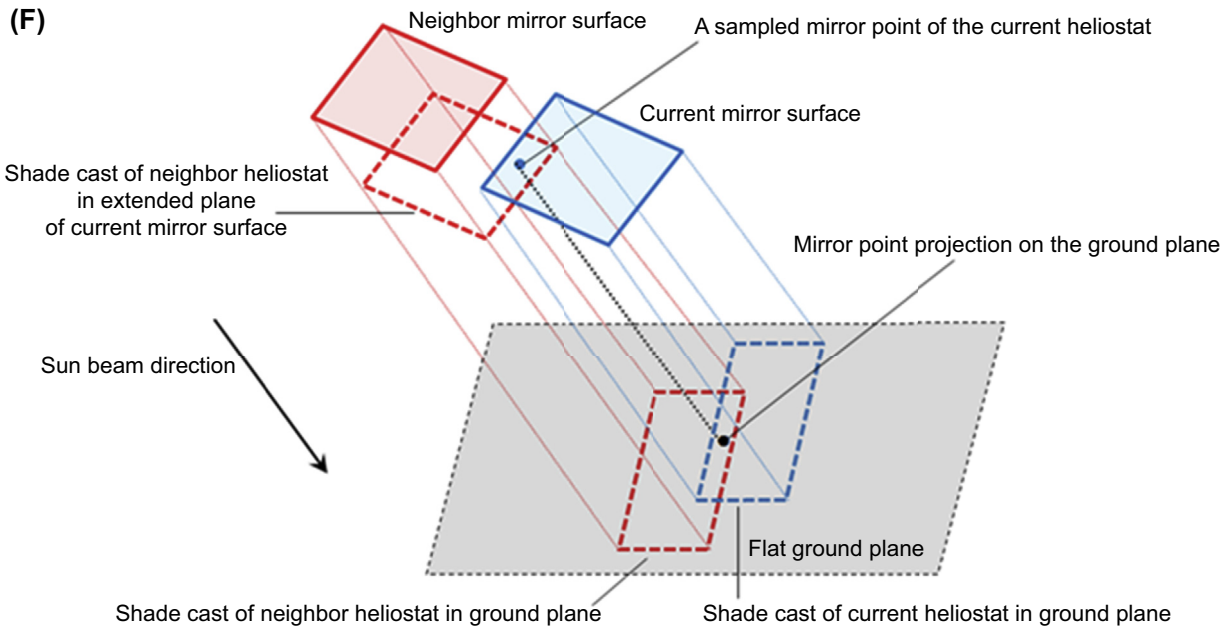


FIGURE 3.2 cont'd.

shadow of the current heliostat contour on the horizontal ground plane overlaps with the shadows from the two neighboring heliostats and the shadow of the solar tower. The current heliostat and its neighboring heliostats are marked by green dots and lines, and the tower is marked by red dots and lines. Fig. 3.2E marks the shaded mirror region of the current heliostat by neighboring heliostats and the solar tower.

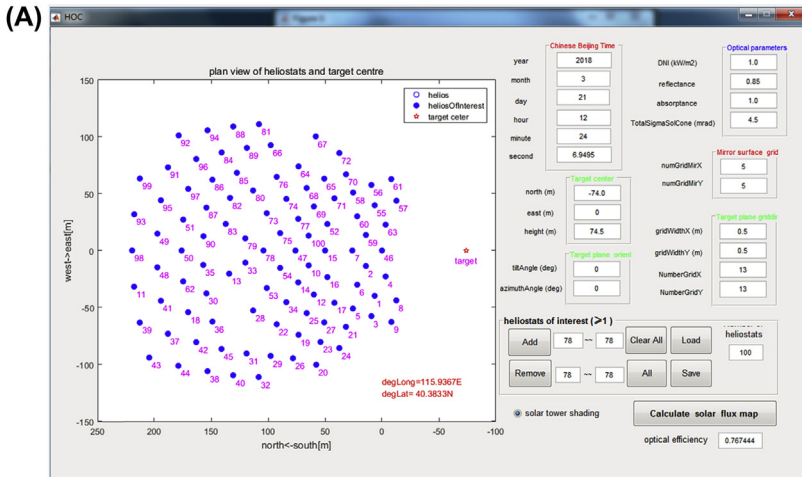
Fig. 3.2F shows the geometric topological invariance of a mirror point of the current heliostat inside the shade cast by a neighboring heliostat under shading projection from the mirror surface plane to the flat ground plane. If the shading projection of a sampled mirror point of the current heliostat is shaded by a neighboring heliostat or the tower, the mirror point should be shaded from the incident sun beam, i.e., if a mirror point of the current heliostat is shaded by a neighboring heliostat, the shading projection of the mirror point is in the intersection of the shade regions of the current heliostat and the neighboring heliostat in the flat ground plane, as Fig. 3.2F shows.

### 3.2.3 Two Specific Versions of Heliostat Optical Code

HOC based on the BRT and new shading-and-blocking methods for a solar tower power plant was developed using MATLAB, as Fig. 3.3 shows. The following two versions of HOC are for the cavity receiver and cylinder receiver, respectively.

Fig. 3.3A–D show the specific version of HOC for the DAHAN solar tower power plant in Beijing. There are 100 azimuth-elevation tracking heliostats in the solar field, and the total tower is 118 m high. The mirror surface of the heliostats is 10 m wide and 10 m long; it is composed of 8 rows  $\times$  8 columns of square mirror facets, and each mirror facet is 1.25 m  $\times$  1.25 m. The target center is 74.5 m higher than the ground plane.

Fig. 3.3E–G show the cylinder central receiver solar field layout (CCRSFL) version of HOC. A CCRSFL adopts the traditional radial-staggered pattern layout for a heliostat field. In CCRSFL, given the parameters of tower height, heliostat size, and receiver size, the heliostats are initially arranged as a compact circular field with sufficient total mirror area; then the heliostat field grows gradually by increasing the radial spaces between adjacent heliostat rings during the optical optimization process. The optimizing objective function collects the maximum annual solar energy from the receiver aperture. After first-stage optimization of solar field layout, the solar field is trimmed by selecting the needed number of heliostats that have higher annual optical efficiencies. The trimmed heliostat field is optimized further through a second stage similar to the first. CCRSFL can efficiently simulate the concentrated solar flux map of heliostats on the receiving surface using only a pair of cross-



**(B)** heliostat facets(front view): $1.25\text{m} \times 1.25\text{m}$  per facet

*8	*7	*6	*5	*4	*3	*2	*1
*16	*15	*14	*13	*12	*11	*10	*9
*24	*23	*22	*21	*20	*19	*18	*17
*32	*31	*30	*29	*28	*27	*26	*25
*40	*39	*38	*37	*36	*35	*34	*33
*48	*47	*46	*45	*44	*43	*42	*41
*56	*55	*54	*53	*52	*51	*50	*49
*64	*63	*62	*61	*60	*59	*58	*57

**(C)**

orientations of heliostats ( month3day21hr12.4019 )

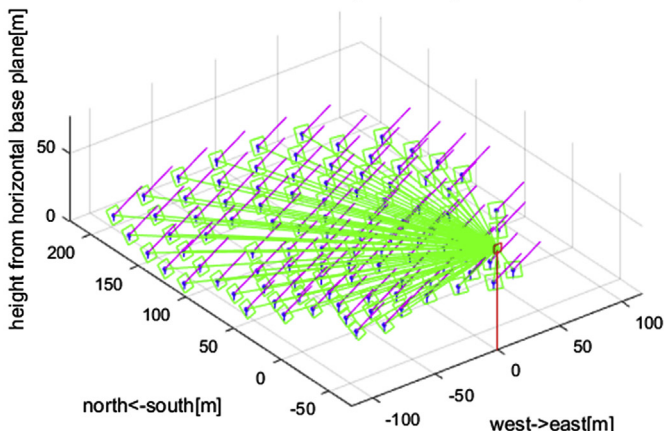


**FIGURE 3.3** Two versions of heliostat optical code (HOC) for the cavity receiver and the cylinder receiver respectively: (A) interface of the specific version of HOC for the DAHAN solar tower power plant in Beijing with data loaded for all 100 heliostats, (B) arrangement of mirror facets for a  $100\text{-m}^2$  DAHAN heliostat, (C) light path drawing of all DAHAN heliostats at the solar noon of the spring equinox, (D) simulation of the concentrated solar flux image on the horizontally north facing target plane by all DAHAN heliostats at the solar noon of spring equinox, (E) interface of cylinder central receiver solar field layout version of HOC with field data loaded, (F) simulated solar flux density on the cylinder receiver surface from all heliostat fields with respect to given parameter settings, and (G) efficient HOC simulation of the concentrated solar flux map of heliostats on the receiving surface using only a pair of cross-flux-density profiles to reconstruct a flux density map of the elliptical Gaussian type.

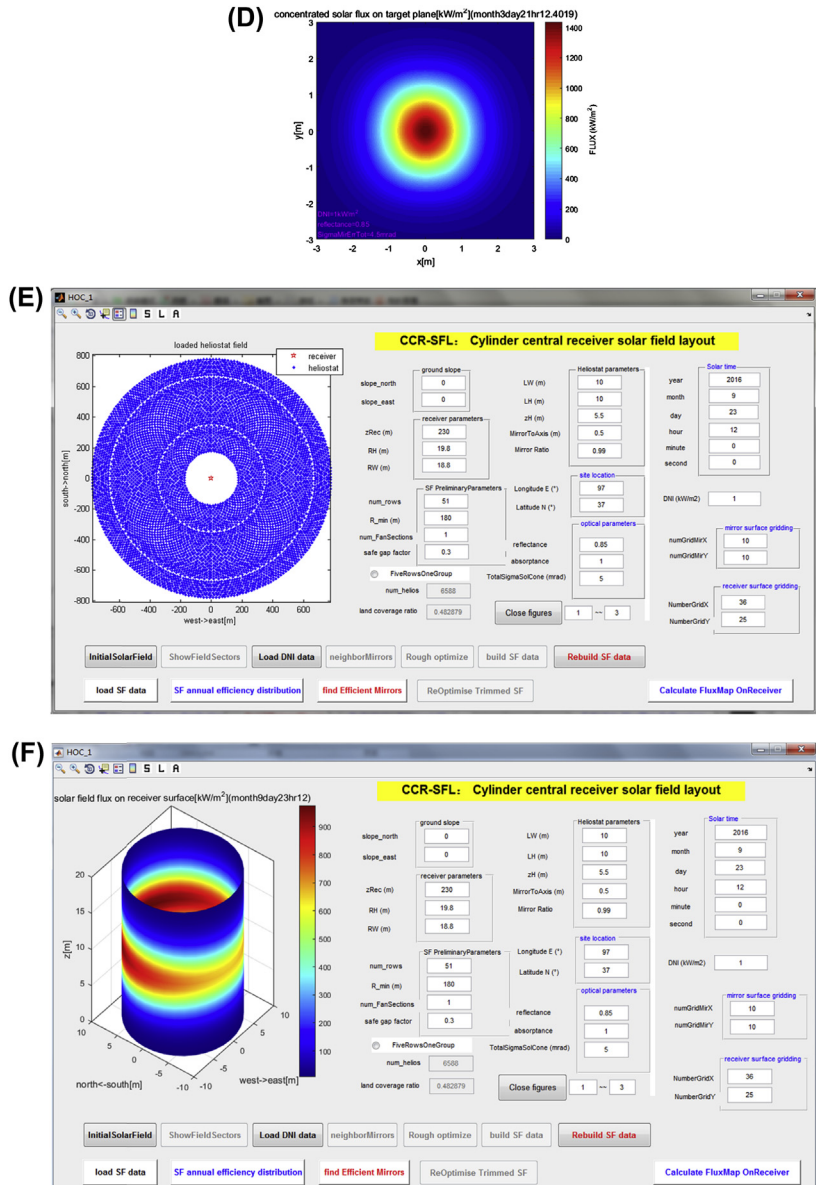


FIGURE 3.3 cont'd.

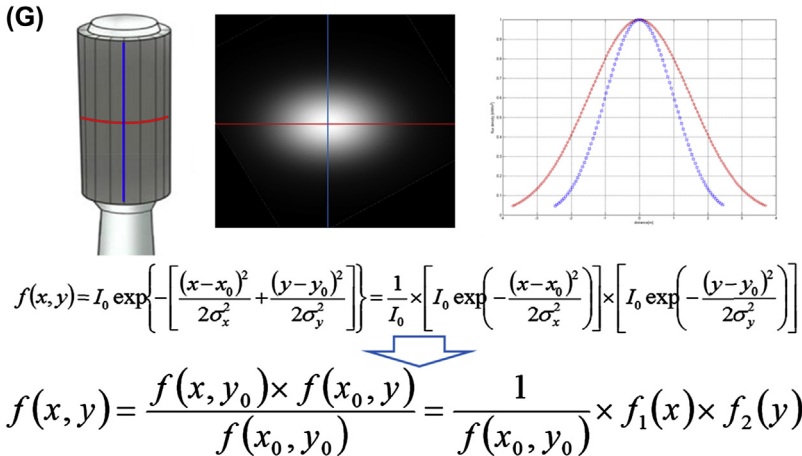


FIGURE 3.3 cont'd.

flux-density profiles to reconstruct a flux density map not limited to the elliptical Gaussian type, as Fig. 3.3G shows. Fig. 3.3E and F show a typical calculation example of cylinder receiver flux density distribution at the solar noon of the autumnal equinox.

Fig. 3.3F shows the mathematical principle of flux map reconstruction using a pair of cross-flux-density profiles along the X and Y axial directions.  $f(x, y)$  is the flux density function over the X-Y receiving surface, where  $(x_0, y_0)$  is the coordinate pair of the peak value, and  $\sigma_x$  and  $\sigma_y$  are the standard deviations along the X and Y axes.  $I_0 = f(x_0, y_0)$  represents the peak flux value at point  $(x_0, y_0)$ .  $f(x, y_0)$  and  $f(x_0, y)$  are the flux density profiles passing through point  $(x_0, y_0)$  along the X and Y axes, respectively. Thus HOC can efficiently simulate the concentrated solar flux map  $f(x, y)$  on the receiving surface with just the flux density values of the X and Y flux-density profiles and then using them to reconstruct the flux density map.

### 3.2.4 Values of Specular Reflectance

The value of specular reflectance has a direct impact on energy calculations. Normally, all values are taken at the design point when mirrors are clean and fall in a range of 92%–94% [20].

However, when calculating annual energy for a power plant in an area with significant sand dust, the effect of dust accumulation on the mirror must be considered. Generally speaking, in a season with a large amount of dust, heliostat reflectance drops by 0.8% per day [20]. When functioning by facing upward to the sky, the reflectance of a parabolic trough

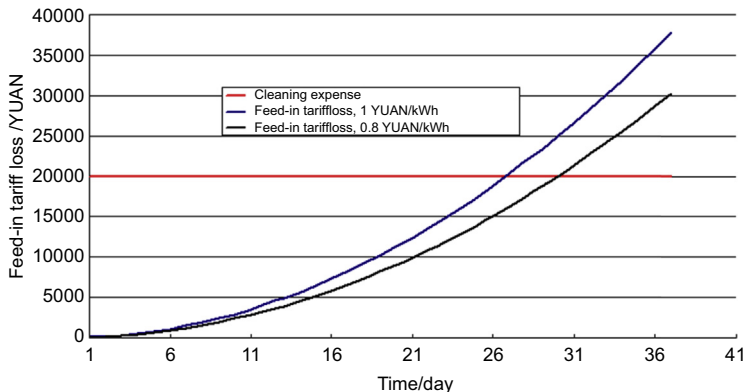


FIGURE 3.4 Defining the mirror cleaning time.

reflective surface may drop even faster. In the case of cleaning the mirror twice a month, it is more appropriate to take a value of about 83% as annual mean reflectance.

The ratio of cleaning times, energy loss, and paid cleaning expense shall be calculated. Currently, the cleaning expense for each square meter of mirror is about 2 yuan. For a heliostat concentration field of 10,000 square meters, the respective cleaning expense would be 20,000 yuan. The daily loss of reflectance of the mirror is 0.8%. When the expense of power loss exceeds the concentration field cleaning expense, the cleaning process shall start. Fig. 3.4 indicates the cleaning time defined by the intersection of the mirror cleaning expense and economic loss caused by power attenuation from dust accumulation loss.

Assuming the feed-in tariff of an CSP plant is 1 yuan/kWh, the cleaning time indicated in Fig. 3.4 approximates 27 days. Obviously this value changes according to the cleaning costs, daily dust accumulation status, and feed-in tariff of the power plant. After the mirrors are cleaned, reflectance bounces back to 94% from 72.4%.

Assuming the feed-in tariff of the CSP plant is 0.8 yuan/kWh, the cleaning time indicated in Fig. 3.4 approximates 30 days.

### 3.2.5 Atmospheric Transmittance Analysis

Atmospheric transmittance is related to the degree of local sand blow. Due to the short focal distance of a parabolic trough collector, it is not necessary to consider transmittance. However, for a large-scale power tower plant, this factor must be considered.

During transmission of optical waves in the atmosphere, absorption and scattering of atmospheric gas molecules and aerosols may result in

energy attenuation of the solar beam, and the nonuniform air refractive index may result in the variation of amplitude and phase of the optical wave. When the power of the optical wave is large enough and lasts for an extremely short time, the nonlinearity effect may also influence the characteristics of solar beams.

The integrated effects of absorption and scattering results in attenuation of the radiant intensity of transmitted light. Partial energy of incident light is converted into other forms of energy through absorption (such as thermal), and partial energy deviates from its original direction due to scattering (namely spatial reallocation of radiation energy).

Monochromatic radiation with intensity is assumed to pass through a thin atmospheric layer with thickness  $dl$ . Without considering nonlinearity effects, optical intensity attenuation  $dI$  is proportional to  $I$ , namely

$$\frac{dI}{I} = \frac{I' - I}{I} = -\beta dl \quad (3.1)$$

Atmospheric transmittance can be obtained through integral calculus

$$T = \frac{I}{I_0} = \exp \left( - \int_0^L \beta dl \right) \quad (3.2)$$

$$T = \exp(-\beta L) \quad (3.3)$$

in which  $\beta$  is the atmospheric extinction coefficient,  $l/\text{km}$ , and  $L$  refers to the transmission distance of solar radiation, km.

This is Lambert's law for describing atmospheric attenuation, which manifests the exponential law of decreased optical intensity with increases in transmission distance.

As extinction coefficient  $\beta$  describes the influences of the two independent physical processes of absorption and scattering on the radiant intensity of transmitted light,  $\beta$  can be manifested as

$$\beta = k_m + \sigma_m + k_a + \sigma_a \quad (3.4)$$

in which  $k_m$  and  $\sigma_m$  are molecular absorption and scattering analysis coefficients separately, and  $k_a$  and  $\sigma_a$  are absorption and scattering coefficients of aerosols in the atmosphere.

Research on atmospheric attenuation can be summarized as studies of the four basic attenuation parameters mentioned above. When applying, the commonly used unit for  $\beta$  is either  $\text{L}/\text{km}$  or  $\text{dB}/\text{km}$ , and the conversion relationship is

$$\beta(\text{dB}/\text{km}) = 4.343 \times \beta(\text{L}/\text{km}) \quad (3.5)$$

1. Molecule absorption. Atmospheric molecules polarize under the influence of the optical wave electric field and perform forced vibrations on the frequency of incident radiation. Thus in order to overcome the internal resistance of atmospheric molecules, energy is consumed and takes the form of absorption of atmospheric molecules.

Molecular absorption characteristics strongly rely on the frequency of radiation wavelength. The inherent absorption frequency of a molecule is determined by its internal motion modality. The internal motion of a polar molecule normally consists of the electronic motion within the molecule, vibration of atoms that compose the molecule, and rotation of molecules surrounding the center of mass. The respective resonant absorption frequencies correspond to the ultraviolet, visible light, near-infrared, intermediate-infrared, and far-infrared regions of the optical wave.

Although N<sub>2</sub> and O<sub>2</sub> molecules take up the largest share of the atmosphere (about 90%), their visible light and infrared regions show hardly any absorption, and then only show significant absorption toward far-infrared and microwave bands. Thus within the visible light and near-infrared regions, the effects of absorption are normally not considered.

Except for the above molecules, the atmosphere also contains He, Ar, Xe, O<sub>3</sub>, Ne, and so on. All these molecules have considerable absorption spectral lines in the visible light and near-infrared regions; however, due to their insignificant amount in the atmosphere, the respective effect of absorption is normally also not considered. Only when the remaining attenuation factors are already quite weak above the sky is the absorption effect considered. For a tower power plant, the influences of molecular absorption are not considered.

H<sub>2</sub>O and CO<sub>2</sub> molecules also play a certain role in the absorption of solar radiation. In special cases, the H<sub>2</sub>O molecule has a broad vibration—rotation and sole-rotation structure within the near-infrared region, and thus the H<sub>2</sub>O molecule acts as the most important absorption molecule in visible light and near-infrared regions and serves as the main cause for optical attenuation of the atmosphere on clear days. The central wavelengths of some major absorption spectral lines of H<sub>2</sub>O molecules are as follows: 0.72, 0.82, 0.93, 0.94, 1.13, 1.38, 1.46, 1.87, 2.66, 3.15, 6.26, 11.7, 12.6, 13.5, and 14.3  $\mu\text{m}$ .

For certain specific wavelengths, the atmosphere may present extremely intensive absorptions that optical wave can barely pass through. Solar radiation wavelength bands applied by CSP generation are mainly below 3  $\mu\text{m}$  and greatly overlap with the

above parts. Thus in the power tower plant with concentrators located far away from the receiver, influences of atmospheric humidity on radiation transmission shall be considered. It is suggested not to build up large-scale power tower plants in areas with high atmospheric humidity.

2. Molecule scattering. There is always the statistical deviation of partial density from the mean density in the atmosphere, which is known as the density fluctuation. It ruins the optical uniformity of the atmosphere; partial solar radiation light will transmit toward other directions, which leads to the scattering of the solar radiation in various directions.

In visible light and near-infrared wave regions, radiation wavelength is always much greater than molecular dimensions. Under such conditions, scattering is referred to as the Rayleigh scattering. The intensity of Rayleigh scattering light is inversely proportional to the biquadratic value of wavelength  $\lambda$ . The empirical equation of Rayleigh scattering coefficient is:

$$\sigma_m = 0.827 NA^3 / \lambda^4 \quad (3.6)$$

in which  $N$  refers to the quantity of molecules within a unit volume,  $\text{cm}^{-3}$ ;  $A$  refers to the molecular scattering section,  $\text{cm}^2$ ;  $\lambda$  refers to the length of the optical wave, cm. The bigger of wavelength  $\lambda$ , the weaker of the scattering effect; the smaller of  $\lambda$ , the stronger of the scattering effect.

When encountering atmospheric molecules or aerosols particles, the optical wave will interact with them and once again emit the light (called wavelet) of the same frequency and less intensity with the incident light in all directions, which is referred to as the optical scattering. The wavelet is called the scattering radiation; atmospheric molecules and aerosol particles that receive the original incident light and emit wavelets are called scattering particle. When scales of scattering particles are much smaller than the wavelength of incident light (for example, scattering effect of atmospheric molecules on visible light), it is called molecular scattering or Rayleigh scattering, in which scattering lights have been distributed on an even and symmetric basis.

As molecular scattering is inversely proportional to the biquadratic value of wavelength, the bigger of the  $\lambda$ , the weaker of the scattering effect; and the smaller of the  $\lambda$ , the stronger of the scattering effect, scattering effect of visible light is stronger than that of infrared light, and scattering effect of blue light is stronger than that of red light. In a clear sky, other particles are insignificant in content; thus Rayleigh scattering has been playing a dominant role.

In addition, as the scattering effect of blue light is the strongest, a clear sky is normally blue-colored.

3. Attenuation of atmospheric aerosols. Definition of atmospheric aerosols: There is a large amount of solid and liquid particles in the atmosphere with the size between 0.001 and 10  $\mu\text{m}$ . They are mostly dusts, soot deposits, water droplets, sized salts, organic microbes, etc. As they are suspended in a gel state in the atmosphere, these particles are normally called atmospheric aerosols. As a major factor for influencing climate change, atmospheric aerosols have aroused widespread attention from the world scientific circle, which mainly include six categories of seven types of aerosol particles. Sand dust aerosols or so-called mineral aerosols are the main components of troposphere aerosols. China's sand dust aerosols mainly come from deserts in Xinjiang, Gansu, Inner Mongolia, Loess Plateau and other arid and semiarid areas. Recently, frequent sandstorms in North China have aroused broad attention from both home and abroad. Sandstorm has turned into a major environmental problem of the Earth. Sizes of atmospheric aerosol particles are distributed on a very complex basis, and are greatly influenced by climate variation as well. Maximum values of concentration and dimension (diameter) of atmospheric aerosol particles corresponding to different types of weather have been listed in [Table 3.2](#).

Optical wave attenuation of atmospheric aerosols includes aerosol scattering and absorption (refer to [Fig. 3.5](#)). Sizes of the

TABLE 3.2 Physical Parameters of Haze, Cloud, and Precipitation

Weather Type	$N/\text{cm}^{-3}$	$a_{\max}/\mu\text{m}$	Type of Atmospheric Aerosols
Haze, M	100	3	Maritime or coastal aerosols
Haze, L	100	2	Territorial aerosols
Haze, H	100	0.6	High-altitude or stratosphere aerosols
Rain, M	100	3000	Drizzle or moderate rain
Rain, L	100	2000	Heavy rain
Hail, H	10	6000	Hail containing a large number of small particles
Cumulus cloud, C.1	100	15	Cumulus cloud or stratus cloud, mist

$N$  refers to particle concentration,  $a_{\max}$  represents the maximum diameter of particle.

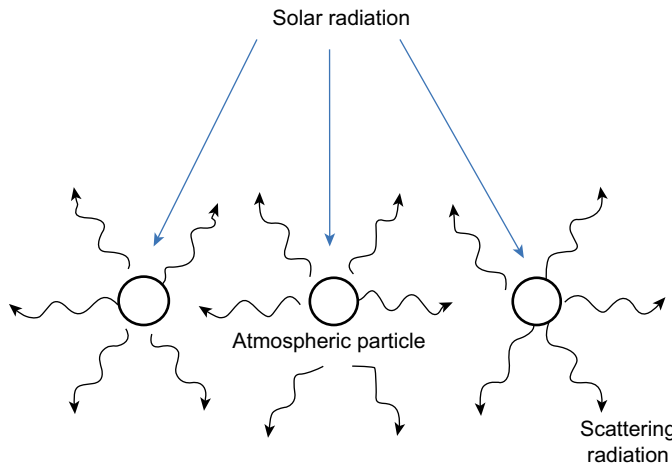


FIGURE 3.5 Atmospheric aerosol attenuation.

sand dust particles correspond to visible light and near-infrared light, which shall be handled by applying the Mie-Debye scattering theory. The Mie-Debye scattering, on the other hand, mainly relies on various characteristics, like the size of the scattering particle, density distribution and refractive index; the relationship between it and the wavelength is much less intensive than the relationship with Rayleigh scattering (which can be approximately deemed as irrelevant to wavelength).

According to the IPCC report, the mean life of sand dusts is about 4 days, the mean column-perpendicular integral content is about  $32.2 \text{ mg/m}^2$ , and the mass extinction coefficient when wavelength is  $0.550 \mu\text{m}$  is  $0.7 \text{ m}^2/\text{g}$ . Based on the research analysis results, particles within a range of  $0.1\text{--}1.0 \mu\text{m}$  are the main light extinction particles. NIU Shengjie et al. entered into desert sources (Tengger Desert, Badain Jaran Desert, Mu Us Desert) during April to May every year from 1996 to 1999, and conducted systematic observations toward the sand dust weather; by utilizing a plane to observe atmosphere aerosols in desert areas, they also systematically analyzed the microstructure of sand dust aerosols in Helan Mountains. ZHANG Wenyu et al. conducted the ground multiwave band solar radiation observations in Shapotou Station in Tengger Desert during April to September 2001. According to their research, optical thickness of local atmospheric aerosols varied significantly under different weather conditions. On April 6, 2000, during the catastrophic sandstorm, according to the analysis on sand dust particles, concentration of coarse particles ( $d > 2 \mu\text{m}$ )

during the sandstorm was more than 20 times of that after the sandstorm; whereas the concentration of fine particles ( $d < 2 \mu\text{m}$ ) is seven times that after the sandstorm. Optical thickness, extinction efficiency factor, scattering efficiency factor, and absorption efficiency factor of aerosols are major physical parameters to describe the conditions of atmospheric aerosols, as well as the crucial factors to evaluate the energy flow transmission of atmospheric concentration.

Extinction efficiency factor  $Q_e$  refers to the ratio of the light extinction section to geometric section of the respective particle. According to the Mie-Debye scattering theory, extinction efficiency factor  $Q_e$  has the important features of fluctuating along with the attenuation of sand dust particle radius  $r$  and approaching 2.

According to Fig. 3.6, position of the primary main peak of  $Q_e$  falls in a range of  $0.1\text{--}1.0 \mu\text{m}$ . Along with the increase of wavelength  $\lambda$ , position of the primary main peak moves toward the direction of the increase of  $r$ . According to the measured data from both home and abroad, it is exactly within the above-mentioned main peak area, in which aerosol spectrum normally has sharp peak values. However, along with the increase of particle radius  $r$ , variation amplitude of extinction efficiency factor gradually decreases; when  $r > 5.0 \mu\text{m}$ , the extinction efficiency factor  $Q_e$  gradually loses its sensitivity against the particle size  $r$ , and gradually approaches 2, that is, solar energy eliminated by large particles from the incident beam is exactly two times of the optical energy prevented by its section.

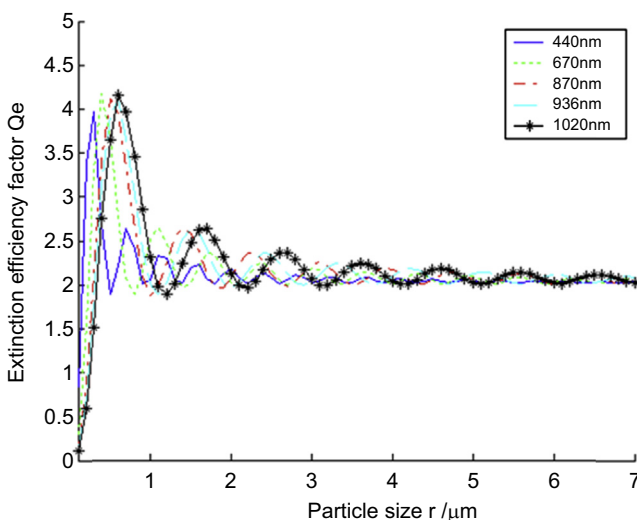


FIGURE 3.6 Variation of extinction efficiency factor  $Q_e$  over particle size  $r$ .

Scattering effect factor  $Q_s$  refers to the ratio of scattering section to the geometric section of the respective particle. Fig. 3.7 shows the variation rule of scattering efficiency factor  $Q_s$  over particle size  $r$ . Position of the primary peak value of  $Q_s$  also falls in a range of 0.1–1.0  $\mu\text{m}$ . Along with the increase of wavelength  $\lambda$ , position of the primary peak value moves toward the direction of the increase of  $r$ . When the particle size  $r$  is very small,  $Q_s$  is much smaller than 1, that is, the scattering ability of particles are much smaller than any energy projected onto its geometric section. Along with the increase of particle radius  $r$ ,  $Q_s$  also rapidly increases, and gradually approaches the maximum value of 4. When  $r > 4.0 \mu\text{m}$ , variation amplitude of  $Q_s$  gradually decreases and is slowly weakened in the form of damped oscillation while gradually approaching 1, that is, for large particles, scattering efficiency factor approaches 1. Such variation is caused by the absorption nature of particles.

Absorption efficiency factor  $Q_a$  refers to the ratio of absorption section to the geometric section of the respective particle. According to Fig. 3.8, based on the variation of absorption efficiency factor  $Q_a$  over particle size  $r$ ,  $Q_a$  gradually increases along with the increase of  $r$  and approaches 1; in addition, absorption features of particles vary according to different values of wave band  $\lambda$ , absorption ability at the wave band of 440 nm is obviously higher than those at other wave bands. Meanwhile, by integrating with Figs. 3.6 and 3.7, along with the growth of absorption, vibration of  $Q_e$  and  $Q_s$  curves gradually decreases until vanishing in the end.

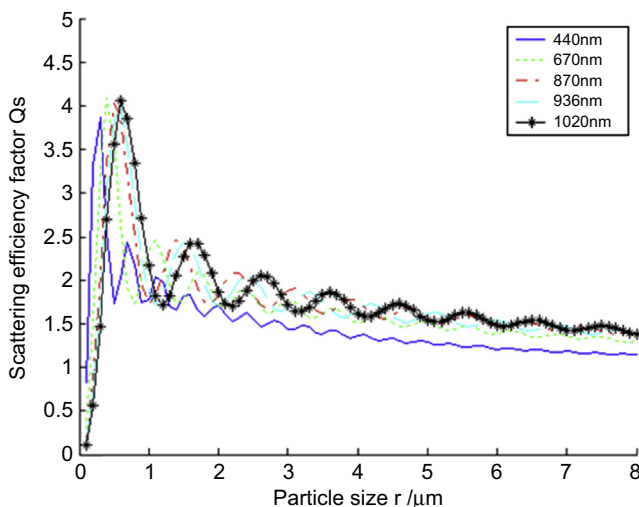


FIGURE 3.7 Variation of scattering efficiency factor  $Q_s$  over particle size  $r$ .

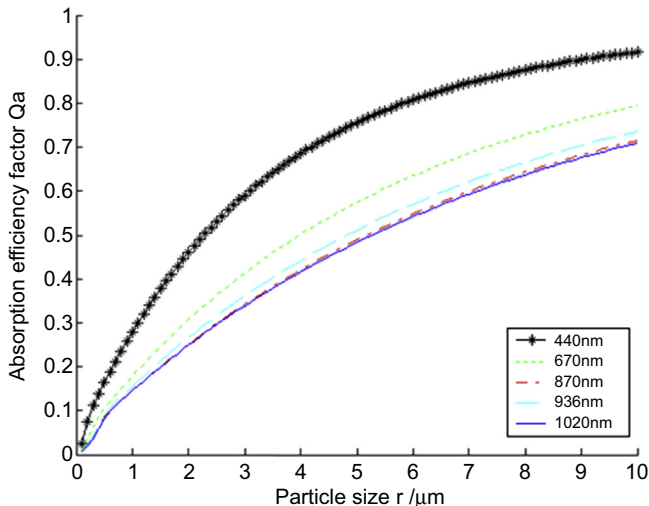


FIGURE 3.8 Variation of absorption efficiency factor  $Q_a$  over particle size  $r$ .

4. Extinction coefficient. Aerosol extinction coefficient is used to describe the degree of solar direct radiation being weakened by the atmosphere. Value of the coefficient is related to the category of aerosols and wave band of solar direct radiation; yet in general, the coefficient is comparatively stable.

[Fig. 3.9](#) offers contributions of differently sized particles to extinction coefficient, according to which, the overall extinction coefficient of all particles is proportional to the area below the curve,

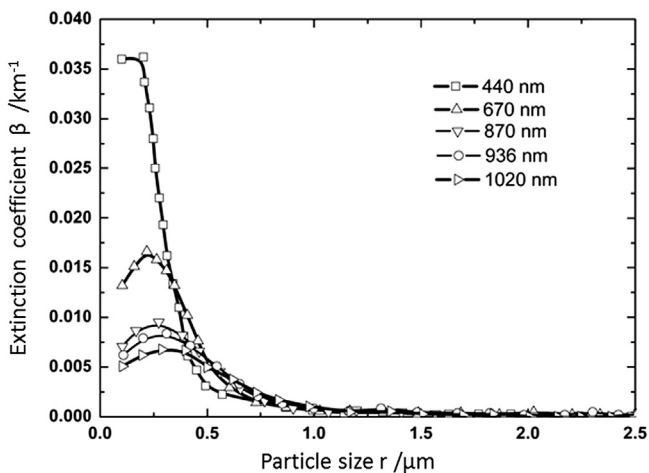


FIGURE 3.9 Variation of extinction coefficient  $\beta$  over particle size  $r$ .

and particles with the size of 0.1–0.4  $\mu\text{m}$  have the largest contributions to the total extinction coefficient; peak value of extinction appears when the particle size approximates 0.2  $\mu\text{m}$ ,  $\beta(440) = 0.36/\text{km}$ . Along with the increase of particle size, extinction coefficient decreases rapidly; when the particle size reaches up to 1.0  $\mu\text{m}$ , extinction coefficient has already approached 0. Then, based on the variation of extinction coefficient over wavelength, aerosol particle has the best extinction ability when the wavelength is 440 nm; along with the increase of wavelength, extinction ability of the particle gradually decreases; comparing with other wavelengths, the extinction coefficient decreases with a higher speed when wavelength is 440 nm. Yet at the same time, it is also discovered that the relationship between extinction coefficient and wavelength is not onefold, which can be concluded from 0.4 to 1.0  $\mu\text{m}$  section of the particle size curve. In this section of the particle size curve, curves of various wavelengths intersect with each other; there is no obvious law to follow. Many studies have indicated that variation of extinction coefficient over wavelength can normally be manifested as follows:

$$\beta = \frac{A}{r^\gamma} \quad (3.7)$$

in which  $A$  is a constant; index number  $\gamma$  may vary from 4 (suitable for Rayleigh scattering and extremely small-sized particles) to 0 (suitable for the scattering effect of mist on visible light or near-infrared light).

However, only for extremely large and extremely small particles, can such dependency relationship be manifested by a simple function within a comparatively broad wavelength range. Sand dust particles for a power plant fall in between these two extreme values. Based on the entire wavelength and particle size ranges, variation of extinction coefficient still follows a certain rule.

To sum up, extinction coefficient  $\beta$  in Eq. (3.4) is 0.02. For a 10 MW power plant, the last row of heliostats is located about 0.8 km away from the receiver tower. By substituting extinction coefficient and light transmission length  $L = 0.8 \text{ km}$  into Eq. (3.3), atmospheric transmittance of heliostat from the last row can be obtained:

$$T = \exp(-\beta L) = \exp(-0.02 \times 0.8) = 0.984 \quad (3.8)$$

The mean value is

$$T = \exp(-\beta L) = \exp(-0.02 \times 0.4) = 0.99$$

For a 100 MW-level power tower plant, area of the concentration field is about 1 million square meters. The last row of heliostats is 2 km away from the tower.

$$T = \exp(-\beta L) = \exp(-0.02 \times 2) = 0.96$$

### 3.2.6 Heat Losses of Power Tower Cavity Receiver

Receiver is the device in the CSP generation system that converts solar energy into thermal energy. Receiver of the power tower generation system is normally mounted at the top of the receiver tower. There are mainly two types of receivers, cavity type and cylinder type receivers. The cavity receiver is used to absorb the solar radiation collected by the concentration field arranged in northern sectors ([Fig. 3.10A and C](#)), whereas the cylinder receiver is used to receive solar radiation collected by the concentration field arranged in circles surrounding the receiver tower ([Fig. 3.10B](#)). Absorber of the cavity receiver is mounted within a cavity structure insulating thermal from outside; opening area of the cavity is less than the surface area of the absorber, which is able to effectively reduce heat loss of the absorber. A cylinder receiver is made by welding a large amount of straight tubes that are vertically parallel to each other on the instrument in order to create strip receiver plates, and put together the receiver plates in order to create an approximate cylinder. Bottom and top of the cylinder have been designed with heat-transfer fluid header for providing cold and hot transfer fluid to the receiver and collecting the thermal transfer fluid. According to different heat-transfer fluid inside the absorber, receivers for the power tower generation system can be categorized into synthetic oil receiver, water/steam receiver, molten-salt receiver, air receiver, liquid metal receiver, solid particle receiver, etc. According to different features of solar radiation absorption process inside the receiver, receivers for the power tower generation system can be categorized into volumetric receiver and tubular receiver. The volumetric receiver's absorber is normally made of honeycomb ceramics, foam ceramics, metal gauze, foam metal and other

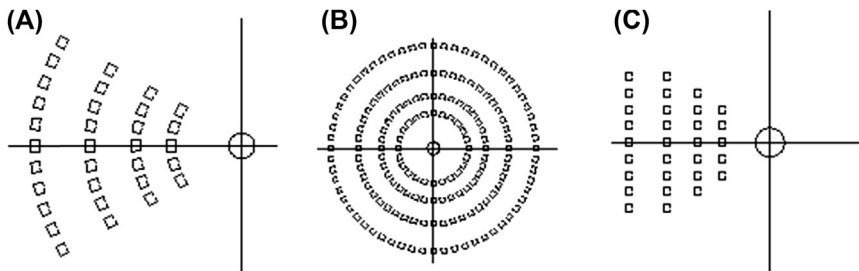


FIGURE 3.10 Various kinds of concentration fields and receivers.

porous materials. Solar radiation is transmitted and absorbed within the entire volume of absorber, which is frequently used together with the system that uses heat-transfer fluid as the gas. The tubular receiver consists of several pieces of tubes. Solar radiation will be absorbed on the surface of the absorber tube; interior wall of the tube exchanges thermal energy with the heat-transfer fluid flowing through the tube by the convection heat transfer, the heat-transfer medium of which is liquid in most of the cases.

For a cavity receiver, the heat loss  $P_{LOSS}$  can be calculated as follows [21]

$$P_{LOSS} = P_{REFCAV} + P_{RAD} + P_{CONV} + P_{COND} \quad (3.9)$$

in which  $P_{REFCAV}$  refers to the reflective radiation loss of the cavity receiver;  $P_{RAD}$  refers to the radiation heat loss from the surface of absorber inside the cavity receiver to the outside through receiver aperture;  $P_{CONV}$  refers to the thermal convection from the surface of absorber to the outside through receiver aperture;  $P_{COND}$  refers to the conductive heat loss from the surface of absorber to the outside heat loss.

The area of the cavity receiver is shown in Fig. 3.11.  $A_1$  is the aperture area of the receiver (unit:  $\text{m}^2$ ) and  $A_2$  is the area of inner absorbing surface of the receiver.

1. Reflective radiation loss  $P_{REFCAV}$  U<sub>marov</sub> (1983) equation, under the premise of the thermal absorbent surface being a gray body, the receiver's equivalent absorptance  $\alpha_{eff}$  is

$$\alpha_{eff} = \frac{\alpha_w}{1 - (1 - \alpha_w) \left( 1 - \frac{A_1}{A_2} \right)} \quad (3.10)$$

in which  $a_w$  is the solar absorptance on the surface of the absorber of the receiver, which can be measured through experiments and usually depend on the temperature.

Receiver's equivalent reflectance  $P_{COV}$  is

$$\rho_{COV} = 1 - \alpha_{eff}$$

$$= 1 = \frac{\alpha_w}{1 - (1 - \alpha_w) \left( 1 - \frac{A_1}{A_2} \right)} \quad (3.11)$$



FIGURE 3.11 Schematic diagram of the area of the cavity receiver.

$P_{AP}$  refers to the radiation flux through the receiver aperture after solar radiation is reflected by the concentration field.

$$P_{REFCAV} = \rho_{COV} P_{AP}$$

$$= \left( 1 - \frac{\alpha_w}{1 - (1 - \alpha_w) \left( 1 - \frac{A_1}{A_2} \right)} \right) P_{AP} \quad (3.12)$$

$P_{AP}$  can be obtained through some heliostat field simulation software, and corrected through experimental measurements.

In Eq. (3.12),  $\alpha_w$  is a constant that changes along with  $(A_1/A_2)$ . We assume  $\alpha_w = -0.85$ , and substitute it into Eq. (3.11)

$$\rho_{COV} = 1 - \frac{0.85}{1 - 0.15 \left( 1 - \frac{A_1}{A_2} \right)} \quad (3.13)$$

Fig. 3.12 displays the variation rule of reflectance, according to which, equivalent reflectance of cavity receiver is normally around 0.05.

In case that the area ratio  $(A_1/A_2)$  is a constant and  $\alpha_w$  changes accordingly, we assume  $A_1/A_2 = -0.2$ , and substitute it into Eq. (3.11)

$$\begin{aligned} \rho_{COV} &= 1 - \frac{\alpha_w}{1 - (1 - \alpha_w)(1 - 0.2)} \\ &= 1 - \frac{\alpha_w}{1 - 0.8(1 - \alpha_w)} \end{aligned} \quad (3.14)$$

According to Fig. 3.13, along with the increase of absorptance of absorber, equivalent reflectance decreases rapidly. Thus it is useful to increase the thermal efficiency of the receiver by

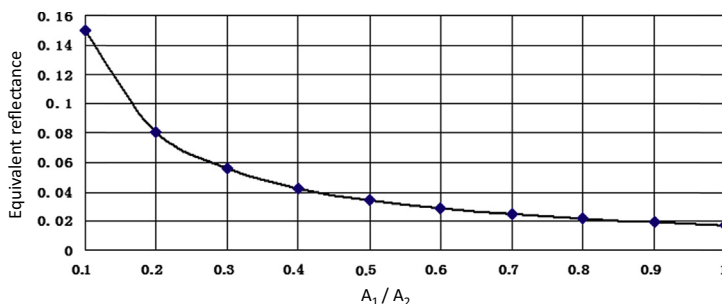


FIGURE 3.12 Equivalent reflectance of cavity receiver ( $\alpha_w = 0.85$ ).

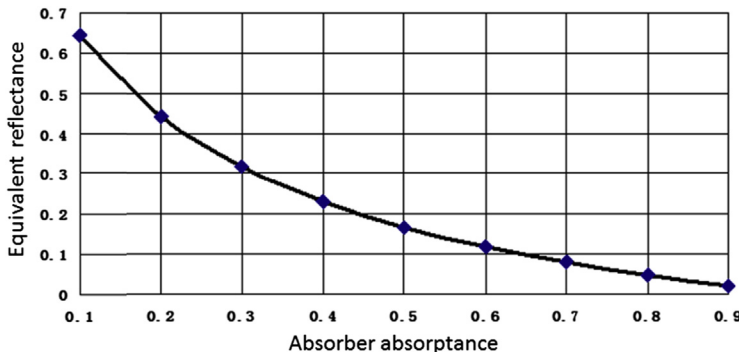


FIGURE 3.13 Equivalent reflectance of cavity receiver ( $A_1/A_2 = 0.2$ ).

selecting coatings with higher absorptance or performing surface preparation.

2. Radiation heat loss PRAD. Radiation heat loss is the thermal radiation from the receiver to the outside through the aperture of receiver.

$$P_{\text{RAD}} = \epsilon_{\text{AP}} \sigma (T_w^4 - T_g^4) A_1 \quad (3.15)$$

in which  $\epsilon_{\text{AP}}$  refers to the equivalent thermal emittance of receiver;  $\sigma$  is a Stefan-Boltzman constant;  $T_w$  refers to the mean temperature of absorber surface;  $T_g$  refers to the ground surface temperature.

In Eq. (3.15), as the aperture of cavity receiver tilts downward, it is the radiation heat exchange between the absorber surface and local ground surface that actually occurs (refer to Fig. 3.14).

$\epsilon_{\text{AP}}$  can be calculated by applying the Umarov (1983) formula

$$\epsilon_{\text{AP}} = \frac{\epsilon_w}{1 - (1 - \epsilon_w) \left( 1 - \frac{A_2}{A_1} \right)} \quad (3.16)$$

in which  $\epsilon_w$  refers to the solar emittance of absorber surface,  $\epsilon_w = 1 - a_w$ . We assume  $A_2/A_1 = 5$ , and substitute it into Eq. (3.16)

$$\epsilon_{\text{AP}} = \frac{\epsilon_w}{1 + 4(1 - \epsilon_w)} \quad (3.17)$$

Variation of equivalent emittance along with the absorptance of absorber is shown in Fig. 3.15, according to which, equivalent emittance varies greatly with the absorptance. Absorptance treatment to the absorber surface is an effective approach to reduce radiation heat loss.

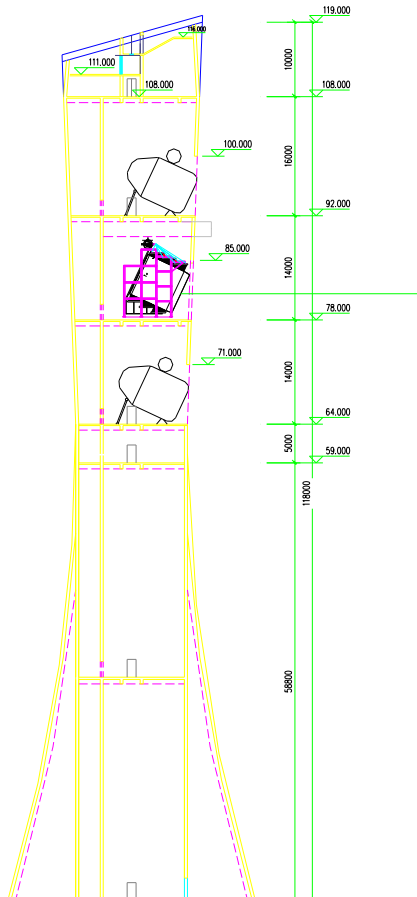


FIGURE 3.14 Radiation heat transfer between the absorber surface and local ground surface.

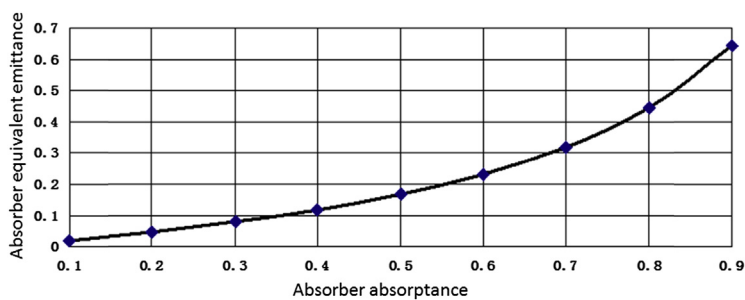


FIGURE 3.15 Equivalent emittance of cavity receiver ( $A_2/A_1 = 5$ ).

After measuring the absorber surface temperature  $T_w$  by substituting Eq. (3.16) into Eq. (3.15), formula for calculating radiation heat loss of receiver can be easily obtained.

$$P_{\text{RAD}} = \frac{\epsilon_w \sigma (T_w^4 - T_g^4) A_1}{1 - (1 - \epsilon_w) \left(1 - \frac{A_2}{A_1}\right)} \quad (3.18)$$

3. Convective heat loss  $P_{\text{conv}}$ . Convective heat losses of receiver include natural convective heat loss and forced convective heat loss. The forced convective heat loss will not be explained in this section at this moment, only the method for calculating natural convective heat loss will be discussed. Driven by buoyancy, natural convection is related to the shape of the absorber, the installation dip of receiver (Fig. 3.16), as well as the surface temperature of absorber and the respective distribution. It is extremely difficult to achieve precise conclusions only based on theoretical analysis. In this section, the experimental formula Sieber Kraabel model is applied to calculate the Nusselt number

$$Nu = 0.088 Gr^{\frac{1}{2}} \left( \frac{T_w}{T_a} \right)^{0.18} (\cos \theta)^{2.17} \left( \frac{d_{AP}}{L} \right)^8 \quad (3.19)$$

$$s = 1.12 - \frac{0.982 d_{AP}}{L} \quad (3.20)$$

in which  $\theta$  refers to the receiver dip angle (refer to Fig. 3.16);  $T_a$  refers to the ambient air temperature;  $T_w$  refers to the absorber mean temperature;  $d_{AP}$  refers to the diameter of aperture area;  $L$  is the characteristic length, which is equivalent to the depth of receiver

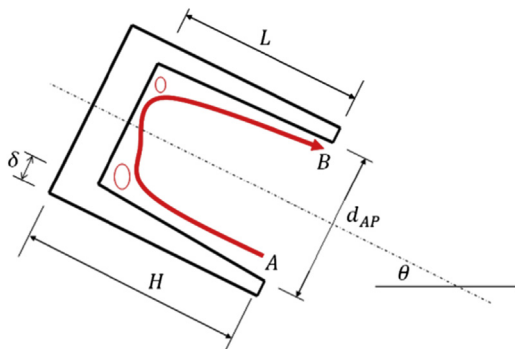


FIGURE 3.16 Cavity receiver.

aperture (refer to Fig. 3.16);  $G_r$  is the Grashof number;  $Nu$  is the Nusselt number.

In case that the receiver is placed horizontally,  $\theta = 0$ , the respective Nusselt number is  $Nu_0$ .

Nusselt numbers corresponding to other dip angles and the respective ratios are:

$$\frac{Nu}{Nu_0} = \cos^{2.47} \theta \quad (3.21)$$

Fig. 3.17 shows the variation rule of Nusselt number, according to which, the bigger of the receiver dip angle, the less of the convective heat loss. Receiver dip angle is normally determined by the concentration field arrangement, and is related to the reflection directions of heliostats. Considering solar altitudes at different time points, the calculation process is complex. This section mainly discusses the convective heat loss. This angle is assumed to be a given value that will not be explained in any detail.

According to the rules of natural convection, the approximate flow pattern inside the absorber is shown in Fig. 3.16, according to which, in case of designing blocks at corner A and B, it will effectively restrain natural convection.

$$\begin{aligned} Nu &= \frac{\alpha_{AP} L}{\lambda} \\ \alpha_{AP} &= \frac{\lambda}{L} Nu \\ &= 0.088 \frac{\lambda}{L} Gr^{\frac{1}{3}} \left( \frac{T_w}{T_a} \right)^{0.18} (\cos^{2.47} \theta) \left( \frac{d_{AP}}{L} \right)^s \end{aligned} \quad (3.22)$$

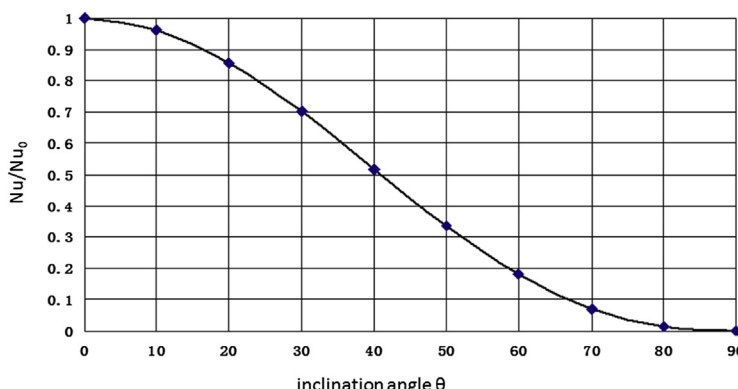


FIGURE 3.17 Variation of cavity receiver  $Nu$  over  $\theta$ .

Overflowed energy through receiver aperture due to natural convection is

$$P_{\text{CONV}} = \alpha_{\text{AP}}(T_w - T_a)A_1 \quad (3.23)$$

We substitute Eq. (3.22) into Eq. (3.23),

$$P_{\text{CONV}} = \alpha_{\text{AP}}(T_w - T_a)A_1$$

$$= 0.088Gr^{\frac{1}{3}}\left(\frac{T_w}{T_a}\right)^{0.18}(\cos^{2.47}\theta)\left(\frac{d_{\text{AP}}}{L}\right)^{\left(1.12 - 0.982\frac{\lambda_{\text{AP}}}{L}\right)}\left(\frac{\lambda}{L}\right) \quad (3.24)$$

$$(T_w - T_a)A_1$$

in which  $\lambda$  is the air thermal conductivity under ambient air temperature,  $\text{W}/(\text{m}\cdot\text{K})$ .

4. Conductive heat loss  $P_{\text{COND}}$ . Conductive heat loss of receiver depends on the thermal radiation through the receiver wall surface and thermal-insulating materials, values of which are mainly determined by its thermal-insulating performance.

$$P_{\text{COND}} = \frac{T_w - T_a}{R} \quad (3.25)$$

Provided that absorber surface temperature  $T_w$  and ambient air temperature  $T_a$  have been obtained, heat loss is transmitted through absorber to the thermal-insulating material, and further through thermal-insulating material to receiver exterior wall surface; the exterior wall surface exchanges thermal through natural convection and dissipates it into the atmosphere. Thermal resistance of this process has been calculated as follows:

$$\frac{1}{R} \approx \frac{2\pi kH}{\ln\left(\frac{r_{\text{AP}} + \delta}{r_{\text{AP}}}\right)} + h_{wb}\pi(r_{\text{AP}} + \delta)H \quad (3.26)$$

in which  $h_{wb}$  refers to the nature convective heat-transfer coefficient of receiver exterior wall surface,  $\text{W}/(\text{m}^2 \cdot ^\circ\text{C})$ ;  $\delta$  refers to the thickness of thermal insulating material,  $m$ ;  $r_{\text{AP}}$  refers to the radius of receiver aperture,  $m$ ; and  $H$  refers to the axial length of receiver,  $m$ .

Due to the nonuniform internal temperature of receiver and the installation angle of receiver, Nusselt distribution for heat exchange between receiver exterior surface and the air is also complex. Here, the horizontally placed long cylinder is used to simplify the calculation of Nusselt number through natural

convection thermal radiation. The mean Nusselt number of receiver exterior wall surface is calculated through Eq. (3.27) [52]

$$Nu_{wb} = \left\{ 0.6 + \frac{0.387 Ra_{wb}^{\frac{1}{6}}}{\left[ 1 + \left( \frac{0.559}{Pr} \right)^{\frac{9}{10}} \right]^{\frac{8}{27}}} \right\}^2, \quad 10^{-5} < Ra_{wb} < 10^{12} \quad (3.27)$$

$$\begin{aligned} Ra_{wb} &= \frac{g\beta(T_{wb} - T_a)(r_{AP} + \delta)^3}{va} \\ &= \frac{g(T_{wb} - T_a)(r_{AP} + \delta)^3}{vaT_a} \end{aligned} \quad (3.27a)$$

$$h_{wb} = \frac{\lambda Nu_{wb}}{H} = \frac{\lambda}{H} \left\{ 0.6 + \frac{0.387 Ra_{wb}^{\frac{1}{6}}}{\left[ 1 + \left( \frac{0.559}{Pr} \right)^{\frac{9}{16}} \right]^{\frac{8}{27}}} \right\}^2 \quad (3.28)$$

in which  $\beta$  is the volumetric expansion coefficient of the air,  $1/^\circ\text{C}$ , as  $\beta = 1/T_a$ ;  $v$  is the kinematic viscosity of the air,  $\text{m}^2/\text{s}$ ;  $a$  is temperature diffusion coefficient,  $\text{m}^2/\text{s}$ ;  $Pr$  is the Prandtl number of the air;  $T_{wb}$  is the mean temperature of absorber exterior wall surface,  $^\circ\text{C}$ .

We substitute Eqs. (3.26–3.28) into (3.25)

$$\begin{aligned} P_{COND} &= \left[ \frac{2\pi kH}{\ln\left(\frac{r_{AP} + \delta}{r_{AP}}\right)} + \pi(r_{AP} + \delta)Hh_{wb} \right] (T_w - T_a) \\ &= \left[ \frac{2\pi kH}{\ln\left(\frac{r_{AP} + \delta}{r_{AP}}\right)} + \delta\lambda \left\{ 0.6 + \frac{0.387 Ra_{wb}^{\frac{1}{6}}}{\left[ 1 + \left( \frac{0.559}{Pr} \right)^{\frac{9}{16}} \right]^{\frac{8}{27}}} \right\}^2 (r_{AP} + \delta) \right] (T_w - T_a) \end{aligned} \quad (3.29)$$

In the case that the reference temperature is the ambient air temperature,  $Pr = 0.71$ , we substitute it into Eq. (3.29)

$$P_{COND} = \left[ \frac{2\pi kH}{\ln\left(\frac{r_{AP} + \delta}{r_{AP}}\right)} + \pi\lambda \left( 0.6 + 0.32 Ra_{wb}^{\frac{1}{6}} \right)^2 (r_{AP} + \delta) \right] (T_w - T_a) \quad (3.30)$$

When Eq. (3.30) is applied, it is necessary to know the mean temperature  $T_{wb}$  of receiver exterior wall surface, which is calculated as follows:

$$P_{COND} = \left[ \frac{2\pi kH}{\ln\left(\frac{r_{AP} + \delta}{r_{AP}}\right)} \right] (T_w - T_{wb}) \quad (3.31)$$

Through substituting Eq. (3.27a) into (3.30), and according to Eq. (3.31) = Eq. (3.30) for energy balance, then  $T_{wb}$  can be calculated and substituted into Eq. (3.31) in order to obtain  $P_{COND}$ .

In actual projects, while considering the safety of receiver, according to the requirement of design norm, receiver surface temperature shall not exceed 80°C; otherwise, it may result in fire hazards of cables and other inflammable equipment on receiver exterior surface. When calculation is conducted through Eq. (3.31), it is also possible to substitute  $T_{wb} = 80^\circ\text{C}$  into the equation, so that

$$P_{COND} = \left[ \frac{2\pi kH}{\ln\left(\frac{r_{AP} + \delta}{r_{AP}}\right)} \right] (T_w - 80) \quad (3.31a)$$

In case of considering the influence of wind, it is also possible to directly calculate the forced convective heat-transfer coefficient of receiver exterior surface under forced convection conditions.

5. Receiver heat loss. By substituting the above into Eq. (3.9), heat loss can be calculated as follows:

$$\begin{aligned} P_{LOSS} &= P_{REFCAV} + P_{RAD} + P_{CONV} + P_{COND} \\ &= \left[ 1 - \frac{\alpha_w}{1 - (1 - \alpha_w)\left(1 - \frac{A_1}{A_2}\right)} \right] P_{AP} + \frac{\varepsilon_w \sigma (T_w^4 - T_g^4) A_1}{1 - (1 - \varepsilon_w)\left(1 - \frac{A_2}{A_1}\right)} \\ &\quad + 0.088 G r^3 \left( \frac{T_w}{T_a} \right)^{0.18} (\cos^{2.47} \theta) \left( \frac{d_{AP}}{L} \right)^{\left(1.12 - 0.982 \frac{d_{AP}}{L}\right)} \\ &\quad \left( \frac{\lambda}{L} \right) (T_w - T_a) A_1 + \left[ \frac{2\pi kH}{\ln\left(\frac{r_{AP} + \delta}{r_{AP}}\right)} \right. \\ &\quad \left. + \pi \lambda \left( 0.6 + 0.32 Ra_{wb}^{\frac{1}{5}} \right)^2 (r_{AP} + \delta) \right] (T_w - T_a) \end{aligned} \quad (3.32)$$

Or, the engineering simplified equation can be applied:

$$\begin{aligned}
 P_{\text{LOSS}} &= P_{\text{REFCAV}} + P_{\text{RAD}} + P_{\text{CONV}} + P_{\text{COND}} \\
 &= \left[ 1 - \frac{\alpha_w}{1 - (1 - \alpha_w) \left( 1 - \frac{A_1}{A_2} \right)} \right] P_{\text{AP}} + \frac{\varepsilon_w \sigma (T_w^4 - T_g^4) A_1}{1 - (1 - \varepsilon_w) \left( 1 - \frac{A_2}{A_1} \right)} \\
 &\quad + 0.088 G r^{\frac{1}{3}} \left( \frac{T_w}{T_a} \right)^{0.18} (\cos^{2.47} \theta) \left( \frac{d_{\text{AP}}}{L} \right)^{\left( 1.12 - 0.982 \frac{d_{\text{AP}}}{L} \right)} \\
 &\quad \left( \frac{\lambda}{L} \right) (T_w - T_a) A_1 + \left[ \frac{2\pi k H}{\ln \left( \frac{r_{\text{AP}} + \delta}{r_{\text{AP}}} \right)} \right] (T_w - 80) \quad (3.33)
 \end{aligned}$$

In order to facilitate the understandings of readers, a calculation example is given as follows.

Assume

$$\begin{aligned}
 T_g &= T_a = 20^\circ\text{C}, \quad T_w = 400^\circ\text{C}, \quad \alpha_w = 0.9, \quad \varepsilon_w = 0.85, \quad k = 0.048 \text{ W}/(\text{m}\cdot^\circ\text{C}), \\
 \lambda &= 0.033 \text{ W}/(\text{m}\cdot^\circ\text{C}), \quad \delta = 0.3 \text{ m}, \quad d_{\text{AP}} = 5 \text{ m}, \quad r_{\text{AP}} = 2.5 \text{ m}, \quad L = 5 \text{ m}, \\
 H &= L + \delta = 5.3 \text{ m}, \quad \theta = 20^\circ, \quad v = 22.8 \times 10^{-6} \text{ m}^2/\text{s}, \quad a = 32.8 \times 10^{-6} \text{ m}^2/\text{s}, \\
 A_1 &= 25 \text{ m}^2, \quad A_2 = 100 \text{ m}^2, \quad P_{\text{AP}} = 6500 \text{ kW}; \quad \sigma = 5.6686 \times 10^{-8} \text{ W}/(\text{m}^2 \cdot \text{K}^4)
 \end{aligned}$$

Grashof number is:

$$Gr = \frac{g \beta (T_w - T_a) L^3}{va} = \frac{9.81 \times (400 - 20) \times 5^3}{22.8 \times 10^{-6} \times 32.8 \times 10^{-6} \times 293} = 2.1 \times 10^{12}$$

When interior of the cavity is in a turbulent state, various parameters are substituted into Eq. (3.33)

$$\begin{aligned}
 P_{\text{LOSS}} &= \left[ 1 - \frac{0.9}{1 - (1 - 0.9) \left( 1 - \frac{25}{100} \right)} \right] \times 6500 \\
 &\quad + \frac{0.85 \times 5.6686 \times 10^{-8} \times (673^4 - 293^4) \times 25}{1 - (1 - 0.85) \left( 1 - \frac{100}{25} \right)} + 0.088 \\
 &\quad \times (2.1 \times 10^{12})^{\frac{1}{3}} \times \left( \frac{400}{20} \right)^{0.18} (\cos^{2.47} 20^\circ) \left( \frac{5}{5} \right)^{\left( 1.12 - 0.982 \times \frac{5}{5} \right)} \\
 &\quad \left( \frac{0.033}{5} \right) (400 - 20) \times 25 + \left[ \frac{2\pi \times 0.048 \times 5.3}{\ln \left( \frac{2.5 + 0.3}{2.5} \right)} \right] \times (400 - 80) \\
 &= 176 + 183 + 103 + 4.5 = 466.5(\text{kW})
 \end{aligned}$$

Proportions of various factors in receiver heat loss are shown in Fig. 3.18, according to which, reflection and radiation heat losses have accounted for a comparatively large proportion. Therefore, the solar selective coating on the interior surface of absorber is of great significance. Conductive heat loss is insignificant, which can be almost neglected.

Along with the increase of the dimension of aperture of receiver, intercept factor of receiver increases as well; meanwhile, the heat loss also starts to grow. Fig. 3.19 reveals the variation of cavity receiver heat loss at the design point along with the variation of the dimension of aperture of receiver. At off-design points, it is necessary to calculate the dimension of facula in the concentration field by applying the concentration field calculation software, and then calculate the intercept factor of receiver before substituting it into  $P_{AP}$  in Eq. (3.33).

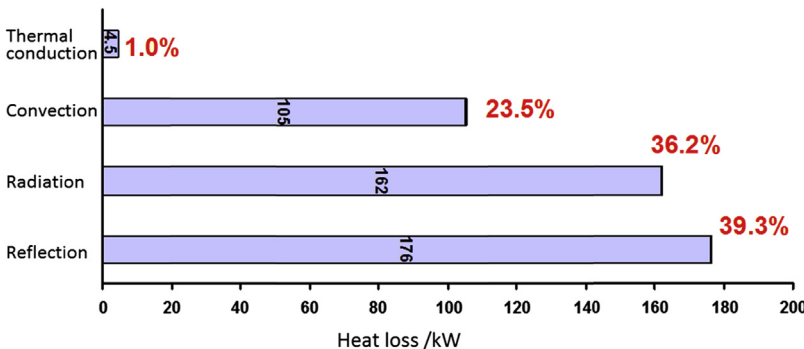


FIGURE 3.18 Heat losses in various parts of cavity receiver.

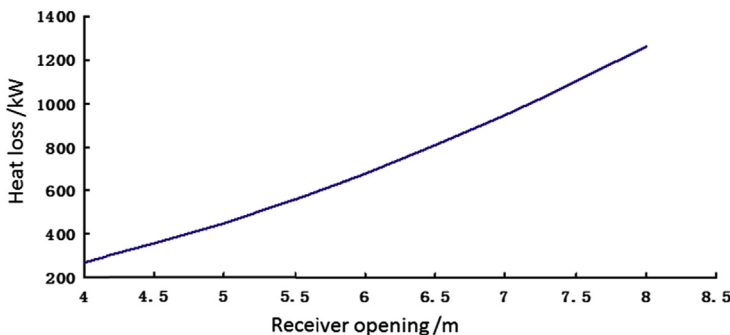


FIGURE 3.19 Variation of heat loss of cavity receiver at the design point along with the dimension variation of aperture of receiver.

The above heat loss has been calculated without considering the influences of wind speed and direction. For a commercial power plant, the receiver is normally mounted inside a sealed absorption space, in which the influence of wind on conductive heat loss can be neglected; yet its influences on convection loss shall be considered.

### **3.3 THERMAL PERFORMANCE OF PARABOLIC TROUGH COLLECTOR**

Calculation of the efficiency of parabolic trough collector is comparatively complex, which is related to the solar irradiance, axial layout of concentrator, optical performance of concentrator, working temperature of heat-transfer medium, ambient air temperature, wind speed, and concentration field features; thus it is very difficult to ensure the precision of calculation. Normally, an efficiency calculation formula shall be offered by the equipment manufacturer.

#### **3.3.1 Parabolic Trough Receiver Tube Heat Loss Parameters**

As variable properties of vacuum, transparent glass tubes and coatings against temperature variation are involved, the heat-transfer theory calculation on evacuated tube heat loss is comparatively difficult, which is normally obtained through experimental measurements. The test data of heat loss coefficient of the evacuated tube from SCHOTT of Germany is shown below, which is taken as an example to demonstrate the approximate range of heat loss coefficient of the evacuated tube.

Table 3.3 has listed data corresponding to Fig. 3.20. The unit of heat loss coefficient is the heat loss power along unit length of axial line of the evacuated tube: W/m.

In Fig. 3.20, the lateral axis is the difference of evacuated tube temperature and ambient air temperature, whereas the vertical axis is the heat loss coefficient of the evacuated tube (W/m). When the temperature difference is 293°C, the respective heat loss coefficient is about 113 W/m; when the temperature difference is 393°C, the respective heat loss coefficient is about 257 W/m. Presently, there has been no China state standard on the testing of the evacuated tube heat loss coefficient. When using various unit measured values, it is necessary to carefully check the testing approaches and conditions described in the testing report. The heat loss coefficient is related to the thermal charging mode, materials of heater, steady state conditions during temperature measurement (ambient air temperature, heater temperature), position of

TABLE 3.3 Measured Values of Heat Loss Coefficient of SCHOTT PTR70 Evacuated Tube [22]

Testing	Evacuated Tube Temperature/ °C	Mean Glass Temperature/ °C	Mean Ambient Air Temperature/ °C	Evacuated Tube and Ambient Air Temperature Difference/°C	Heat Loss Coefficient HL/(W/m)
1	100	26	23	77	15
2	153	30	23	130	23
3	213	35	23	190	43
4	246	38	24	222	59
5	317	50	24	293	113
6	346	55	23	323	141
7	390	65	24	366	204
8	418	73	25	393	257
9	453	82	23	430	333
10	458	84	24	434	348
11	506	99	24	482	495

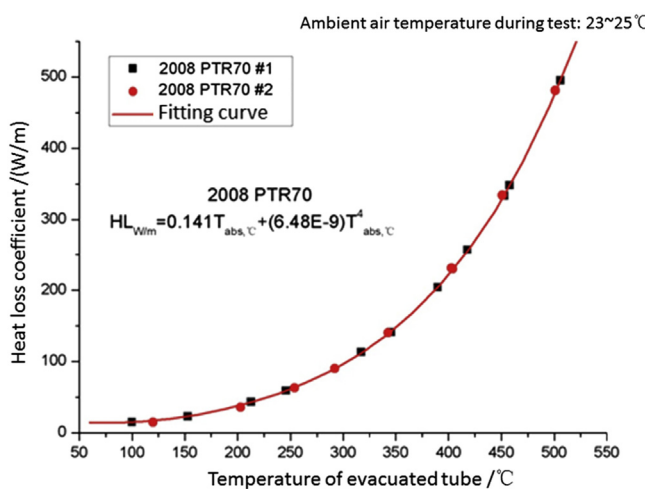
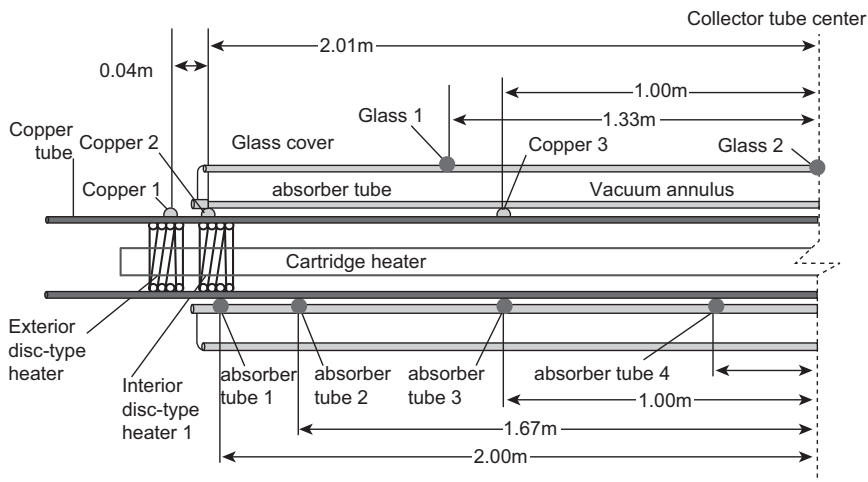


FIGURE 3.20 Heat loss coefficient of PTR70 evacuated tube from schott of germany [22]. Data Source: Technical Report NREL/TP-550-45633, May 2009.



**FIGURE 3.21** Positions of temperature measuring points on the test platform of heat loss coefficient of NREL evacuated tube [22].

temperature measuring point and sampling frequency, as well as the temperature and color of the interior wall.

Fig. 3.21 has indicated positions of temperature measuring points on the evacuated tube test platform of the National Renewable Energy Laboratory (NREL), which is part of the Department of Energy (DOE)[22]; the heater material is copper.

Standards currently suitable for testing the thermal performance of parabolic trough solar collectors include the American standard ANSI/ASHRAE 93 "Methods of Testing to Determine the Thermal Performance of Solar Collectors" [23] and European standard EN 12975-2 "Thermal Solar Systems and Components—Solar Collectors: Part 2: Test Methods" [24]. Although these two standards have already been compared by certain literature, they have focused on low-temperature thermal utilization of solar energy of flat-plate-type and vacuum-tube-type solar collectors. Working temperatures of these two types of solar collectors are normally less than 80°C; nevertheless, working temperature of the parabolic trough solar collector falls in a range of 100–400°C.

### 3.3.2 Current Status of Measurement Methods for Parabolic Trough Collector Thermal Performance

#### 3.3.2.1 Current Overseas Research Status of Thermal Performance of Parabolic Trough Collectors

Ever since 1970s, commercial products of concentrating solar collectors began to be developed, which made the DOE in the United States and

relevant industries to realize that it was highly necessary to conduct systematic and standardized testing and evaluation toward collectors; it would help to enable potential users evaluate such technology through unified tests. In 1973, with the help from the DOE, Sandia National Laboratories of America (SNLA) located in Albuquerque carried out studies on the testing of tracking parabolic trough collectors for the first time. In 1975, SNLA's mid-temperature solar system testing facility started to function, which included the parabolic trough collector module testing platform and system testing platform.

In 1977, American Society of Heating, Refrigerating and Air Conditioning Engineers (ASHRAE) published the standard test method ASHRAE 93-77, which provided guiding principles for testing non-tracking and tracking solar collectors. Henceforth, it was developed synchronously with the construction of tracking solar collector testing platform. Presided by the American Society for Testing Materials (ASTM), many investors participated in the development and evaluation of solar collectors. They applied themselves in developing the test method for tracking solar collectors, and finally published the standard test method ASTM E905 in 1983. However, as tracking solar collectors was normally used in the large-scale array, it was necessary to understand the performance of the entire system before testing a single collector module. These systems included pipelines and other system balance members, as well as unsteady state conditions. In order to acquire such data, DOE initiated a series of projects. The first project involved a large amount of field tests. These tests had focused on numerous large-scale parabolic trough thermal collecting systems on industrial sites. The second project was called the Modular Industrial Solar Retrofit project, which focused on advanced parabolic trough thermal collecting system for industrial steam and carried out development and testing works.

SNLA's parabolic trough collector module test platform includes three test stations (each test station has an independent fluid loop), a data collection system and a parabolic trough collector with an aperture area up to  $45\text{ m}^2$ . Based on the heat-transfer fluid in the loop, different testing temperatures can be defined. For example, loop 1 applies Therminol 66 synthetic oil, the maximum operating temperature of which is  $315^\circ\text{C}$ ; loop 2 applies Syltherm 800 synthetic oil, the maximum operating temperature of which is  $425^\circ\text{C}$  (refer to Fig. 3.22). Biaxial rotation test platform is able to make the aperture of receiver of parabolic trough collector face a random direction within a specific test period. In addition, the meteorological station collects all necessary data about natural conditions. The laboratory also published some important testing research reports related to the performance of parabolic trough collectors, such as the 30 MWe SEGS Power Plant Simulation Report [25], Test Report for LS-2 Parabolic

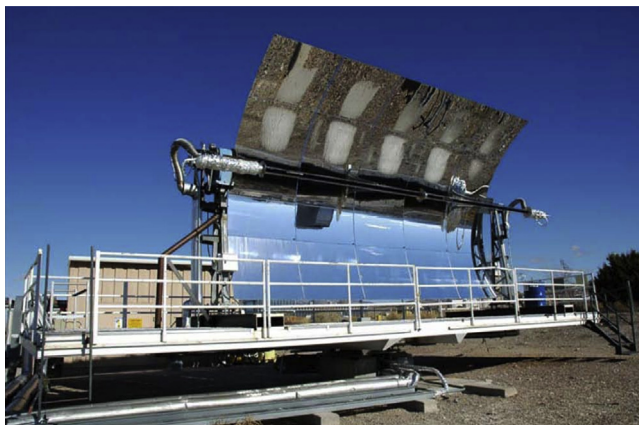


FIGURE 3.22 Parabolic trough collector module test platform of Aandia National Laboratories of America.

Trough Collector Applied in SEGS Power Plant, Test Report for Parabolic Trough Collector Mounted with Schott Vacuum Receiver, and Parabolic Trough Collector Steady State Test Report for Industrial Applications [26].

Early tracking solar collector tests carried out by SNLA and the subsequent Solar Energy Research Institute of America were based on the general technologies in ASHRAE 93-77. However, this method was not completely applicable for the tracking solar collector, because there were no massive explanations, analysis and precise testing technologies specifically described in this standard to be related to the tracking solar collector testing. Being aware of the incompleteness of this method, the solar energy commission of ASTM established a subordinate professional commission, which carried out a series of studies on standards from the aspect of economic test methods. The target of this standard was to define the annual energy output of the appointed tracking solar collector at a specific location. This professional commission operated by following the principle of voluntariness and unanimity through consultation, members of which included manufacturers, users and other representatives from industries, governments, colleges, and universities as well as testing laboratories. Solar Energy Research Institute of America drafted the original standards for this professional commission; the ultimate achievement was the ASTM standard test method E905-87: "Standard Test Method for Determining Thermal Performance of Tracking Concentrating Solar Collectors," the newest version of which was the updated version in 2007.

According to the testing requirements of concentrating solar collectors, this standard has mainly considered the respective massive technical problems, which include:

Influences of tracking/driving system and surface precision of reflector on thermal performance of collectors; Appropriate selection of standardized factors for incident solar radiation; Research on quasi steady state test conditions for solar collectors with high concentration ratios; As the high temperature synthetic oil applied in testing is lack of sufficiently precise specific thermal power parameters, the specific thermal power of synthetic oil shall be determined through calorimetry; Testing and analysis on vertical incidence and angular incidence on aperture of receiver of collector; In the case that heat-transfer fluid within the collector does not flow, sunshine may cause damage to the collector; therefore, requirements on pretreatment of solar collector shall be cancelled; For large-scale solar collectors, most of the solar simulators may introduce interferences and uncertainty; therefore, it is specified to perform the test outdoors under the clear weather.

This published standard shall be applied in axial or biaxial concentrating solar collectors; influences of solar scattering radiation are negligible, only influences of direct radiation, as well as determination of optical responses of collectors toward different solar incidence angles and thermal performance of vertically incident solar radiation under different operating temperatures shall be considered. Methods in this standard are requested to achieve quasi steady state conditions, measure certain environmental parameters, and determine the product of inlet and outlet temperature difference of heat-transfer fluid within the collector and thermal capacity of heat-transfer fluid. The test method has provided experiment and calculation procedures in order to determine such parameters as response time, incidence angle correction factor, range of near-vertical incidence angle, and the thermal gain rate corresponding to the near-vertical incidence angle.

According to the definition, response time refers to the time required for the temperature increase of heat-transfer fluid within a specified collector after the step change of solar radiation, which has determined the time necessary for achieving quasi steady state conditions. Thermal performance of a collector corresponding to a random incidence angle is obtained through the calculation of the incident angular modifier (IAM) and thermal performance of collector under near-vertical incidence. Measurement of IAM is carried out when the collector heat loss is at the minimum level; therefore, inlet temperature of heat-transfer fluid during the measurement is equivalent to or close to the ambient air temperature. In case that the tested collector is mounted on a biaxial tracking test platform, the thermal performance test is able to achieve the condition of vertical incidence of solar radiation through the aperture of receiver of

collector all day long. In case that the single axis platform is used for testing, or a linear concentrating collector uses its original tracking/driving device, the range of near-vertical incidence must be determined. The testing standard has also provided the method to obtain this angular range, within which the decrease of thermal performance does not exceed 2%. The testing standard has strict requirements on the variation of measurement parameters. These parameters include heat-transfer fluid inlet temperature of collector, temperature increase of heat-transfer fluid after passing through the collector, product of heat-transfer fluid flow rate and specific heat capacity, ambient air temperature and solar DNI.

During the period from 1974 to 1980, a few of tracking solar collector testing research institutions were established in America. Although they were designed and completed before ASTM testing standard being published, basic principle of ASHRAE 93-77 reserved in ASTM standards served as the design foundation for these test platforms; in addition, many test platform designers also participated in the solar energy sub-committee of ASTM. It was important these research institutions focused on the design of linear concentrating tracking parabolic trough collectors. It had reflected that when these works were performed, linear concentrating parabolic trough solar collectors had already been close to commercialization and manufactured by some American companies. It was also noticeable that each of these research institutions had biaxial rotation test platforms; by controlling the tracking direction, they could achieve the vertical incidence of solar radiation on aperture of receiver of collector. Thus thermal performance testing for collectors could be performed in most times of the day.

In 2010, with the support from the NREL published the performance testing instruction for large-scale parabolic trough solar systems, and offered basic principles of two test methods, namely short-term steady state test and multiday continuous test method. The instruction aimed at creating the official PTC52 concentrating solar power generation performance testing standard of the American Society of Mechanical Engineers; according to the plan, the standard included other parabolic trough concentrating solar power generation technologies. However, it normally costs years of time to complete the preparation and approval works related to an official performance testing standard.

As a matter of fact, before carrying out this research, the laboratory had already carried out loop test on SEGS parabolic trough collectors (refer to Fig. 3.23). Furthermore, for technologies related to the performance of parabolic trough collectors, the laboratory had carried out a series of research works, and published the respective research reports (e.g., outdoor measurement of optical performance of the vacuum-tube-type parabolic trough evacuated tube, pipeline modeling of parabolic trough thermal collection system, rapid analysis on parabolic trough collector



FIGURE 3.23 Testing loop of SEGS parabolic trough collector.

field, heat-transfer analysis and modeling of parabolic trough evacuated tube, heat loss analysis on evacuated tube type parabolic trough evacuated tube and indoor heat loss test method, research on parabolic trough evacuated tube based on site conditions, performance model of parabolic trough solar power plant, simulation model of parabolic trough solar power plant, testing of parabolic trough collector reflective surface, solar advisory model established for parabolic trough solar power plant, technology and performance evaluation of parabolic trough solar power plant, and wind tunnel test method of parabolic trough collector [27].

Deutsches Zentrum für Luft-und Raumfahrt (DLR) has also carried out field testing research on parabolic trough collectors or the collector field. In order to satisfy field installation requirements, testing based on field conditions requires a set of movable equipment and instruments, which mainly include the clamp-on sensor that is able to measure temperature, flow rate and inclination angle, mobile meteorological station, and data collection system. Such testing is able to accomplish the following tasks: Collector field performance evaluation (depending on field and power plant running conditions), efficiency of collector/array/loop, incidence angle influencing factor, heat loss, annual performance prediction, etc.

Besides, in 2009, by referring to the biaxial test platform of SNLA, DLR started to design the Kontas parabolic trough collector rotation test platform (refer to Fig. 3.24A). This research center also carried out studies on technologies related to parabolic trough collectors, which mainly included influences of measuring equipment on the uncertainty of parabolic trough collector performance testing, parabolic trough collector testing in the REACT project, solar flux density testing in parabolic trough

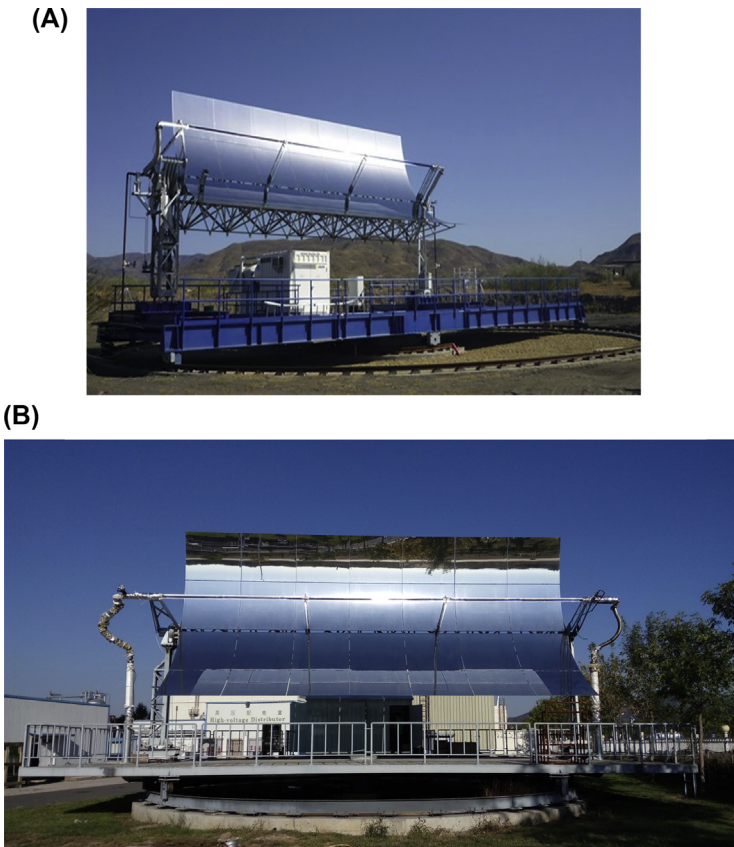


FIGURE 3.24 (A) Kontas test platform in Spain. (B) Institute of Electrical Engineering, Chinese Academy of Sciences test platform in Beijing, China.

collector concentration field, optical efficiency test platform of indoor and outdoor parabolic trough vacuum evacuated tube, transient simulation model for parabolic trough solar power plant and influences of transient variation on energy output, as well as transient thermography method for heat loss testing of parabolic trough evacuated tube.

Fig. 3.24B shows the test platform at IEE-CAS.

Except for the above-mentioned four prominent international research institutions, many scholars in the world have also carried out in-depth studies on parabolic trough collectors. For example, parabolic trough collector efficiency testing by applying the quasi steady state test method in the European standard EN 12975-2; application of American standard ASHRAE 93-2003 and European standard EN 12975-2 in parabolic trough collector performance testing and the respective

comparisons; experimental model established on the basis of parabolic trough collector performance analysis; research on performance values of parabolic trough evacuated tube by comparing configurations of nonvacuum and vacuum parabolic trough evacuated tube; prediction on the truncation factor of parabolic trough collector. Furthermore, simulation and control models of parabolic trough power plant have also been established by fully considering the thermal performance of parabolic trough collectors (e.g., a linear prediction control model developed for 30 MW parabolic trough solar power plant; the dynamic simulation model for a parabolic trough solar power plant with thermal storage facilities; a concentration field analytic model that considers heat loss of nonlinear parabolic trough collectors; a PATTO model that is capable of predicting the overall performance of parabolic trough power plant under abnormal working conditions; model computer program SimulCET for parabolic trough power plant based on experiences and physical derivation).

It is a remarkable fact that technical standards of CSP generation are of great significance for the accelerated reduction of costs. Therefore, CSP generation and thermochemistry organization (SolarPACES) subordinate to International Energy Agency (IEA) is now carrying out the international project TASK I CSP generation system, which includes the development of testing procedures and standards for the parabolic trough collector field. Although many works have been conducted in order to realize standardization, thermal performance test method of parabolic trough collector still needs to be improved. EN 12975-2 standard that is applicable for concentrating solar collectors has already been an integral part of ISO 9806, which is now being revised. Under the framework of SolarPACES, a work-group for CSP generation standards was founded in 2011. A standard must be improved while orienting toward a common framework, which shall also be intensified in terms of the following aspects, namely qualification, certification, testing procedures, components and system endurance test, entrusting procedures, model-based results, concentration field modeling, etc.

### **3.3.2.2 Brief Introduction to the ASHRAE 93 Steady State Test Method**

The newest version of ASHRAE 93 was published in 2010 [23], which specifies that in order to be consistent with the international state standard ISO 9806-1 “Test Methods for Solar Collectors—Part 1: Thermal Performance of Glazed Liquid Working Medium Heating Collectors Including Pressure Drop” [28], partial testing process and certain requirements on measurement parameters in the previous version have been adjusted in this revised standard.

This testing standard offers the specific measurement operation process and calculation procedures, and separately determines thermal efficiencies at the aperture of receiver of parabolic trough collector under near-vertical incidence of solar radiation corresponding to different inlet temperatures of heat-transfer fluid within the collector, and optical responses of parabolic trough collector corresponding to different solar incidence angles. In order to make sure that calculation results are compared in accordance with the unified standard, thermal efficiency on the basis of the aperture area of parabolic trough collectors in ASHRAE 93 has been applied in this section for the regression of steady state test model as well as the respective prediction and calculation, refer to Eq. (3.34).

$$\eta_a = F_R \left[ (\tau\alpha)_e \rho \gamma - \frac{A_r}{A_a} U_L \frac{(T_{fi} - T_a)}{G_{bp}} \right] = \frac{\dot{m} c_f (T_{fo} - T_{fi})}{A_a G_{bp}} \quad (3.34)$$

in which  $F_R$  refers to the heat remove factor of collector;  $(\tau\alpha)_e$  refers to the normal absorption and transmission factor of collector;  $A_a$  refers to the area of aperture of receiver of collector;  $A_r$  refers to the area of absorber of collector;  $\gamma$  refers to azimuth angle coefficient correction factor;  $\rho$  refers to the altitude angle coefficient correction factor;  $U_L$  refers to the heat loss coefficient;  $T_{fi}$  refers to the inlet temperature of heat-transfer fluid of the collector;  $T_a$  refers to the ambient air temperature;  $G_{bp}$  refers to the solar DNI;  $\dot{m}$  refers to the mass flow of heat-transfer fluid;  $c_f$  refers to the specific thermal capacity of heat-transfer fluid; and  $T_{fo}$  refers to the outlet temperature of collector.

For thermal efficiency testing at the aperture of receiver of parabolic trough collector under solar near-vertical incidence, within the working temperature range of parabolic trough collector, inlet temperatures of heat-transfer fluid from at least four evenly separated collectors shall be determined, and inlet temperature of heat-transfer fluid from one collector shall approach the ambient air temperature; under the maximum thermal collection, inlet temperature of heat-transfer fluid is the maximum working temperature of parabolic trough collector. For inlet temperature of heat-transfer fluid of each collector, the steady state test model needs to acquire at least four independent data points. Therefore, the total data points shall be not less than 16 points. Only in this case, can regression for steady state test model parameters be conducted.

It is necessary to achieve the strict steady state condition when conducting the collector performance testing in order to ensure the effectiveness of test data, which requires to conduct the test under a clear weather, requires solar DNI to be larger than  $800 \text{ W/m}^2$  within the entire test period, and requires the volume flow of heat-transfer fluid passing through the parabolic trough collector to be set to the same value, etc.;

**TABLE 3.4** Requirements on Measurement Parameters Within the Steady State Test Period

Parameter	Value	Parameter	Value
$G_{bp}$	$\pm 32 \text{ W/m}^2$	Inlet temperature of heat-transfer fluid within the collector	$\pm 2\%$ of set value
Ambient air temperature	$\pm 1.5^\circ\text{C}$	Outlet temperature of heat-transfer fluid within the collector	$\pm 0.05^\circ\text{C}$ per minute
Volume flow of heat-transfer fluid	$\pm 2\%$ of set value	Mean ambient wind speed	$2 \sim 4 \text{ m/s}$

and these measurement parameters shall also satisfy the allowable deviation specified in Table 3.4.

Parabolic trough solar collectors operate while tracking the movement of the Sun in the axial direction. However, the rotation test platform is capable of enabling the near-vertical incidence of solar radiation at the aperture of receiver of parabolic trough collector within the test period, which means, in order to make sure that the steady state test model is able to conduct the long-term prediction on the thermal performance of parabolic trough collectors, IAM shall be completed in another independent testing process in order to determine the variation of thermal efficiencies of parabolic trough collectors under different incidence angles. For testing the incidence angle correction factor, the inlet temperature of heat-transfer fluid within the parabolic trough collector shall be within  $\pm 1^\circ\text{C}$  of the ambient air temperature. In case of not being able to satisfy such requirement, IAM  $K_{\tau\alpha}$  shall be calculated in accordance with Eq. (3.35).

$$K_{\tau\alpha} = \frac{\eta_a + F_R U_L (T_{fi} - T_a) / G_{bp}}{F_R [(\tau\alpha)_e \rho \gamma]_n} \quad (3.35)$$

in which  $\eta_a$  refers to the intercept efficiency of collector.

The steady state test method has been the most widely recognized performance test method all over the world for parabolic trough solar collectors. Many tests have been completed in accordance with this method (e.g., the test for LS-2 parabolic trough collectors of the first commercial CSP plant (SEGS) in the world, and the test for LS-2 parabolic trough collectors mounted with PTR70 vacuum evacuated tubes, the test for parabolic trough collectors applied in the industrial field and the test for a type of fiberglass-reinforced parabolic trough collectors).

Nevertheless, for a large-scale parabolic trough solar collector in actual operation, the respective length has determined that it cannot be placed on a biaxial rotation tracking test platform, which means, the condition of near-vertical incident of solar radiation on the daylight surface of parabolic trough collector is basically unfulfillable; in addition, testing for the IAM also cannot be conducted. In the case that the parabolic trough collector is arranged horizontally along the north-south axis, condition of near-vertical incident of solar radiation on the daylight surface of parabolic trough collector only occurs once in the morning and once at night every day; yet at this moment, it happens to depend on fluctuation of increase or decrease of solar DNI, even under such circumstances, it cannot be ensured that it may occur at any given time throughout the year; instead, it depends on the latitude of the test site. In the case that the parabolic trough collector is arranged horizontally along the west-east axis, only around midday can incidence of solar radiation along the normal direction near the daylight surface of a parabolic trough collector occur.

Besides, analytic results have indicated that when parabolic trough collectors are subject to the typical intermittent heat-transfer fluid temperature variation in the heating process under cloudy conditions, the steady state test model is ineffective. Therefore, the steady state test duration may be extended by these adverse natural environment and operating conditions, especially for test sites with less favorable natural environmental conditions.

### **3.3.2.3 Brief Introduction to the EN 12975-2 Quasi-Dynamic Test Method**

In order to adapt to more extensive natural environmental conditions, except for the steady test method, the European standard EN 12975-2 also provided a quasi-dynamic test method for solar collector thermal performance [29]. The respective quasi dynamic test model is established on the basis of minimum error analysis of solar collector output power. Furthermore, it has also been integrated with the ambient wind speed, sky temperature, the IAM for scattering irradiance, etc., which are shown in Eq. (3.36).

$$\frac{\dot{Q}}{A} = F'(\tau\alpha)_{en} K_{\theta b}(\theta) G_{bp} + F'(\tau\alpha)_{en} K_{\theta d} G_d - c_6 u G^* - c_1(T_m - T_a) - c_2(T_m - T_a)^2 - c_3 u(T_m - T_a) + c_4 \left[ E_L - \sigma(T_a + 273.15)^4 \right] - c_5 dT_m/d\tau \quad (3.36)$$

in which  $\dot{Q}$  refers to the output power of solar collector;  $F'(\tau\alpha)_{en}$  refers to the efficiency factor of collector;  $k_{\theta b}(\theta)$  serves as the IAM for DNI, yet the specific function expression of the IAM provided by this standard is only

applicable for flat-type solar collectors instead of parabolic trough solar collectors.  $k_{\theta d}(\theta)$  refers to the collector's IAM;  $G^*$  refers to the hemispherical irradiance of aperture of receiver surface of collector;  $c_1, c_2, c_3, c_4, c_5$  are regression coefficients;  $T_m$  refers to the mean temperature of fluid within the collector;  $E_L$  refers to the heat loss;  $\sigma$  is the Stefan–Boltzmann constant,  $\sigma = 5.67 \times 10^{-8} \text{ W}/(\text{m}^2 \text{ K}^4)$ ;  $\tau$  refers to time;  $u$  refers to ambient wind speed. Therefore, for parabolic trough solar collector under higher working temperatures and more complex optical effects, there has been no literature to demonstrate that this function expression remains to be fully convenient and effective.

By using the mathematical tool of multiple linear regression (MLR), the two IAMs,  $k_{\theta b}(\theta)$  and  $k_{\theta d}(\theta)$  in the quasi dynamic test model are able to be obtained together with other parameters of the model on a simultaneous basis, instead of requiring an independent IAM testing process like the steady state test method mentioned above.

Heat loss in the quasi dynamic test model is expressed by a function that contains a quadratic polynomial, and it depends on the difference between the inlet and outlet mean temperature  $T_m$  parabolic trough collector heat-transfer fluid and the ambient air temperature  $T_a$ . Furthermore, derivatives containing inlet and outlet mean temperature of heat-transfer fluid of parabolic trough collectors serve as the effective thermal capacities of collectors, in which  $dT_m/d\tau$  can be obtained by calculating the difference between the current moment  $T_m$  and previous moment  $T_{m-1}$  and dividing it by the sampling interval of  $T_{f0}$  and  $T_{fi}$ .

Although the quasi dynamic test method allows the collector thermal performance test to last continuously for several hours together with solar irradiance fluctuation and solar position variation, it still needs to satisfy certain specified allowable deviation of measurement parameters, which are shown in [Table 3.5](#). It is a remarkable fact that the testing system requires to strictly control the inlet and outlet temperature of heat-transfer fluid of parabolic trough collectors and the mass flow of heat-transfer fluid passing through parabolic trough collectors. However, for a large-scale parabolic trough solar thermal collection system, it is difficult to satisfy these test conditions based on its own control equipment.

Based on the inlet temperature of collector and the combination of natural environmental conditions that contain cloudy and clear days, testing sequences recommended by the quasi dynamic test method can be summarized into four types of testing days, and one of them is subject to the condition of partial cloud. The quasi dynamic test method still requires testing inlet temperatures of heat-transfer fluid of at least four evenly separated collectors within the working temperature range of parabolic trough collectors. Furthermore, collector thermal performance quasi dynamic test method requires each testing sequence to last for at least 3 h with an overall testing time of about five testing days.

**TABLE 3.5** Requirements for Measurement Parameters Within the Quasi-Dynamic Test Period

Parameter	Value	Parameter	Value
Global solar irradiance	300–1,100 W/m <sup>2</sup>	Inlet temperature of heat-transfer fluid within the collector	±1°C
Ambient air temperature	±1.5°C	Outlet temperature of heat-transfer fluid within the collector	1°C more than the inlet temperature of heat-transfer fluid within the collector
Mass flow of heat-transfer fluid	±1% of the set value when being within the testing sequence, ±10% of the set value when being between testing sequences	Mean ambient wind speed	1~4 m/s

However, actual quasi dynamic test time depends on natural environmental conditions of the test site.

Task 4 of the SolarPACES and task 33 of solar heating and refrigeration organization of the IEA jointly constitute the research program of Solar Thermal for Industrial Processes. In this program, according to the quasi dynamic test method, thermal performance test for the parabolic trough solar collector is conducted [28]. However, outlet temperatures of heat-transfer fluid of parabolic trough collectors applied in this program have not exceeded 250°C. Furthermore, there has been no literature to demonstrate that the quasi dynamic test method in European standard EN 12975-2 is completely applicable for the parabolic trough solar collector with an outlet temperature of heat-transfer fluid exceeding 300°C.

### 3.3.3 Test Methods to Determine the Thermal Performance of the Parabolic Trough Collector

#### 3.3.3.1 Current Status of Thermal Performance Test Method

In 1977, America published the ASHRAE 93-2003 standard “Test Methods to Determine Thermal Performance of Solar Collectors,” the newest version of which is ASHRAE 93-2010. As indicated in Section Two of the standard method, this standard is applicable for nonconcentrating and concentrating solar collectors; heat-transfer fluid flows into the

collector through a single inlet and flows out through a single outlet. Apparently, the parabolic trough solar collector is influenced by the scope of the definition. It defines the thermal efficiency of solar collector as the ratio of collected useful energy and solar energy intercepted by the total area of the collector, and offers the efficiency of concentrating solar collector.

$$\begin{aligned}\eta_g &= (A_a/A_g)F_R[(\tau\alpha)_e\rho\gamma - (A_r/A_g)U_L(t_{f,i} - t_a)/G_{bp}] \\ &= \dot{m}c_p(t_{f,o} - t_{f,i})/A_gG_{bp}\end{aligned}\quad (3.37)$$

in which for the concentrating collector,  $A_a$  refers to the aperture area of collector;  $A_g$  refers to the gross area of the collector;  $A_r$  refers to the aperture area of receiver of the collector.

For the concentrating collector, Eq. (3.37) generates a linear relationship between the thermal efficiency  $\eta_g$  and parameter  $(T_{f_i} - T_a)/G_{bp}$ . The intercept of this linear equation on y axis is  $(A_a/A_g)F_R(\tau\alpha)_e\rho\gamma$ , the respective slope is  $(A_r/A_g)F_RU_L$ . Furthermore, the product  $(\tau\alpha)_e\rho\gamma$  varies along with the incidence angle. For many collectors, a linear efficiency curve is sufficient, but for some collectors, it may need a high-order fitting curve.

In order to determine the thermal characteristics of solar collectors, the test shall be conducted under clear weather conditions, while maintaining the incidence of solar radiation near the normal of collector aperture of receiver, namely ensuring the influences of incidence angle on collector thermal efficiency not exceed 2% of the efficiency of collector at aperture of receiver under vertical incidence of solar radiation.

In order to determine the thermal efficiency curve of the collector by applying the two-parameter [ $F_R(\tau\alpha)_e\rho\gamma$  and  $F_RU_L$ ] solar collector thermal performance test model in Eq. (3.37), at least 16 data points shall be measured. These two parameters can be determined on the basis of the regression by applying the least-square method, which is shown in Fig. 3.25. Intercept of the line through regression on the vertical axis and the respective slope of the line are the values of these two parameters. After determining these two parameters, the test model can be used to predict the whole-day solar collector output energy according to different operating temperatures, natural environment data and the IAM by using "hour" as the time calculation unit through accumulation of hourly output energy of the collector, which is of great significance for the solar thermal collection system designer.

As a matter of fact, the comprehensive heat loss coefficient ( $U_L$ ) that represents the thermal conduction, convection, radiation, and heat exchange losses of receiver of the collector is not a constant, but a function of absorber temperature, ambient air temperature and wind speed. Although  $U_L$  obtained through statistical regression analysis is a fixed

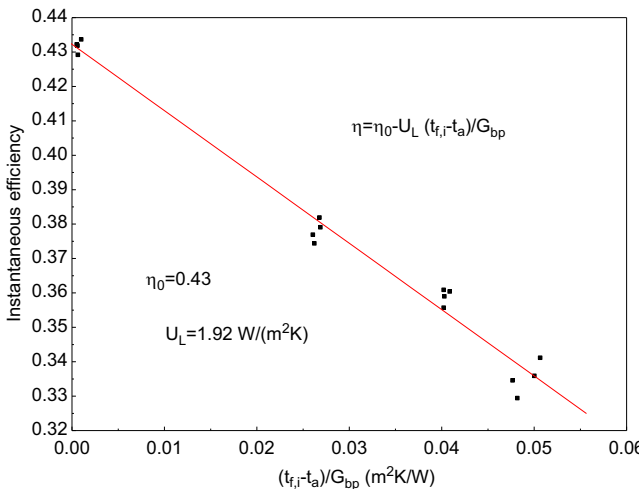


FIGURE 3.25 Collector transient efficiency curve.

value, which is not completely consistent with its strict physical meaning, this method does not have any influence on the prediction of long-term thermal performance of collectors. It is because influences of various factors in the actual process on  $U_L$  are insignificant, which have been widely verified. In the ASHRAE 93 standard, a calculation example has offered the testing model based on parameters determined through regression to calculate the hourly output energy of collector and the whole-day output energy of collector after accumulation, the calculation conditions and results of which are shown in Table 3.6 [23].

As described in the section of "significance and application," this test method is intended to provide test data essential to the prediction of the thermal performance of a collector in a specific system application in a specific location. In addition, to the collector test data, such prediction requires validated collector and system performance simulation models that are not provided by this test method. The results of this test method therefore do not by themselves constitute a rating of the collector under test. Furthermore, it is not the intent of this test method to determine collector efficiency for comparison purposes since efficiency should be determined for particular applications." Therefore, such solar collector test method is not offered to conduct quality rating or search for certain quality parameters or indices of a particular component of a collector under specific conditions; the fundamental target is to design a collector application system. As thermal performance of collector is changeable, when comparing two solar collectors, daily output energy and annual cumulative output energy of collector must be considered, instead of

TABLE 3.6 Calculation of Hourly Useful Thermal Collection of Solar Collector [23]

Time/ h	$T_a/^\circ\text{C}$	$G/(\text{W}/\text{m}^2)$	$G_{bp}/(\text{W}/\text{m}^2)$	$\Delta t/G/(\text{m}^2 \text{K}/\text{W})$	$\theta/^\circ$	$K_{\tau\alpha}$	$(q_u/A_s)/(\text{W}/\text{m}^2)$
6	25.56	41	0	0.5141	93.4	0	0
7	26.11	189.24	116.7	0.1086	79.6	0.58	0
8	26.67	394.24	305.93	0.0507	66.2	0.84	78.85
9	29.44	583.48	488.86	0.0296	53.5	0.93	252.31
10	31.11	731.71	633.94	0.0211	42.5	0.96	381.63
11	32.78	826.33	728.56	0.0167	33.4	0.98	469.94
12	33.33	861.02	763.25	0.0155	30	0.98	498.32
13	34.44	826.33	728.56	0.0148	33.4	0.98	476.24
14	35.56	731.71	633.94	0.0187	42.1	0.96	400.55
15	36.11	583.48	488.86	0.0181	53.5	0.93	280.7
16	36.11	394.24	305.93	0.0264	66.2	0.84	119.85
17	35.56	189.24	116.7	0.0593	79.6	0.58	0
18	35	41	0	0.2851	93.4	0	0

$q_u$ , useful energy.

comparing parameters themselves that have been obtained through regression.

Thermal performance test method of solar collector follows a basic idea. Thermal performance test of solar collector aims at designing a collector application system. Therefore, it is necessary to take into consideration main thermal performance characteristics related to the operation of collectors; by measuring various parameters related to thermal performance of collector, according to the respective thermal performance mathematical model, mathematical methods of statistical regression can be used to identify the undetermined coefficient in the model; based on the thermal performance model, other physical conditions can be calculated and predicted, such as the whole-day and annual cumulative useful output energy of collector under solar irradiance, ambient air temperature and system operating temperature of a specific day. It is a remarkable fact that along with the increase of influencing factors for operating conditions of solar collector, it is necessary to use a more complex mathematical model to describe the respective thermal performance on a reasonable basis, and further offer the precise whole-day and annual cumulative output energy of collector under changing input conditions.

There are two basic methods to establish the mathematical model. One is the mechanism analysis method, which is to establish a model by utilizing modeling information or prerequisite provided by modeling assumptions on the basis of the analysis on the internal mechanism of matters; it is normally referred to as the white box, such as the energy balance equation and thermal and mass transfer theory. The other one is the system identification method, which is to establish a model by utilizing modeling assumptions or actual input and output information of matter system offered to system test data while being absolutely ignorant of the internal mechanism of system; it is normally referred to as the black box. According to different principles, model identification methods can be summarized into four categories: (1) the least-square method, including the least-square method, the extended least-square method, auxiliary variable method and the generalized least-square method; (2) gradient correction parameter identification method, such as stochastic approximation method; (3) probability density approximation parameter identification method, such as the maximum likelihood method; (4) new methods that have been recently developed, such as the blur identification method, neural network identification method, wavelet identification method and inheritance identification method.

To sum up, thermal performance test model of solar collector is to establish the mechanism model according to the energy balance theory and heat-transfer principle, and identify the undetermined parameters of the model by applying the least-square method; it belongs to a grey box model. Such test model based on empirical methods is deemed to be able to generate highly precise results with the respective range of applied parameters.

### **3.3.3.2 Assumed Conditions of Dynamic Test Model**

Dynamic test model of parabolic trough solar collector shall satisfy the following assumptions.

1. Based on the requirement of ASHRAE 93 standard on volume flow of heat-transfer fluid being within  $\pm 2\%$  of the set value during the test, according to the dynamic test model assumption, volume flow variation of synthetic oil passing through the parabolic trough collector within the test period does not exceed  $\pm 2\%$  of the mean value of the period. However, considering that density variation of synthetic oil within the application temperature normally exceeds 10%, such as the density variation of synthetic oil applied under Experimental Conditions of this research, which is shown in Fig. 3.26. Therefore, mass flow of synthetic oil passing through the parabolic trough collector within the test period is assumed to be within  $\pm 20\%$  of the mean value without any intensive fluctuation of

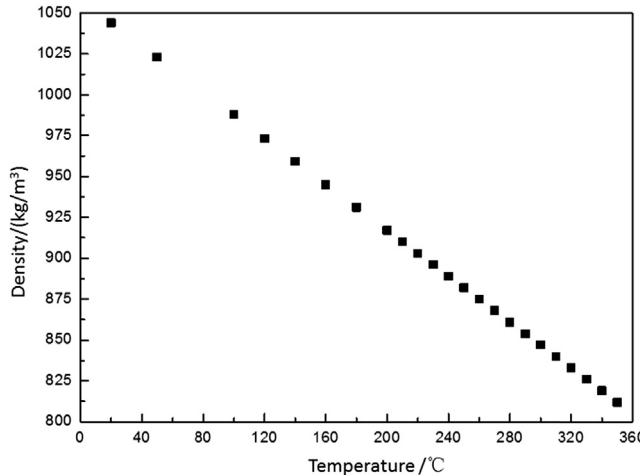


FIGURE 3.26 Density variation of synthetic oil.

abrupt change, such as the stoppage of circulating pump or instantaneous change of valve opening control during normal operation.

2. Based on all experimental data obtained through the test, cleanliness of mirror surface of parabolic trough concentrator and exterior wall surface of glazed shield tube of parabolic trough evacuated tube are consistent with each other, such as cleaning these two surfaces before the test.
3. For the connecting and supporting components at the glass-metal sealing point, thermal stress buffer segment and between two pieces of evacuated tubes, etc., due to the extremely small proportions of their scales against the total length, their influences on the heat-transfer process are not individually considered.
4. Profile defect and installation error of parabolic trough concentrator, and positioning error of parabolic trough evacuated tube, are constants.

### 3.3.3.3 Model Establishment for Heat-Transfer Process

Based on the Lumped Capacitance Method, energy balance equation for the metal evacuated tube of parabolic trough collector is listed and expressed as follows

$$C_b = \frac{dT_b}{dt} = SA_a - A_f U_{bf}(T_b - T_f) - A_{am} U_{ba}(T_b - T_a) \quad (3.38)$$

in which  $C_b$  refers to the thermal power of metal evacuated tube;  $T_b$  refers to the temperature of metal evacuated tube;  $T_f$  refers to the temperature of

heat-transfer fluid;  $T_a$  refers to the ambient air temperature;  $A_a$  refers to the aperture area of parabolic trough collector;  $A_f$  refers to the heat exchange area between metal evacuated tube and heat-transfer fluid;  $A_{am}$  refers to the heat exchange area between metal evacuated tube and the environment;  $U_{bf}$  refers to the heat-transfer coefficient between metal tube and heat-transfer fluid;  $U_{ba}$  refers to the comprehensive heat-transfer coefficient between metal evacuated tube and the environment;  $\tau$  refers to time;  $S$  refers to the part absorbed by the exterior wall surface of metal evacuated tube when solar DNI is perpendicular to the aperture of parabolic trough collector. The last one to the right of the equation is to express the heat exchange process between metal evacuated tube and the neighboring environment, which is normally within the glazed shield tube.

Similarly, the energy balance equation can be established for the heat-transfer fluid within the metal tube of parabolic trough collector, which can be expressed as

$$C_f \frac{dT_f}{d\tau} = A_f U_{bf} (T_b - T_f) - \dot{m} c_f (T_{fo} - T_{fi}) \quad (3.39)$$

in which  $C_f$  refers to the thermal power of heat-transfer fluid;  $c_f$  refers to the specific thermal capacity of heat-transfer fluid;  $T_{fi}$  refers to the inlet temperature of the tube;  $T_{fo}$  refers to the outlet temperature of the tube;  $\dot{m}$  refers to the mass flow.

$1/A_f U_{bf}$  and  $1/A_{am} U_{ba}$  are substituted with thermal resistance  $R_{bf}$  and  $R_{ba}$  separately, then Eq. (3.38) and Eq. (3.39) can be once again expressed as:

$$C_b \frac{dT_b}{d\tau} = S A_a - \frac{T_b - T_f}{R_{bf}} - \frac{T_b - T_a}{R_{ba}} \quad (3.40)$$

And

$$C_f \frac{dT_f}{d\tau} = \frac{T_b - T_f}{R_{bf}} - \dot{m} c_f (T_{fo} - T_{fi}) \quad (3.41)$$

Then Eq. (3.41) is reorganized into

$$\frac{T_b}{R_{bf}} = C_f \frac{dT_f}{d\tau} + \frac{T_f}{R_{bf}} + \dot{m} c_f (T_{fo} - T_{fi}) \quad (3.42)$$

On both sides of the above equation with time  $\tau$ , the derivative is taken, then

$$\frac{1}{R_{bf}} \frac{dT_b}{d\tau} = C_f \frac{d^2 T_f}{d\tau^2} + \frac{1}{R_{bf}} \frac{dT_f}{d\tau} + \dot{m} c_f \left( \frac{dT_{fo}}{d\tau} - \frac{dT_{fi}}{d\tau} \right) \quad (3.43)$$

In order to eliminate  $T_b$  from Eq. (3.40), Eq. (3.42) and Eq. (3.43) are substituted into it, then the two energy balance equations can be combined as

$$\begin{aligned} C_b C_f \frac{d^2 T_f}{d\tau^2} + \frac{C_b R_{ba} + C_f R_{ba} + C_f R_{bf}}{R_{bf} R_{ba}} \frac{dT_f}{d\tau} + \frac{T_f}{R_{bf} R_{ba}} &= \frac{A_a S}{R_{bf}} \\ -\frac{R_{ba} + R_{bf}}{R_{bf} R_{ba}} \dot{m} c_f (T_{fo} - T_{fi}) - C_b \dot{m} c_f \left( \frac{dT_{fo}}{d\tau} - \frac{dT_{fi}}{d\tau} \right) + \frac{T_a}{R_{bf} R_{ba}} \end{aligned} \quad (3.44)$$

Outlet temperature  $T_{fo}$  of heat-transfer fluid within the parabolic trough collector is selected as the lumped temperature of heat-transfer fluid within the metal absorber tube. Thus Eq. (3.44) is changed into

$$\begin{aligned} \frac{1 + (R_{bf} + R_{ba}) \dot{m} c_f}{C_b C_f R_{bf} R_{ba}} T_{fo} &= -\frac{d^2 T_{fo}}{d\tau^2} - \left( \frac{1 + \dot{m} c_f R_{bf}}{C_f R_{bf}} + \frac{R_{bf} + R_{ba}}{C_b R_{bf} R_{ba}} \right) \frac{dT_{fo}}{d\tau} \\ &\quad + \frac{\dot{m} c_f}{C_f} \frac{dT_{fi}}{d\tau} + \frac{(R_{bf} + R_{ba}) \dot{m} c_f}{C_b C_f R_{bf} R_{ba}} T_{fi} \\ &\quad + \frac{1}{C_b C_f R_{bf} R_{ba}} T_a + \frac{A_a}{C_b C_f R_{bf}} S \end{aligned} \quad (3.45)$$

Based on the above, a differential equation can be deduced

$$\frac{d^2 T_{fo}}{d\tau^2} + A \frac{dT_{fo}}{d\tau} + B T_{fo} = C \frac{dT_{fi}}{d\tau} + D T_{fi} + E S + F T_a \quad (3.46)$$

in which

$$A = \frac{1 + \dot{m} c_f R_{bf}}{C_f R_{bf}} + \frac{R_{bf} + R_{ba}}{C_b R_{bf} R_{ba}} \quad (3.47)$$

$$B = \frac{1 + (R_{bf} + R_{ba}) \dot{m} c_f}{C_b C_f R_{bf} R_{ba}} \quad (3.48)$$

$$C = \frac{\dot{m} c_f}{C_f} \quad (3.49)$$

$$D = \frac{(R_{bf} + R_{ba}) \dot{m} c_f}{C_b C_f R_{bf} R_{ba}} \quad (3.50)$$

$$E = \frac{A_a}{C_b C_f R_{bf}} \quad (3.51)$$

$$F = \frac{1}{C_b C_f R_{bf} R_{ba}} \quad (3.52)$$

Apparently,  $D = B - F$ , then, Eq. (3.46) can be reorganized into:

$$\frac{d^2T_{fo}}{d\tau^2} + A \frac{dT_{fo}}{d\tau} + B(T_{fo} - T_{fi}) = C \frac{dT_{fi}}{d\tau} + ES - F(T_{fi} - T_a) \quad (3.53)$$

Heat losses of parabolic trough collector toward the environment includes not only thermal convection with the surrounding air, but also the radiation heat exchange with the sky; thus the last column that represents heat loss in Eq. (3.53) can be expressed by two terms, one of which takes the form of a quadratic term, then Eq. (3.53) can be modified as

$$\frac{d^2T_{fo}}{d\tau^2} + A \frac{dT_{fo}}{d\tau} + B(T_{fo} - T_{fi}) = C \frac{dT_{fi}}{d\tau} + ES - F(T_{fi} - T_a) - G(T_{fi} - T_a)^2 \quad (3.54)$$

As a matter of fact, for application-level large-scale parabolic trough collectors, inlet temperature  $T_{fi}$  and outlet temperature  $T_{fo}$  of heat-transfer fluid within the collector that have been measured simultaneously do not correspond to the two parameters of Eq. (3.54) in time; a time lag relationship exists between  $T_{fi}$  and  $T_{fo}$ , and it is necessary to consider flow time  $\tau_p$  of heat-transfer fluid from the inlet to the outlet of parabolic trough collector. Therefore, the corresponding actual relationship of them in the dynamic test model can be expressed as:

$$T_{fo}(\tau + \tau_p) = f[T_{fi}(\tau)] \quad (3.55)$$

in which  $\tau_p$  depends on the length  $L$  of parabolic trough collector and mean flow rate  $v$  of heat-transfer fluid during the test, which can be expressed as

$$\tau_p = L/v \quad (3.56)$$

However, in order to achieve a concise model expression, in the dynamic test model of this section,  $T_{fo}(\tau + \tau_p)$  and  $T_{fi}(\tau)$  are no longer specially marked; instead, they will be considered during experimental data treatment, model identification and thermal performance prediction and calculation.

### 3.3.3.4 Establishment of Optical Model

An optical model is established based on  $S$  in Eq. (3.54), which aims at offering the physical relationship between it and solar DNI  $G_{DN}$  and the respective mathematical expression. As  $S$  is the section absorbed by the exterior wall surface of metal tube when solar DNI is perpendicular to the aperture of parabolic trough collector, it is a parameter that cannot be directly measured; it requires considering influences of parabolic trough concentrator reflection and transmission absorption of evacuated tube. This section of the model involves a parabolic trough collector truncation

factor  $\gamma$ , specular reflectance  $\rho$ , transmittance  $\tau$ , absorptance  $a$ , cosine factor, end loss correction factor and IAM in optical mechanism analysis.

Based on  $K_{\tau\alpha}$  defined in the equation, influence of variation of truncation factor  $\gamma$  along with the incidence angle shall also be integrated in IAM. Thus incidence angle correction factor  $K_{\gamma\tau\alpha}$  shall be expressed as Eq. (3.57), in which transmittance-absorptance-absorptance product ( $\gamma\tau\alpha$ ) is a collective property of parabolic trough collector, and varies along with the incidence angle  $\theta$ . In addition, when the incidence angle equals zero, vertical incidence of solar beam onto the aperture of parabolic trough collector occurs; then, in this case, the product is  $(\gamma\tau\alpha)_n$ .

$$K_{\gamma\tau\alpha} = \frac{(\gamma\tau\alpha)}{(\gamma\tau\alpha)_n} \quad (3.57)$$

An incidence angle comprehensive correction coefficient  $K(\theta)$  is defined as the product of cosine factor  $F_{\cos}$ , end loss correction factor  $F_{\text{end}}$  and incidence angle correction factor  $K_{\gamma\tau\alpha}$ , which can be expressed as

$$K(\theta) = F_{\cos}F_{\text{end}}K_{\gamma\tau\alpha} \quad (3.58)$$

$K_{\gamma\tau\alpha}$  is calculated by applying the following empirical equation

$$K_{\gamma\tau\alpha} = 1 + a_1 \frac{\theta}{\cos(\theta)} + a_2 \frac{\theta^2}{\cos(\theta)} \quad (3.59)$$

in which both  $a_1$  and  $a_2$  are constants to be determined through experiments.

Thus  $S$  can be expressed as

$$S = G_{\text{DN}}\rho(\gamma\tau\alpha)_n K(\theta) = G_{\text{DN}}\rho(\gamma\tau\alpha)_n F_{\cos}F_{\text{end}}K_{\gamma\tau\alpha} \quad (3.60)$$

Then the calculation equation of cosine factor  $F_{\cos}$ , calculation equation of end loss correction factor  $F_{\text{end}}$  and calculation Eq. (3.59) of incidence angle correction factor  $K_{\gamma\tau\alpha}$  are substituted into Eq. (3.60), and thus  $S$  can be expressed as

$$\begin{aligned} S &= G_{\text{DN}}\rho(\gamma\tau\alpha)_n \cos(\theta) \left[ 1 + a_1 \frac{\theta}{\cos(\theta)} + a_2 \frac{\theta^2}{\cos(\theta)} \right] \left[ 1 - \frac{f}{L} \tan(\theta) \right] \\ &= G_{\text{DN}} \left\{ \begin{aligned} &\rho(\gamma\tau\alpha)_n \cos(\theta) \left[ 1 - \frac{f}{L} \tan(\theta) \right] + \rho(\gamma\tau\alpha)_n a_1 \theta \left[ 1 - \frac{f}{L} \tan(\theta) \right] \\ &+ \rho(\gamma\tau\alpha)_n a_2 \theta^2 \left[ 1 - \frac{f}{L} \tan(\theta) \right] \end{aligned} \right\} \end{aligned} \quad (3.61)$$

in which  $\rho(\gamma\tau\alpha)_n$  refers to the maximum optical efficiency of parabolic trough collector.

In order to simplify the model, three constants are proposed, including

$$E_0 = E_\rho(\gamma\tau\alpha)_n \quad (3.62)$$

$$E_1 = E_\rho(\gamma\tau\alpha)_n a_1 \quad (3.63)$$

$$E_2 = E_\rho(\gamma\tau\alpha)_n a_2 \quad (3.64)$$

Then three functions relevant to incidence angle are defined as:

$$I_0(\theta) = \cos(\theta) \left[ 1 - \frac{f}{L} \tan(\theta) \right] \quad (3.65)$$

$$I_1(\theta) = \theta \left[ 1 - \frac{f}{L} \tan(\theta) \right] \quad (3.66)$$

$$I_2(\theta) = \theta^2 \left[ 1 - \frac{f}{L} \tan(\theta) \right] \quad (3.67)$$

Thus ES in Eq. (3.54) can be expressed as

$$ES = [E_0 I_0(\theta) + E_1 I_1(\theta) + E_2 I_2(\theta)] G_{DN} \quad (3.68)$$

In order to reduce the influence of fluctuation of measured solar DNI on the dynamic measurement model, the metal tube is divided into  $p$  sections along the flow direction of heat-transfer fluid, with the length of each section being referred to as  $L_p$ , which is shown in Fig. 3.27. Value of  $p$  depends on the flow time  $\tau_p$  of heat-transfer fluid passing from the inlet to the outlet of a parabolic trough collector and sampling interval  $\tau_s$  of experimental data, which can be expressed as

$$p = \tau_p / \tau_s \quad (3.69)$$

From section 1 to section  $p$ , solar DNI of heat-transfer fluid within each independent region corresponding to different time points are distinguished from each other. Thus by considering the heat-transfer fluid

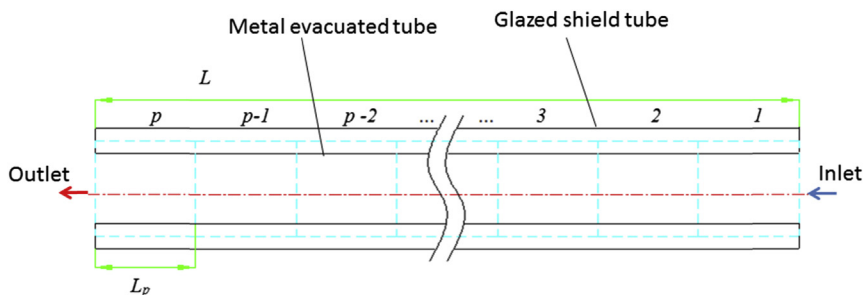


FIGURE 3.27 Section division of metal evacuated tube.

passing through the parabolic trough collector, the solar DNI  $G_p$  under averaging effect can be expressed as

$$G_p = \left\{ G_{DN}(\tau) + G_{DN}(\tau + \tau_s) + G_{DN}(\tau + 2\tau_s) + \dots \right. \\ \left. + G_{DN}[\tau + (p-2)\tau_s] + G_{DN}[\tau + (p-1)\tau_s] \right\} / p \quad (3.70)$$

$G_{DN}$  in Eq. (3.68) is replaced with  $G_p$ , and it is substituted into Eq. (3.54), then

$$\frac{d^2T_{fo}}{d\tau^2} + A \frac{dT_{fo}}{d\tau} + B(T_{fo} - T_{fi}) = C \frac{dT_{fi}}{d\tau} + [E_0 I_0(\theta) + E_1 I_1(\theta) + E_2 I_2(\theta)] \\ G_p - F(T_{fi} - T_a) - G(T_{fi} - T_a)^2 \quad (3.71)$$

### 3.3.3.5 Dynamic Test Model and Parameter Identification

Product of  $G_p$  and  $I_0(\theta)$  is referred to as  $G_{eni}$ , and both sides of Eq. (3.71) are divided by this variable. In addition, in terms of experimental data, the second derivative  $d^2T_{fo}/d\tau^2$  in Eq. (3.71) may bring uncertainty to the prediction results of dynamic test model, which thus can be removed. So, the ultimate expression of thermal performance dynamic test model of parabolic trough solar collector is

$$\frac{T_{fo} - T_{fi}}{G_{eni}} = e_0 + e_1 \frac{\theta}{\cos(\theta)} + e_2 \frac{\theta^2}{\cos(\theta)} + a \frac{1}{G_{eni}} \frac{dT_{fo}}{d\tau} + b \frac{1}{G_{eni}} \frac{dT_{fi}}{d\tau} \\ + c \frac{T_{fi} - T_a}{G_{eni}} + d \frac{(T_{fi} - T_a)^2}{G_{eni}} \quad (3.72)$$

in which

$$e_0 = \frac{E_0}{B}$$

$$e_1 = \frac{E_1}{B}$$

$$e_2 = \frac{E_2}{B}$$

$$a = -\frac{A}{B}$$

$$b = \frac{C}{B}$$

$$c = -\frac{F}{B}$$

$$d = -\frac{G}{B}$$

In the equation,  $e_0$ ,  $e_1$ ,  $e_2$ ,  $a$ ,  $b$ ,  $c$  and  $d$  are seven undetermined parameters. It is necessary for them to obtain experimental data for identification by utilizing parabolic trough collector test;  $G_{\text{eni}}$  is an effectively averaged direct irradiance while considering cosine loss, end section loss of tube and the influences of heat-transfer fluid that passes through the parabolic trough collector. It depends on the measured solar normal direct irradiance  $G_{\text{DN}}$ , cosine factor  $F_{\cos}$ , end loss correction factor  $F_{\text{end}}$ , flow time  $\tau_p$  of heat-transfer fluid passing from the inlet to the outlet of a parabolic trough collector, and sampling interval  $\tau_s$  of experimental data.

$dT_{f0}/d\tau$  and  $dT_{fi}/d\tau$  are two first-order derivatives, which need to be based on the discretization method in the governing equation of numerical heat transfer by utilizing the differential expression of derivatives deduced through the Taylor expansion method, and handled by applying the mean difference method, then

$$\frac{dT_{f0}}{d\tau}(n) = \frac{T_{f0}(n+1) - T_{f0}(n-1)}{2\Delta\tau}$$

$$\frac{dT_{fi}}{d\tau}(n) = \frac{T_{fi}(n+1) - T_{fi}(n-1)}{2\Delta\tau}$$

in which  $n$  refers to the quantity of experimental data during the test ( $n > 1$ );  $\Delta\tau$  refers to the equivalent time interval of two random adjacent numbers of experimental data.

The first three terms to the right of Eq. (3.72) refer to optical characteristics of parabolic trough collector varying along with the incidence angle; the fourth and fifth terms refer to the effective thermal capacity of absorber and heat-transfer fluid of parabolic trough collector; whereas the last two terms refer to heat losses of parabolic trough collector. They are mainly determined by the difference between inlet temperature of heat-transfer fluid within the parabolic trough collector and ambient air temperature, which also include the dual influences of radiation heat exchange loss and convection heat exchange loss. In addition, there is a certain relationship between the dynamic test model and the steady state test model in ASHRAE 93 standard.

Although Eq. (3.72) is not a linear equation, a linear expression can still be obtained through the treatment toward the respective quadratic term, based on which, thermal performance dynamic test model of parabolic trough solar collector applies MLR on the basis of the least-square serial methods as the method to identify the seven undetermined coefficients.

In order to verify the dynamic test model, it shall be applied in the parabolic trough solar collector in this research. Thus by using the experimental condition I test data in Section 3.3.3.6, and applying the

mathematical method of MLR, an identified equation for thermal performance dynamic test of parabolic trough collector can be obtained as follows:

$$\begin{aligned} T_{fo} - T_{fi} = & \left[ 0.182 - 0.00731 \frac{\theta}{\cos(\theta)} + 0.000106 \frac{\theta^2}{\cos(\theta)} \right] G_{eni} - 68.379 \frac{dT_{fo}}{d\tau} \\ & + 33.941 \frac{dT_{fi}}{d\tau} - 0.00571(T_{fi} - T_a) - 0.0000217(T_{fi} - T_a)^2 \end{aligned} \quad (3.73)$$

Regression results of seven coefficients of  $e_0, e_1, e_2, a, b, c$  and  $d$  are analyzed. One major index is the coefficient of determination  $R^2$ , which is 0.86; it measures the fitting degree of the independent variable of regression toward the dependent variable. Other major indices include least-square estimated value and standard error, which have been listed in Table 3.7.

### 3.3.3.6 Thermal Performance Prediction of Dynamic Test Model

The dynamic test model assumes the first-order derivative term of outlet temperature of heat-transfer fluid within the parabolic trough collector to be zero, calculates  $T_{fo}$  by utilizing the known variables  $G_{eni}, \theta, T_{fi}$  and  $T_a$ , and uses it as the initial value; then it applies the Newton iteration method, and finally predicts a reasonable outlet temperature of heat-transfer fluid within the parabolic trough collector. In order to weaken the influences caused by test conditions fluctuation, time  $\tau_p$  of heat-transfer fluid passing through the parabolic trough collector is used

TABLE 3.7 Table of Dynamic Test Model Parameter Regression Analysis

Coefficient	Least-Square Estimated Value	Standard Error	$t_i$	$P(> t )$
$e_0$	0.182	$1.07 \times 10^{-2}$	17.042	0
$e_1$	$-7.34 \times 10^{-3}$	$4.77 \times 10^{-4}$	-15.301	0
$e_2$	$1.06 \times 10^{-4}$	$7.45 \times 10^{-6}$	14.198	0
$a$	-68.379	25.703	-2.660	$8.13 \times 10^{-3}$
$b$	33.941	2.190	15.500	0
$c$	$-5.66 \times 10^{-3}$	$3.84 \times 10^{-4}$	-14.856	0
$d$	$-2.17 \times 10^{-5}$	$1.88 \times 10^{-6}$	-11.543	0

$t_i$  refers to the test statistics, which is equivalent to ratio of the least-square estimated value to the standard error of regression coefficient;  $p$  refers to the degree of freedom, which is equivalent to the probability of  $t$  distribution being larger than the absolute value of  $t_i$  under the difference of the quantity of experimental data and that of regression coefficients.

as the reference when implementing smoothing processing toward the predicted outlet temperature data of heat-transfer fluid within the parabolic trough collector.

In order to clearly express the prediction results, difference between the measured and the predicted outlet temperatures of heat-transfer fluid within the parabolic trough collector is offered as the absolute error, and used to divide the measured outlet temperature of heat-transfer fluid within the parabolic trough collector in order to obtain the ratio that can be used as the relative error of prediction results.

Furthermore, in order to demonstrate the working effect of the collector, it is also necessary to calculate the collector efficiency, which refers to the ratio of the output energy from parabolic trough collector to the solar DNI projected into the concentration field during operation. Equation in ASHRAE 93 standard is applied in this book, and solar irradiance  $G_{bp}$  that considers the cosine effect is selected as the denominator of efficiency calculation equation of energy projected into the concentration field, which is shown in Eq. (3.74). There is also some literature that has only applied solar direct normal irradiation  $G_{DN}$  as the denominator of the efficiency equation without considering the influence of cosine loss.

$$\eta = \frac{\int c_{oil} \dot{m} (T_{fo} - T_{fi}) d\tau}{A_a \int G_{bp} d\tau} \quad (3.74)$$

in which  $c_{oil}$  refers to the specific thermal capacity of synthetic oil used in this book. The manufacturer has provided its values corresponding to different temperatures, which are shown in Fig. 3.28.

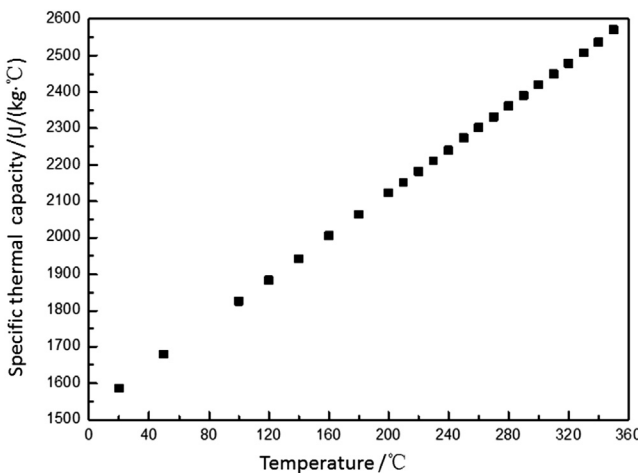


FIGURE 3.28 Variation of specific thermal capacity of synthetic oil.

In order to simplify the calculation, based on the observation, these data have high degrees of linearity. Thus according to these data, a linear equation can be obtained as follows through fitting method:

$$c_{\text{oil}} = 1528.32 + 2.973T_{\text{oil}} \quad (3.75)$$

in which  $T_{\text{oil}}$  refers to the synthetic oil temperature. In order to specify the reasonability and precision of this method, four typical experimental conditions are discussed separately as follows [30].

### 3.3.4 Experimental Condition I

Based on the meteorological data of Experimental Condition I and collector inlet fluid data  $G_{\text{DN}}$ ,  $T_f$  and  $T_a$ , as well as the solar radiation incidence angle  $\theta$  relevant to solar position and solar irradiance  $G_{\text{eni}}$  that considers cosine effect and end effect correction, predicted value of fluid outlet temperature of parabolic trough collector can be obtained through iteration calculation by applying Eq. (3.72).

The calculated value and predicted value have been compared in Fig. 3.29. D and M separately refer to outlet temperatures of heat-transfer fluid within the parabolic trough collector obtained through the dynamic prediction method and experimental measurement. Within the test period of Experimental Condition I, namely from 10:07 to 12:46, the predicted value perfectly fits to the experimental value. The obvious difference of both values appears within 2 min after 11:16. The maximum outlet

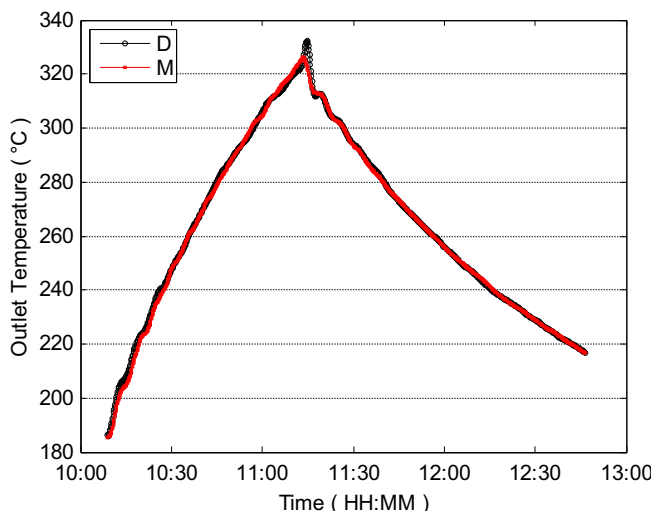


FIGURE 3.29 Predicted value of collector outlet temperature by dynamic model under experimental condition I compared with the experimental measurement.

temperature  $326^{\circ}\text{C}$  of heat-transfer fluid within the parabolic trough collector obtained through experimental measurement appears at 11:16, whereas the predicted maximum outlet temperature  $332^{\circ}\text{C}$  of heat-transfer fluid within the parabolic trough collector by the dynamic test equation appears at 11:17. Such a difference is mainly caused by the necessary time to rotate the aperture of receiver of parabolic trough collector to the poor-light side. Within this tracker adjustment period, the actual incidence of solar direct radiation onto the aperture surface of a parabolic trough collector cannot reduce to zero instantaneously. Thus prediction by applying this dynamic test model may result in lagging and errors.

By drawing the tendency of differences between the measured and the predicted outlet temperatures of heat-transfer fluid within the parabolic trough collector, Fig. 3.30 has clearly indicated the quantity of predicted values that exceeds the measured value by  $-4^{\circ}\text{C}$  within the parabolic trough collector adjustment period; however, within the entire test period, most of the differences between the measured value and the predicted value fall in a range of  $-4$  and  $2^{\circ}\text{C}$ , especially for the predicted value in the cooling process, which are within  $\pm 1^{\circ}\text{C}$  of the measured value. As shown in Fig. 3.31, further analysis on the relative error also indicates that the relative error of the predicted value mainly appears within  $\pm 1\%$ .

In Fig. 3.32, for the parabolic trough collector output power variation curve D predicted through the dynamic test model and the output power

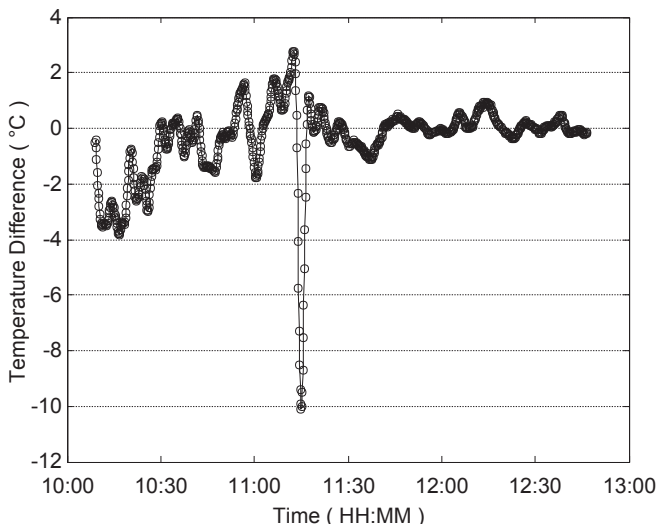


FIGURE 3.30 Absolute error of dynamic model on the predicted value under experimental condition I.

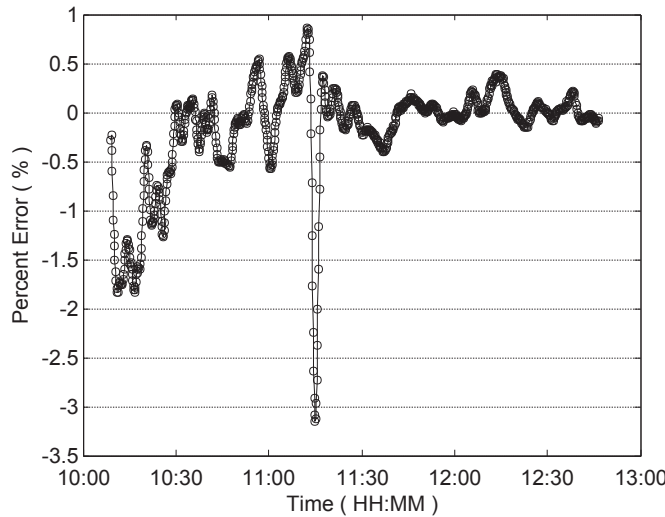


FIGURE 3.31 Relative error of dynamic model on the predicted value under experimental condition I.

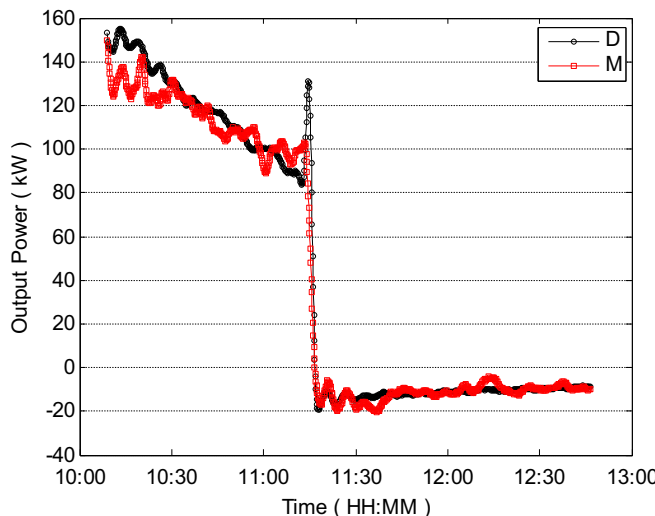


FIGURE 3.32 Predicted value of collector output power by dynamic model under experimental condition I.

variation curve M obtained through the measured value calculation, differences of some values from beginning of the test and parabolic trough collector state adjustment period have exceeded 20 kW, but in general, no matter for the heating process or cooling process of parabolic

trough collector, most of the data coincide with each other. This is because an undetermined coefficient of dynamic test model has been obtained through regression of this group of experimental data.

### 3.3.5 Experimental Condition II

Based on  $G_{DN}$ ,  $T_{fi}$  and  $T_a$  of Experimental Condition II, by applying Eq. (3.72) of dynamic test equation for parabolic trough collector, Fig. 3.33 has drawn the dynamic test model prediction curve D and experimental measurement curve M of outlet temperature of heat-transfer fluid within the parabolic trough collector. Within the entire test period, namely from 12:10 to 13:01, parabolic trough collectors have all remained in the tracking status. Thus the measured outlet temperature of heat-transfer fluid within the parabolic trough collector increases from 185 to 307°C, and the outlet temperature of heat-transfer fluid within the parabolic trough collector predicted through the dynamic test model also increases from 185 to 306°C. Except for some slight deviation after 12:39, temperature increase tendency of prediction curve and measurement curve are consistent with each other.

In Fig. 3.34, the specific value corresponding to this deviation has been clearly presented, which is caused by a short-term cloudy. Within 1 min before or after 12:45, the dynamic model has predicted appearance of the maximum absolute error of outlet temperature of heat-transfer fluid within the parabolic trough collector. Some data points indicate that the measured value is 3°C higher than the predicted value. Within the period from 12:53

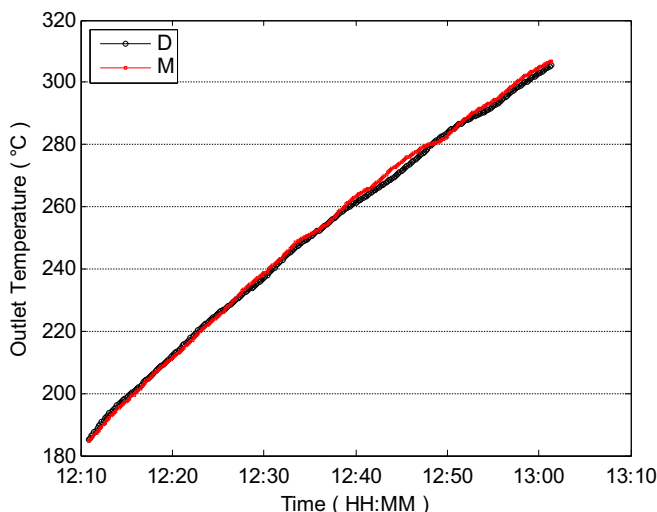


FIGURE 3.33 Predicted value of collector outlet temperature by dynamic model under experimental condition II.

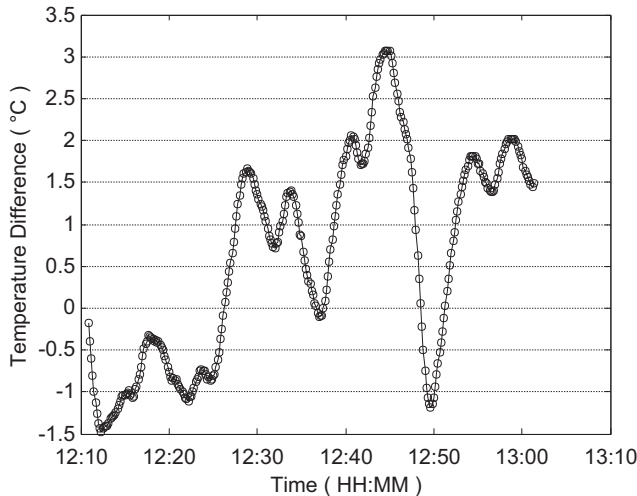


FIGURE 3.34 Absolute error of dynamic model on the predicted value under experimental condition II.

to the end of the test, absolute errors of some predicted values fluctuate between 1.5 and 2°C. However, before 12:40, the difference between the measured and the predicted outlet temperatures of heat-transfer fluid within the parabolic trough collector mainly concentrates within  $\pm 1.5^\circ\text{C}$ .

Based on the relative error analysis, as shown in Fig. 3.35, relative error of the predicted values mainly exists within  $\pm 0.8\%$ ; even the maximum

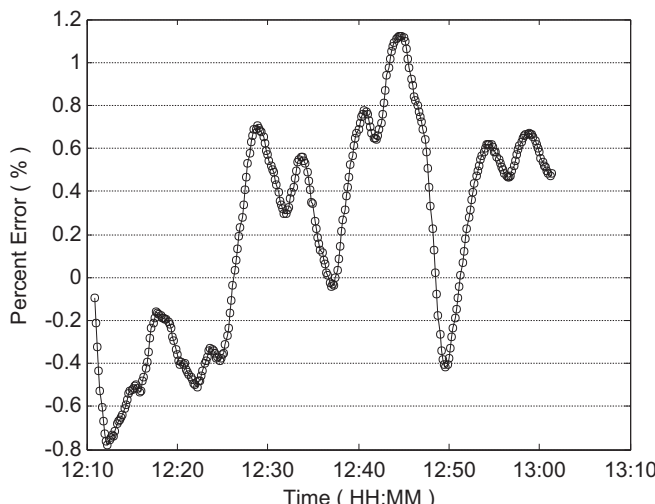


FIGURE 3.35 Relative error of dynamic model on the predicted value under experimental condition II.

relative error within 1 min before or after 12:45 is less than 1.2%, which is also at the nearly same level with the relative error under Experimental Condition I. It indicates that under the natural condition without excessive fluctuations and under the stable operating condition of parabolic trough collectors, even if the inlet temperature of heat-transfer fluid within the parabolic trough collector constantly increases, the dynamic test model for parabolic trough collector is able to show a considerable thermal performance prediction effect.

For parabolic trough collector output power predicted through the dynamic test model and calculated based on the experimental measurement data, as shown in Fig. 3.36, their values mainly vary within a range of 110–130 kW. Although dynamic test model prediction curve D and value calculation curve M through experimental measurement within 1 min before or after 12:45 have been obviously distinguished from each other, it is also the point where the maximum absolute error of predicted values of dynamic test model lies; however, difference between and among these values at the same time point has not exceeded 20 kW.

By focusing on Experimental Condition II, comparison and error analysis of predicted value of thermal performance dynamic test model of parabolic trough collector, experimental measurement data and the respective calculated value have demonstrated that for the test conditions similar to experimental data applied in the coefficient regression of the model, the dynamic test model is able to achieve satisfactory thermal performance prediction results of parabolic trough collector.

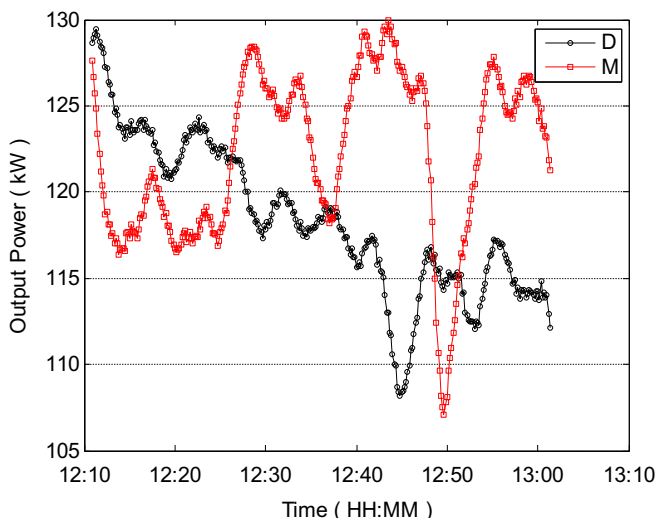


FIGURE 3.36 Prediction of dynamic model on collector output power under experimental condition II.

### 3.3.6 Experimental Condition III

During the period from 12:32–11:32, as influenced by frequent obnubilation, solar DNI of Experimental Condition III fluctuates greatly between  $700 \text{ W/m}^2$  and zero. Due to such fluctuation, no matter for the experiment measured value of inlet temperature of heat-transfer fluid within the parabolic trough collector or the respective calculated value based on  $G_{DN}$ ,  $T_{fi}$  and  $T_a$  through the dynamic test model, they have all undergone significant changes, which is shown in Fig. 3.37. Especially for the predicted value of the dynamic test model, such influence is more intensive. For example, within 3 min before or after 10:50, predicted value of the dynamic test model on the inlet temperature of heat-transfer fluid within the parabolic trough collector primarily increases from the minimum value  $264^\circ\text{C}$  to the maximum value  $287^\circ\text{C}$ , then drops to  $266^\circ\text{C}$ . The two changes have both exceeded  $20^\circ\text{C}$ . Yet within the same period, the difference between the maximum and the minimum experiment measured values is not more than  $10^\circ\text{C}$ . However, it is a remarkable fact that predicted value fluctuation of thermal performance dynamic test model of parabolic trough collector has always been centering the experiment measured value, and both of them enjoy a consistent variation tendency.

Fig. 3.38 has further indicated that although the maximum value of the difference between the measured and the predicted outlet temperatures of heat-transfer fluid within the parabolic trough collector may approach  $\pm 15^\circ\text{C}$ , absolute error of the predicted value of dynamic test model mainly exists within  $\pm 5^\circ\text{C}$  with an approximate symmetric distribution

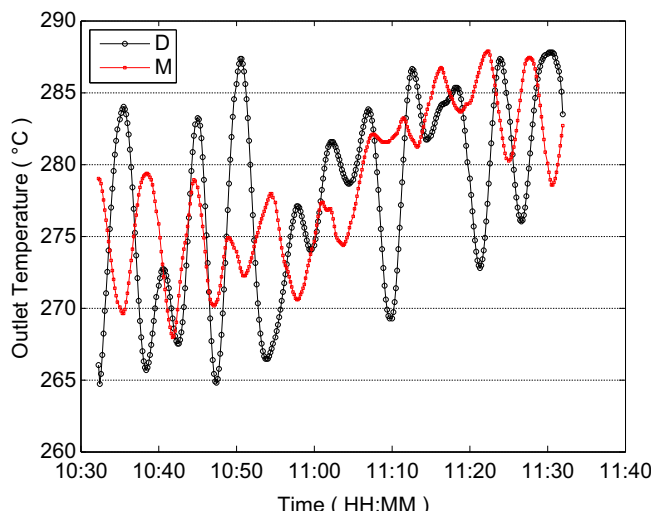


FIGURE 3.37 Predicted value of dynamic model on collector outlet temperature under experimental condition III.

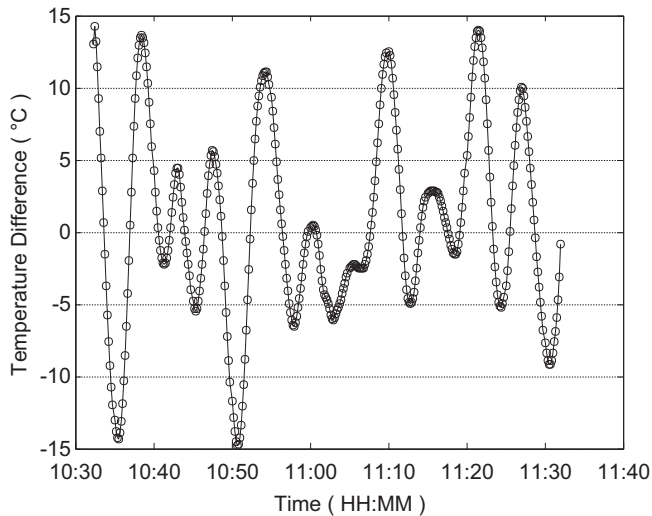


FIGURE 3.38 Absolute error of dynamic model on predicted value under experimental condition III.

around zero. For long-term thermal performance evaluation of parabolic trough solar collector, such distribution is conducive for offsetting some prediction errors.

In Fig. 3.39, according to the relative error analysis, for test conditions containing the significant fluctuation of solar DNI, the maximum

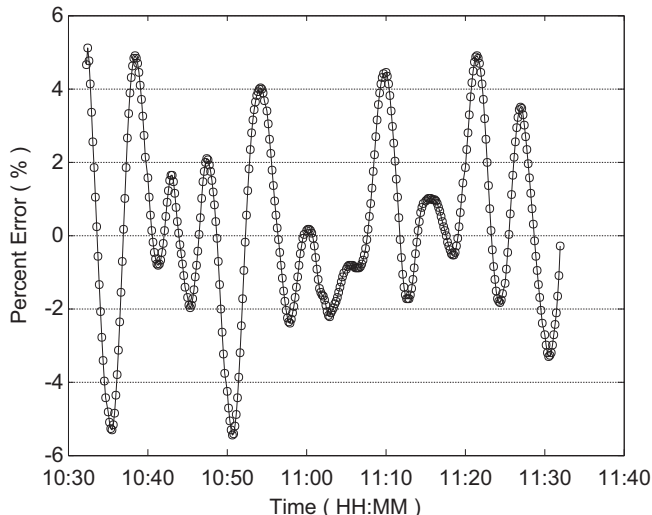


FIGURE 3.39 Relative error of dynamic model on predicted value under experimental condition III.

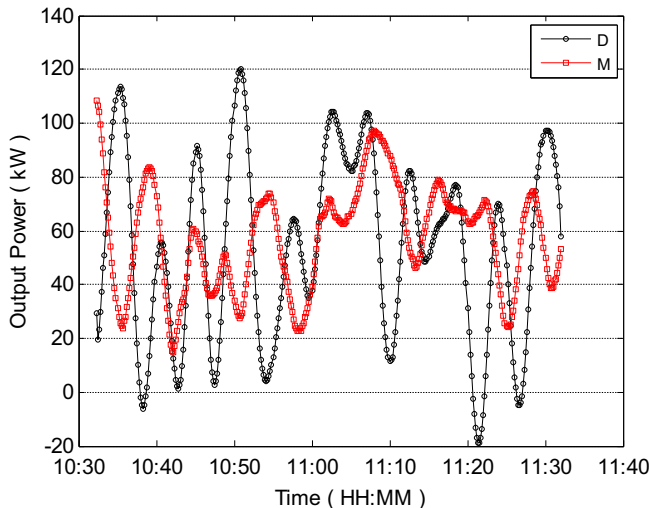


FIGURE 3.40 Prediction of dynamic model on collector output power under experimental condition III.

relative error of outlet temperature of heat-transfer fluid within the parabolic trough collector predicted by the dynamic test model has exceeded  $\pm 5\%$ , but the relative error has still mainly concentrated within  $\pm 2\%$ ; in addition, it has always had approximate symmetric fluctuation around zero.

According to the variation of parabolic trough collector output power within a range of 15–110 kW calculated on the basis of the experiment measured value, as shown in Fig. 3.40, in the predicted value of dynamic test model on parabolic trough collector output power, there are individual data points that are less than zero. This is obviously incorrect. It has also indicated that in case of significant fluctuation of solar DNI, dynamic test model is not able to ensure the precision of every transient value of parabolic trough collector output power.

Based on test conditions under Experimental Condition III, by comparing the predicted value of thermal performance dynamic test model of parabolic trough collector and the experiment measured value as well as the respective calculated value, absolute error, and relative error, they all indicate that in case of being influenced by adverse condition of frequent obnubilation, the dynamic test model is not able to ensure the high precision of every transient predicted value. However, its predicted data are able to fluctuate around the measured value, so that the long-term thermal performance prediction effect of parabolic trough collector can be ensured.

### 3.3.7 Experimental Condition IV

Based on the measured data under Experimental Condition IV, for two cooling processes of parabolic trough collector, outlet temperature of heat-transfer fluid of parabolic trough collector predicted by the dynamic test model separately decreases from 338 to 166°C and from 231 to 168°C, the corresponding experiment measured values separately decrease from 325 to 168°C and from 222 to 170°C, which are shown in Fig. 3.41. Although there is a significant deviation of the predicted value and experiment measured value around 10:23 and 14:12, namely during tracking status variation of parabolic trough collector, both of them coincide with each other as a whole.

In Fig. 3.42, within the period of 10:09–10:23, namely the primary thermal charging stage of parabolic trough collector, the absolute error of outlet temperature of heat-transfer fluid within the parabolic trough collector predicted by the dynamic test model exceeds the experiment measured value by  $-5 \sim -10^\circ\text{C}$ ; it even exceeds by  $-15^\circ\text{C}$  at certain data points. However, for the subsequent primary cooling stage of parabolic trough collector, absolute error of the predicted value of dynamic test model mainly exists within  $\pm 1^\circ\text{C}$ . When once again adjusting the parabolic trough collector to be in the tracking status, the reheating stage of parabolic trough collector appears between 13:24 and 14:12. Absolute error of the predicted value of dynamic test model concentrates within  $\pm 10^\circ\text{C}$ , and presents an approximate symmetric distribution around their zero value. In the last cooling stage of parabolic trough collector, predicted value of dynamic test model is  $3^\circ\text{C}$  less than the experiment measured value.

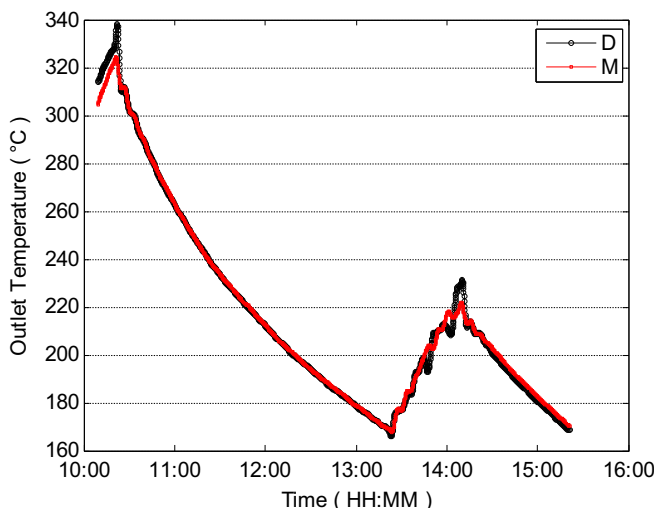


FIGURE 3.41 Predicted value of dynamic model on collector outlet temperature under experimental condition IV.

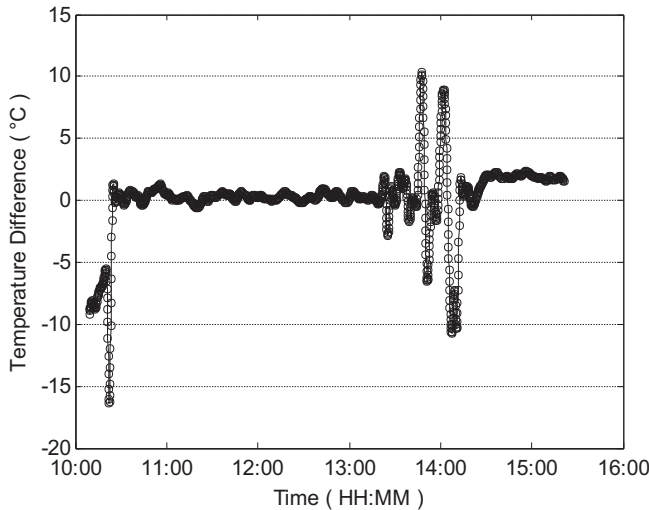


FIGURE 3.42 Absolute error of dynamic model on predicted value under experimental condition IV.

In Fig. 3.43, according to the relative error analysis, relative error of outlet temperature of heat-transfer fluid within the parabolic trough collector predicted by the dynamic test model does not exceed  $\pm 5\%$ , in which the two data points when the relative error approaches  $\pm 5\%$  mainly appear in the status adjustment of parabolic trough collector and

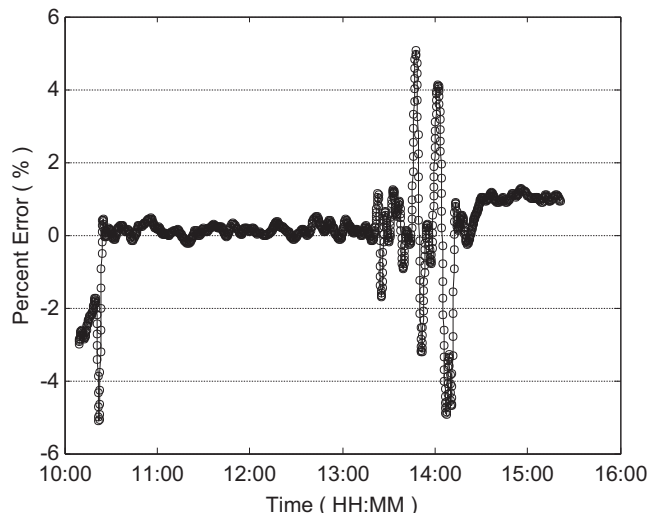


FIGURE 3.43 Relative error of dynamic model on predicted value under experimental condition IV.

the reheating stage under influences of intensive cloud. However, for two cooling processes of parabolic trough collector, relative error of the predicted value of dynamic test model mainly exists within  $\pm 1\%$ . As shown in Fig. 3.44, for the primary heating process of parabolic trough collector, predicted value of the dynamic test model on the output power of parabolic trough collector mainly varies between 145 and 183 kW; whereas the calculated value of experiment test data falls in a range of 100–111 kW, and this is the testing stage with the largest deviation of these two values. During 10:23–13:24, in the primary cooling process of parabolic trough collector, these two values fall in a range of  $-2 \sim -19$  kW with a consistent variation tendency. The dynamic test model has manifested excellent prediction effects.

Based on test conditions under Experimental Condition IV, by comparing and analyzing the predicted value of dynamic test model and the experiment measured value as well as the respective calculated value, the absolute error of  $\pm 3^\circ\text{C}$  and relative error of  $\pm 1\%$  have indicated that thermal performance dynamic test model of parabolic trough solar collector is able to ensure the prediction effect in the cooling process of parabolic trough collector.

In order to further demonstrate the effect of thermal performance dynamic test model of parabolic trough collector in engineering applications, based on the four typical experimental conditions, and according to Eq. (3.74), output energy and mean thermal efficiency of parabolic trough collector corresponding to each test period can be separately calculated, results of which have been listed in Table 3.8.

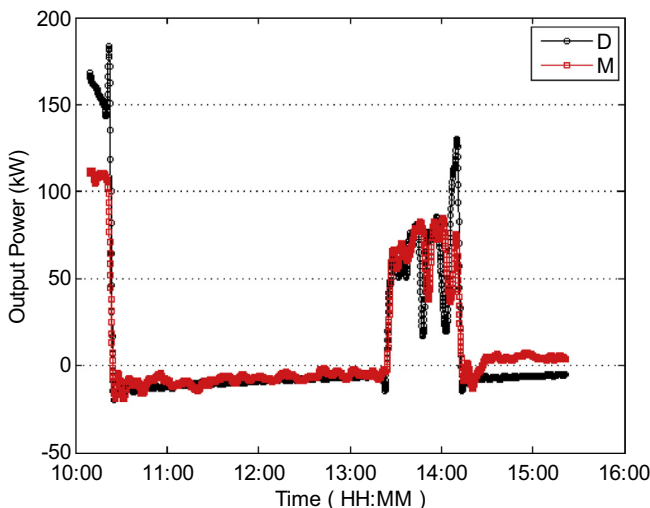


FIGURE 3.44 Prediction of dynamic model on collector output power under experimental condition IV.

TABLE 3.8 Predicted Value of Dynamic Test Model and Experiment Measured Value and Respective Calculated Value

Experimental Condition	Time	Model-Predicted Output Energy/MJ	Output Energy Calculated Based on Measured Value/MJ	Solar Energy/MJ	Model-Predicted Thermal Efficiency/%	Thermal Efficiency Calculated Based on Measured Value/%	Error/%
1	10:09–12:47	418.56	394.92	1296.9	32.27	30.45	1.82
2	12:11–13:01	359.84	371.56	1006.4	35.75	36.92	-1.16
3	10:32–11:32	194.94	206.58	676.18	28.83	30.55	-1.72
4	10:09–5:21	192.03	198.88	783.57	24.51	25.38	-0.87

By integrating the above analysis, based on the prediction effect of dynamic test model on parabolic trough collector, experimental requirements and process of performance dynamic test of parabolic trough collector can be summarized: Thermal performance dynamic test of parabolic trough solar collector shall be conducted under a clear days; the whole testing process is required to enjoy a solar DNI over 700 W/m<sup>2</sup>; variation of volume flow of heat-transfer fluid passing through the parabolic trough collector shall be within ±2%. According to the scope of application of parabolic trough collector, a specific variation scope of outlet temperature of heat-transfer fluid within the specific parabolic trough collector can be determined. The testing process consists of two stages, namely outlet temperature ascent process of heat-transfer fluid within the parabolic trough collector under normal tracking concentrating conditions, and outlet temperature descent process of heat-transfer fluid within the parabolic trough collector under conditions when adjusting the aperture of receiver of parabolic trough collector to the poor-radiation side. In addition, the test shall be conducted around the time of the day when the maximum incident angle appears; for example, for the most common parabolic trough solar collector arranged horizontally on the north-south axis, the tracking test for parabolic trough collector shall be conducted within 2 h before or after high noon every day.

### **3.4 BASIC DATA REQUIRED BY POWER PLANT DESIGN**

---

- 1.** Solar radiation data and meteorological data of CSP plant, neighboring areas and local meteorological stations.
- 2.** Soil and Water Conservation Program Report
- 3.** Water Resources Argumentation Report
- 4.** Geological Survey Report
- 5.** Geological Hazard Risk Evaluation Manual
- 6.** 1:50,000 topographic map within 10 km of extended site scope and 1:2000 topographic map within site scope
- 7.** Process Gas and Water-Supply Conditions
- 8.** Correspondence of Uncovered, Identified Major Mineral Resources within Land Use Scope of Site Selection during Project Construction
- 9.** Grid Access System Report
- 10.** Environmental Impact Assessment Report
- 11.** Price data of local construction materials, equipment and labor cost

### 3.5 MAJOR PARAMETERS AND PRINCIPLES OF DESIGN

1. Installed capacity of power plant, estimated annual power generation.
2. Concentrating mode: Tower-type, parabolic trough-type or others, concentrator area.
3. Thermal-absorbing and heat-transfer medium and the respective maximum working temperature: Water/steam, synthetic oil and the respective maximum working temperature, molten salt, and its maximum working temperature
4. Requirements on energy storage device: Quantity of thermal storage tanks, thermal storage capacity, temperature, category of materials, category and quantity of circulating pumps
5. Evaporator: Heat exchange pattern, volume, applicable medium, circulating pump
6. Auxiliary boiler: Whether there is any auxiliary heating system, type of auxiliary fuel (fuel or natural gas), annual consumption and source of auxiliary fuel.
7. Shape and dimension of receiver: Cavity diameter and cylinder size of tower-type; length and diameter of the evacuated tube of parabolic trough-type.
8. Rated steam inlet parameters of steam turbine (main steam pressure and temperature), rated power, minimum stable load, unit thermal efficiency.
9. Heat-transfer fluid circulating equipment: Circulating pump, expansion tank etc.
10. Control: Concentration field control mode; entire field control mode.
11. Concentrator cleaning facilities and method: Manual cleaning, machine cleaning, dry cleaning, washing.
12. Steam turbine condensed mode, dry-cooled or wet-cooled, annual water consumption.
13. Efficiency: Annual mean efficiency of concentration field, annual maximum efficiency of concentration field, annual mean efficiency of receiver, annual mean efficiency of power plant.
14. Power plant initiation time under typical solar irradiation and meteorological conditions.
15. CSP plant access system voltage grade and boost mode.
16. Thermal power plant grid access metering gateway point designed at the division point of property.
17. Permanent engineering land use area.

18. Maximum annual water consumption during project construction and total annual water consumption during project operation.
19. Power plant construction period: In northwestern areas of China, the construction period of a 50 MW power plant normally does not exceed 30 months; whereas that of a 100 MW power plant normally does not exceed 42 months.
20. Power plant operation period: Normally to be 25 years

### **3.6 DESCRIPTION OF GENERAL PARAMETERS OF THE POWER PLANT**

---

Below are the items described in the overall technical parameters of an CSP plant; after completion of design, explanation to the following items shall be provided.

1. Concentrator: Area and dimension of aperture of a single concentrator. Tracking modes include azimuth/altitude angle, working wind speed corresponding to open-loop/close-loop design precision, protective wind speed.
2. Concentration field: Concentrating forms include parabolic trough and tower, etc. Maximum power projected on the receiver from the concentration field, concentration field aperture area.
3. Receiver: Structural forms mainly include cavity-type, cylinder-type, and evacuated tube-type. Receiver water inlet temperature, receiver outlet pressure, receiver outlet temperature, receiver fluid flow rate.
4. Steam turbine generator: Inlet steam pressure of steam turbine; inlet steam temperature of steam turbine; maximum temperature of condensate water; generator outlet voltage.
5. Thermal storage: Thermal capacity, temperature, volume, necessary time for full-load power generation of steam turbine.
6. Backup emergency power supply: power, AC uninterruptible power supply and 220 V DC power supply
7. Power access: Voltage, transformer power
8. Grid access: Voltage, current, and time period

### **3.7 CALCULATION OF ANNUAL POWER GENERATION**

---

In a regular project, it is normally the owner who firstly proposes to construct a power plant with an expected capacity, and the design unit shall calculate annual power generation of the power plant and

concentration field area based on the capacity requirement proposed by the owner. Annual power generation of the power plant is related to solar to electricity conversion efficiency at the design point, concentration field area, and solar irradiation resources. The specific calculation process has been explained in details as follows.

### 3.7.1 Calculation by Applying the Design Point Method

In annual power generation calculation, except for such invariable factors as solar irradiation resources and weather, others are all variables.

The key point for annual power generation calculation is to determine the collector field power, which includes the concentration field area and receiver power. The concentration process, thermal receiver, thermal storage, and heat exchange are coupled to power generation, which shall be calculated by using multiple factors simultaneously on the basis of system energy balance. At a typical time point, such as the design point, the concentration field area depends on the rated input of steam turbine, rated input of thermal storage, and operating mode of power plant corresponding to the design point. It is normally required that at the design point, the concentration field provides energy to the receiver, output power of which shall be not less than the sum of rated input of steam turbine and rated input of thermal storage. At this moment, the power plant is basically able to ensure the full-load power generation during the day and several hours of power generation during the night. In this case, the rated input power of thermal storage shall be the ratio of the capacity of thermal storage to its thermal-charging operation hours.

*Fig. 3.45* shows the annual power generation calculation process. Firstly, irradiation and meteorological conditions shall be determined; then, a concentration field area shall be assumed. When considering the output of concentration field as the input of receiver, the output power of receiver shall be equivalent to the sum of required input power of steam turbine and thermal storage. In case of the condition not being satisfied, it is necessary to reassume the concentration field area until the request is satisfied.

After determining the concentration field area, the system efficiency can be calculated based on the concentrating efficiency, receiver efficiency, generating efficiency, etc. Then, annual power generation of the system can be calculated.

Thus the basic idea for calculating the annual power generation is that under specified geographic location, meteorological conditions, solar irradiation conditions, steam turbine capacity and thermal storage capacity, the concentration field area and the annual mean generating efficiency of CSP generation system can be determined.

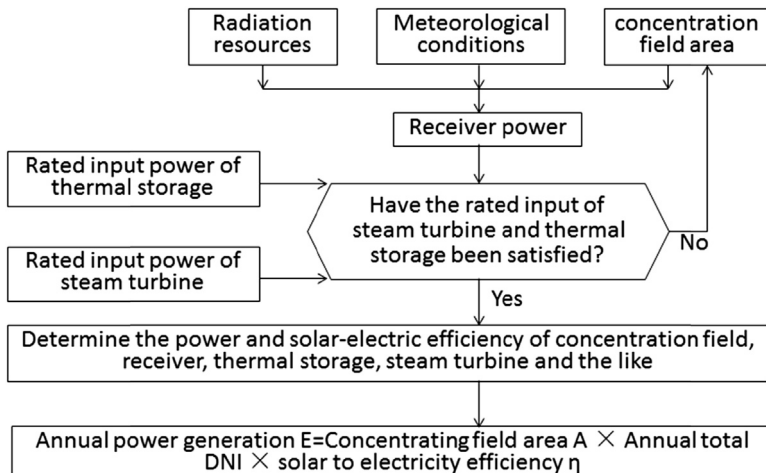


FIGURE 3.45 Annual power generation calculation process.

Thermal storage capacity normally depends on the night peak modulation power supply capacity (product of power and generation hours). In case of only focusing on night power generation, concentration field area shall satisfy the rated thermal request of steam turbine corresponding to night generation hours. However, such operational condition has been rarely seen. In case of no thermal storage, output of concentration field at the design point is the rated input of steam turbine.

Step I: The design point irradiation and meteorological conditions, and the steam turbine rated power  $P_{TURBINE}$  are defined.

Step II: The concentration field area is assumed to be  $A$ .

Step III: Power plant output power at the design point can be calculated according to the process described in Table 3.1. In case that  $P$  satisfies:

$$|P - P_{TURBINE}| < \varepsilon \quad (3.76)$$

Then the calculation process ends, and concentration field area  $A$  is obtained. Otherwise, a new concentration field area shall be assumed for another calculation, until Eq. (3.76) is satisfied.  $\varepsilon$  refers to the allowed margin of error of iteration, which shall be determined before calculation, such as  $\varepsilon = 50$  kW.

System photoelectric efficiency  $\eta$  at the design point is calculated as follows: assuming  $DNI = 1000 \text{ w/m}^2$  at the design point

$$\eta = \frac{P_{TURBINE}}{1000 A} \quad (3.77)$$

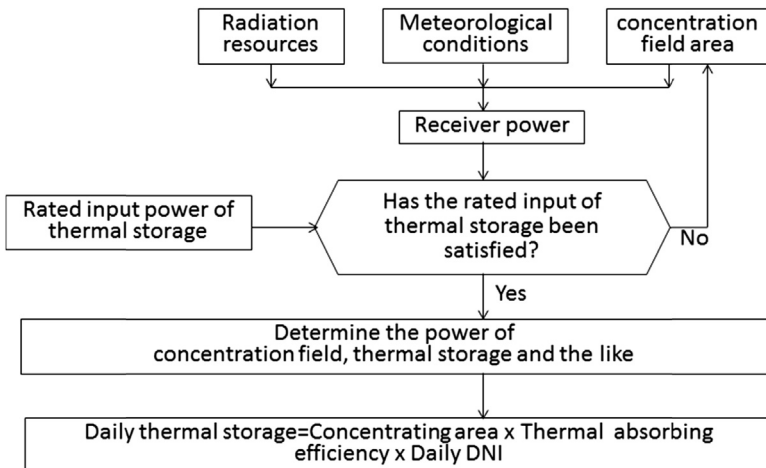


FIGURE 3.46 Determination of thermal storage and concentrating area.

In case of substituting the annual mean efficiency with the photoelectric efficiency of the system, the annual power generation  $E$  can be calculated as follows:

$$E = \text{DNI} \times A \times \eta \quad (3.78)$$

In case of the system being equipped with a thermal storage, after determining the corresponding concentration field area of steam turbine, the corresponding concentration field area of thermal storage can be calculated, which is shown in Fig. 3.46. Thermal storage is calculated in a different way with thermal radiation in the denomination of "day." For a system equipped with a thermal storage, the total area of the concentration field equals to the sum of the concentration field area calculated according to Fig. 3.45 corresponding to the steam turbine and the required concentration field area corresponding to thermal storage.

### 3.7.2 Calculation Example for Annual Power Generation

It is known that in a certain location, the annual total DNI = 1850 kWh/m<sup>2</sup>, annual mean solar irradiance is 750 W/m<sup>2</sup>, and annual mean ambient air temperature is 10°C. Steam turbine parameters of the 50 MW power tower plant equipped with 4 h thermal storage are shown in Table 3.9.

Provided that thermal energy is accumulated through 4 h of full-load operation of steam turbine, the heliostat concentration field area and annual power generation of power plant are required to be calculated.

TABLE 3.9 Parameters of Steam Turbine

S/N	Content	Unit	Value
1	Power Range	MW	30–50
2	Sliding Pressure Working Scope (load)	%	30–110
3	Steam Parameter Range	MPa	3–9
4	Rated Power	MW	50
	Main Steam Pressure	MPa	9.2
	Main Steam Temperature	°C	360–383
	Rated Air Inflow	t/h	226

Analysis and solution: Midday of the spring equinox is taken as the design point, solar irradiance takes the value of annual mean solar irradiance of  $750 \text{ W/m}^2$ , design point ambient air temperature takes the value of annual mean ambient air temperature of  $10^\circ\text{C}$ . Output power of collector field at the design point is required to exceed the sum of required input power of generator unit and thermal storage power.

Electricity generation capacity corresponding to the project is 50 MW, and the rated input thermal power is 150 MW.

The rated input storage thermal power is calculated as follows:

Daily required thermal storage =  $4 \text{ h} \times 150 \text{ MW} = 600 \text{ MWh}$ . Assuming the thermal storage working duration is 6 h during the daytime, then the storage thermal power equals  $600 \text{ MWh}/6 \text{ h} = 100 \text{ MW}$ .

150 MW generate power during the daytime directly, another 100 MW using for the night. Required output thermal power from the receiver at the design point can be obtained as

$$150 + 100 = 250(\text{MW}) \quad (3.79)$$

Step I: The required heliostat concentration field area is assumed to be  $100,000 \text{ m}^2$ , and the receiver is cylinder. Based on the concentration field design software, the efficiency of concentration field at the design point can be calculated, which is 68%, and the intercept factor of receiver is 100%.

In this case, output power  $P_{\text{concentrator}}$  of mirror field is:

$$P_{\text{concentrator}} = 68\% \times 100\% \times 100,000 \times 0.75 = 51 \text{ (MW)}$$

According to the method specified in 3.2, the efficiency of receiver can be calculated, which is 90%. In this case, the output  $P_{\text{receiver}}$  of receiver is:

$$P_{\text{receiver}} = 51 \times 90\% = 45.9 \text{ (MW)}$$

Comparing with Eq. (3.79):  $250 \text{ MW}/45.9 \text{ MW} \approx 5.44$ .

Step II: Considering the concentration field area is basically proportional to the output, and the decrease of concentration field efficiency after increase of the scale of concentration field, the concentration field area is reassumed to increase by 5 times and reach up to  $500,000 \text{ m}^2$ . Based on the concentration field design software, the output efficiency of concentration field at the design point can be calculated, which is 63%, and the intercept factor of receiver is 95%.

In this case, the output power  $P_{\text{concentrator}}$  of concentration field is:

$$P_{\text{concentrator}} = 63\% \times 95\% \times 500,000 \times 0.75 = 224.4 \text{ (MW)}$$

According to the method specified in 3.2, the efficiency of receiver can be calculated, which is 85%.

In this case, the output  $P_{\text{receiver}}$  of receiver is:

$$P_{\text{receiver}} = 224.4 \times 85\% = 191 \text{ (MW)}$$

The result is less than 250 MW of Eq. (3.79).

Step III: The concentration field area is reassumed to increase by 35% and reach up to  $675,000 \text{ m}^2$ . Based on the concentration field design software, the output efficiency  $\eta_{\text{hel}}$  of concentration field at the design point can be calculated, which is 62%, and the intercept factor  $\eta_{\text{int}}$  of receiver is 94%.

In this case, the output power  $P_{\text{concentrator}}$  of concentration field is:

$$P_{\text{concentrator}} = 62\% \times 94\% \times 675,000 \times 0.75 = 295 \text{ (MW)}$$

According to the method specified in 3.2, the efficiency  $\eta_{\text{receiver}}$  of receiver can be calculated, which is 84%.

In this case, the output  $P_{\text{receiver}}$  of receiver is:

$$P_{\text{receiver}} = 295 \times 84\% = 247.8 \text{ (MW)}$$

The result is nearly 250 MW in Eq. (3.79), which satisfies the calculation requirement.

From the above, the concentration field area of the power plant is  $675,000 \text{ m}^2$ . After substituting the number into Table 3.1, and calculating term by term, results can be obtained in Table 3.10.

$$\eta_T = \eta_{\text{hel}} \times \eta_{\text{int}} \times \eta_{\text{receiver}} \times \eta_{\text{turbine}} = 62\% \times 94\% \times 84\% \times 30\% = 14.7\%$$

From Fig. 3.45,  $E = 1850 \text{ kWh/m}^2 \times 14.7\% \times 675,000 \text{ m}^2 = 187,310,000 \text{ kWh}$ ; namely the annual power generation approximates 187 million kWh.

Full-load generating hours of the power plant =  $187,310,000 \text{ kWh} / 5 \times 10^4 \text{ kWh} = 3746 \text{ h}$ .

TABLE 3.10 Energy Balance at Example Design Point

S/N	Item	Inputted Power	Lost Power	Residual
1	Solar Irradiance Input to Concentration Field at the design point	$675000 \times 0.75 = 506 \text{ MW}$	0	
2	Concentration Field Loss: Shade, cosine, reflectance, atmospheric transmission loss, receiver intercept factor		211 MW	
3	Inputted Power of Receiver	295 MW		
4	Receiver Loss: Reflection, convection, radiation, conduction		47 MW	
5	Output Power of Receiver			248 MW
6	Input to Thermal storage	$248 \times 98\% = 243 \text{ MW}$		
7	Output of thermal storage and HX			$243 \times 97\% = 236 \text{ MW}$
8	Steam Turbine Input Power	150 MW		
9	Steam Circulation Loss		100 MW	
10	Output Power			50 MW
11	Loss: Auxiliary system consumption and loss (rated operating conditions)		11.1 Steam Turbine 100 kW 11.2 Concentration Field and Communication 20 kW 11.3 DCS 20 kW 11.4 Circulation Pump 2000 kW 11.5 Others 100 kW	2.2 MW
12	Net Output of Power Plant			47.8 MW

### 3.7.3 Thermal Power Plant Capacity Optimization

Thermal power plant system calculation in the previous section has been based on the fact that the capacity of a steam turbine has been specified in advance. Furthermore, an alternative calculation method is that as the generating capacity is the core index to determine the price, it is possible to firstly assume an initial investment and expected price, then the corresponding annual generating capacity can be inversely deduced based on these two factors. As the annual generating capacity is relevant to the system efficiency, after determining the generating capacity, it is also possible to calculate the annual generating efficiency based on local meteorological conditions.

In case of the power price of the power plant being considered as a modifiable quantity, technical and economic optimization for the power plant can also be conducted according to the method shown in Fig. 3.47, and a reasonable power price can be obtained.

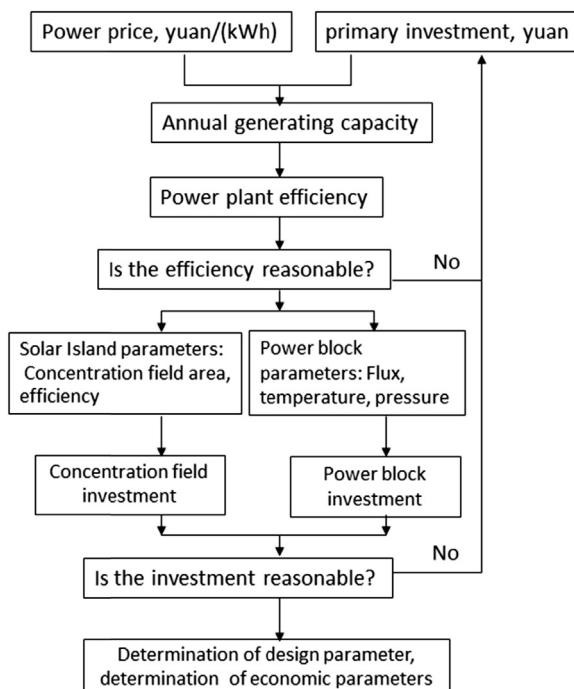


FIGURE 3.47 Power plant technical and economic optimization method.

### 3.7.4 Power Generation Calculation Methods Based on Hourly Simulation

The key point of this method is that the hourly solar irradiance and meteorological conditions data are necessary. Through the simulation on the basis of system energy balance, relationships between the collector field output and rated input of a steam turbine corresponding to different concentration field areas can be calculated, so that the annual maximum generating capacity corresponding to the steam turbine capacity can be obtained, and the "optimum concentration field area," thermal storage, auxiliary boiler capacity, etc. can be determined respectively. The "optimum concentration field area" refers to the power plant determined according to the constructed capacity of a certain area. Such concentration field area configuration intends to maximize the annual generating capacity of the power plant.

By applying this method, comparing with the design point method, more abundant information can be obtained, such as energy distribution among different units of the power plant system under various kinds of meteorological conditions; logical connection among various units, which serves as the foundation of power plant DCS preparation; energy flow and control information flow among various units during power plant initiation, standby, and stoppage, which are extremely important for process design. As the design point method corresponds to the typical hours in a year and typical meteorological conditions, in fact, it is merely to calculate a "typical point."

Simulation software that has been broadly applied right now is TRNSYS, which is capable of analyzing system principles, system composition, component model, operating mode, operating status, control logic, etc. In order to facilitate the reader on understanding this process, principle system of Beijing Badaling Experimental CSP plant at IEE-CAS has been established in this section and is shown in [Fig. 3.48](#). The corresponding full system simulation TRNSYS model is shown in [Fig. 3.49](#).

Simulation model of the system mainly consists of the meteorological module (Type15-2), heliostat concentration field module (FeffMatx, Type394), receiver module (CenRec, Type395), high- and low-temperature thermal storage module (Type 5b, Tank-Type 14) and steam turbine module of Rankine Cycle (Stage, Type 318), condenser, deaerator, various kinds of pump and generator modules. This section mainly introduces the approximate method of system simulation. The specific modeling process for the mathematical models of the above modules and basic mutual coupling logics will not be described here.

By applying the HOC (the heliostat optical code of IEE-CAS) software, as shown in [Fig. 3.50](#), heliostat concentration field of Badaling power plant

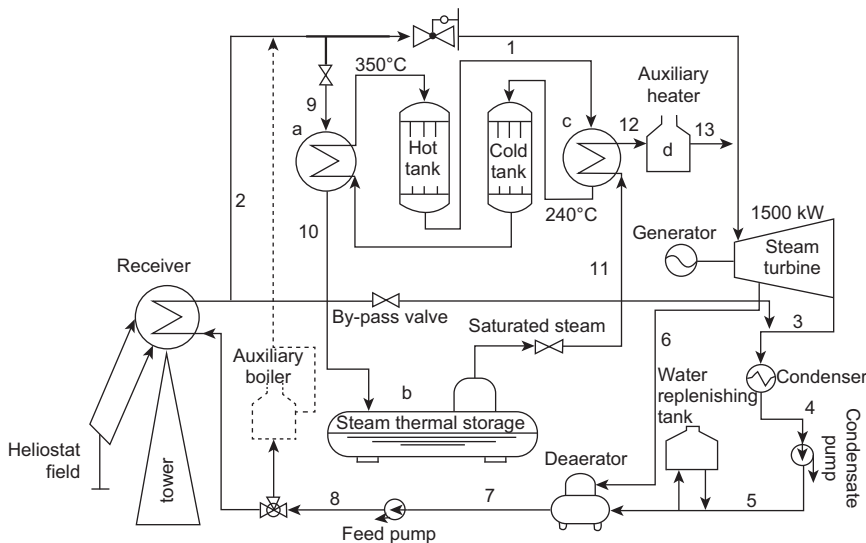


FIGURE 3.48 Principle thermal system of Badaling power plant (numbers in the figure refer to serial number of flow passage).

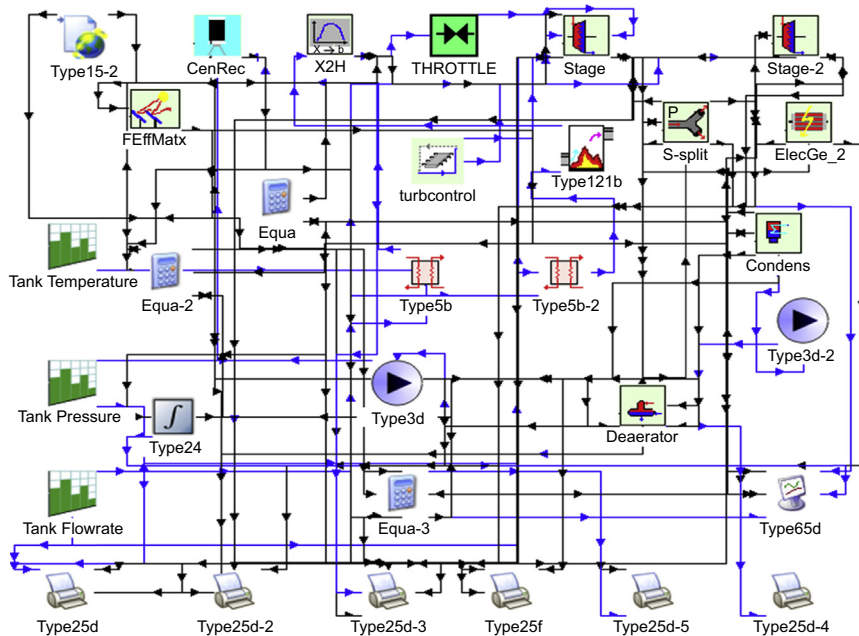
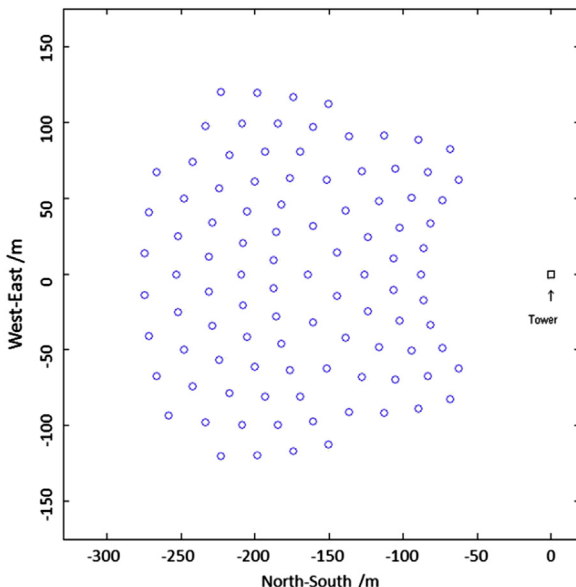


FIGURE 3.49 Full system simulation TRNSYS model of Badaling power plant.



**FIGURE 3.50** One layout of heliostat concentration field of Badaling power plant (sector radial-staggered layout of concentration field).

**TABLE 3.11** Major Parameters of Heliostat Concentration Field of Badaling Power Plant

Location	40.4°N, 115.9°E	Layout of Heliostat Concentration Field Optical Efficiency	Radial-staggered pattern
Heliostat Surface Profile	Ideal sphere	Ring 1 and Tower Spacing Coefficient	1
Annual Mean Optical Efficiency of Concentration Field	66.6%	Rated of Concentration Field at the design point	81.72%
Length and Width of Mirror Surface of One-sided Heliostat	10m × 10 m	Heliostat Number	100 pieces

has been established. Various kinds of design parameters and efficiency calculation results of the concentration field are shown in [Table 3.11](#).

[Figs. 3.51 and 3.52](#) show the solar thermal collection part of power plant simulated on the basis of [Fig. 3.49](#) [31]. The relationship between thermal power concentrated by heliostat concentration field onto the surface of aperture of receiver (Curve 1 in the figure) and DNI (Curve 2 in the figure)

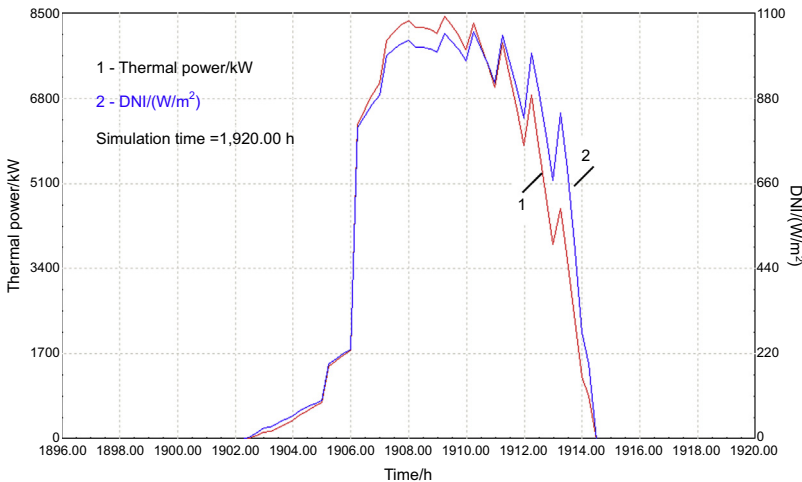


FIGURE 3.51 Relationship between the concentration power projected by heliostat concentration field onto the receiver and direct normal irradiance on the spring equinox.

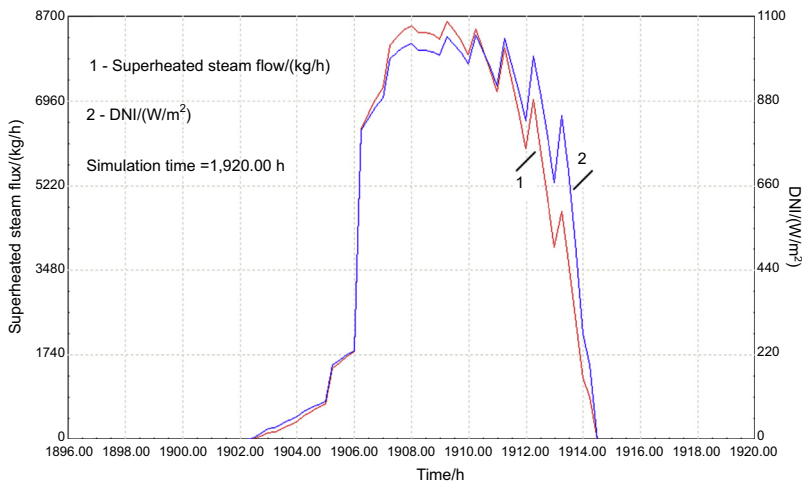


FIGURE 3.52 Relationship between the outlet superheated steam flow of receiver of Badaling power plant and direct normal irradiance on the spring equinox.

can be calculated, which is shown in Fig. 3.51. Under the premise of the inlet and outlet temperatures being set, the relationship between the outlet superheated steam flux of receiver (Curve 1 in the figure) and DNI (Curve 2 in the figure) is shown in Fig. 3.52.

The relationship between the whole-day generating capacity (Curve 1 in the figure) and solar DNI (Curve 2 in the figure) is shown in Fig. 3.53.

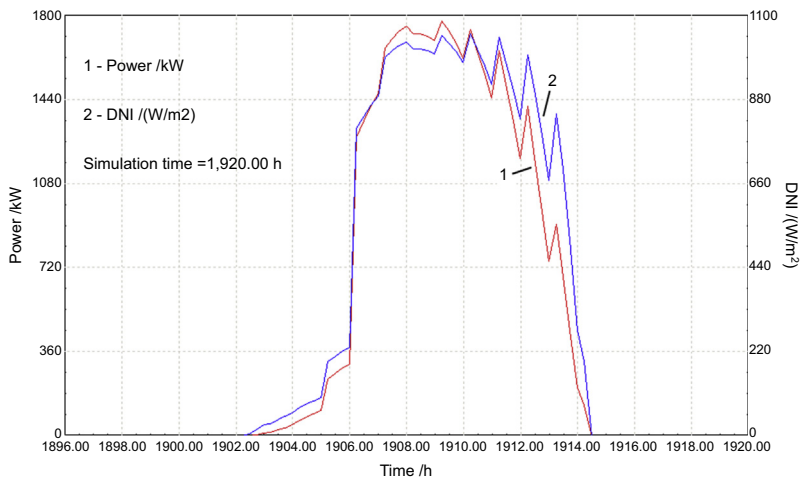


FIGURE 3.53 Relationship between generating capacity of Badaling power plant and direct normal irradiance on the spring equinox.

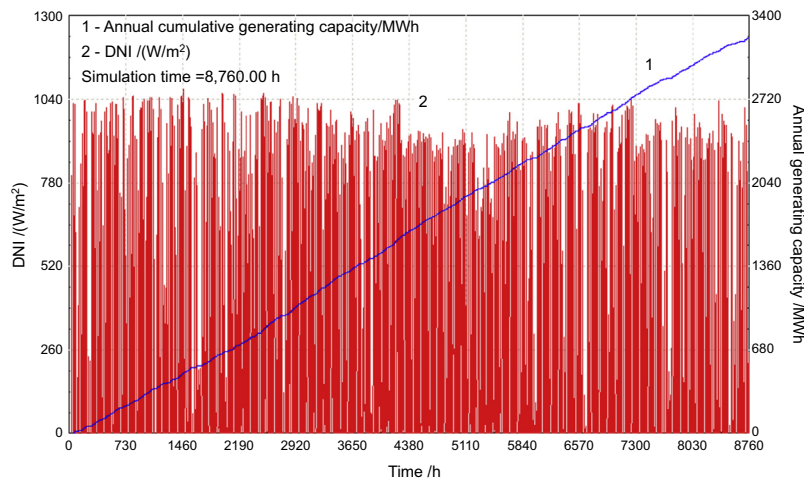


FIGURE 3.54 Relationship between the annual generating capacity and daily solar direct normal irradiance of Badaling power plant.

As shown in Fig. 3.54, by utilizing the hourly meteorological data, annual generating capacity of Badaling CSP plant has been analyzed and researched. The figure has indicated the annual cumulative generating capacity, as shown in Curve 1 in the figure. Curve 2 refers to the annual hourly DNI.

Relationships between outlet steam thermal variation, outlet steam pressure variation, temperature variation of steam thermal storage in the

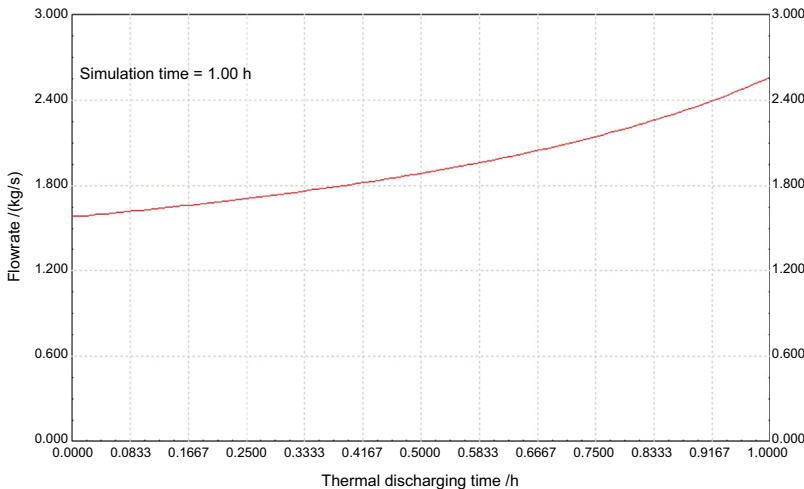


FIGURE 3.55 Variation of outlet steam flow of steam thermal storage along with thermal discharging time.

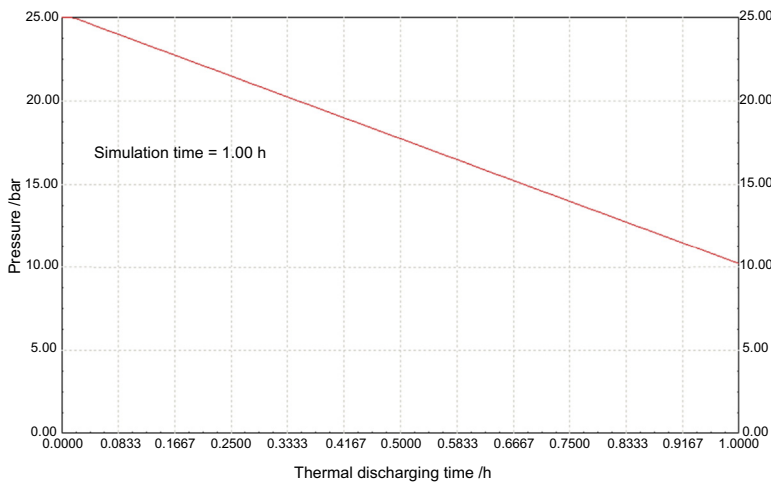
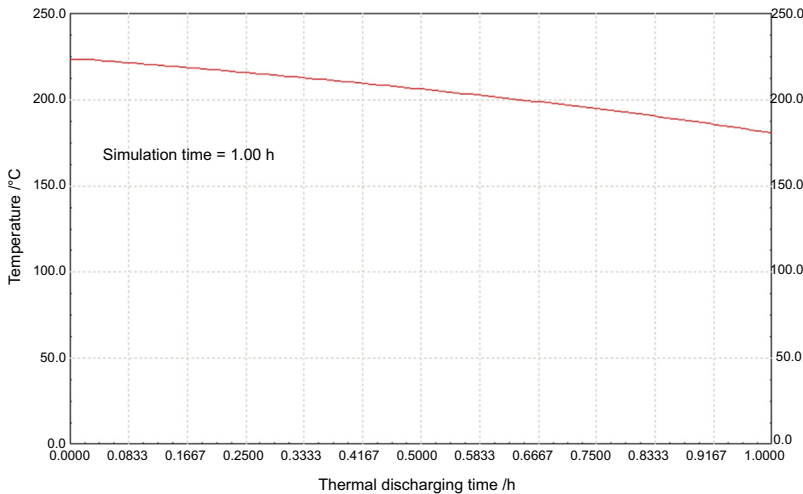


FIGURE 3.56 Variation of outlet steam pressure of steam thermal storage along with thermal discharging time.

thermal storage system, and thermal discharging time have been separately shown in Figs. 3.55–3.57 [31]. The designed thermal charging and discharging time is 1 h; therefore, in Figs. 3.55–3.57, the designed time on the horizontal axis is 1 h.

At the design point of the Badaling power tower plant (namely 12:00 on the midday of the spring equinox, DNI = 1000 W/m<sup>2</sup>), major thermodynamic parameters calculated based on the above values of



**FIGURE 3.57** Variation of outlet steam temperature of steam thermal storage along with thermal discharging time.

various spots of Badaling power plant indicated in Fig. 3.48 are as follows: The selected steam turbine's relative internal efficiency is assumed to be  $\eta_{ri} = 0.8$ , mechanical efficiency  $\eta_m = 0.98$ , and generator efficiency  $\eta_g = 0.98$ . Through calculation, various parameters can be obtained, including steam turbine inlet superheated steam pressure  $P'_{in} = 2.354$  MPa, steam turbine inlet superheated steam temperature  $T'_{in} = 390^\circ\text{C}$ , and steam turbine final outlet exhaust pressure  $P'_{out} = 0.0073$  MPa. As shown in Fig. 3.48, steam turbine intermediate extraction pressure  $P_b = 0.3$  MPa. According to the definition of the relative internal efficiency  $\eta_{ci}$  of steam turbine and the water/steam diagram, thermodynamic parameters corresponding to various points indicated in Fig. 3.48 can be obtained as follows:

Point 1

$$p_1 = p'_{in} = 2.354 \text{ MPa}, \quad T_1 = T'_{in} = 390^\circ\text{C}, \quad h_1 = 3220.1 \text{ kJ/kg}, \\ s_1 = 7.014 \text{ kJ/(kg}\cdot\text{K});$$

Point 3

$$p_3 = p'_{out} = 0.0073 \text{ MPa}, \quad T_3 = T'_{out} = 39.784^\circ\text{C}, \quad h_3 = 2390.684 \text{ kJ/kg}, \\ s_3 = 7.677 \text{ kJ/(kg}\cdot\text{K});$$

Point 6

$$p_6 = 0.3 \text{ MPa}, \quad T_6 = 183.2^\circ\text{C}, \quad h_6 = 2831.27 \text{ kJ/kg}, \quad s_6 = 7.239 \text{ kJ/(kg}\cdot\text{K})$$

Feed water in Fig. 3.48 is assumed to pass through the condensate pump, the thermodynamic parameters of point 5 at deaerator inlet are as follows:

$$p_5 = 0.12 \text{ MPa}, \quad T_5 = 41^\circ\text{C}, \quad h_5 = 171.82 \text{ kJ/kg}, \quad s_5 = 0.586 \text{ kJ/(kg}\cdot\text{K})$$

Feed water design parameters of point 7 at deaerator outlet are as follows:

$$p_7 = 0.12 \text{ MPa}, \quad T_7 = 104.0^\circ\text{C}, \quad h_7 = 435.99 \text{ kJ/kg}, \quad s_7 = 1.352 \text{ kJ/(kg}\cdot\text{K)}$$

Steam turbine final outlet exhaust at point 3 in Fig. 3.48 enters into the condenser and experiences the 3-4 constant-pressure cooling process in the condenser, in which steam is cooled and completely condensed into saturation water through phase change while discharging thermal; water from the environment is used as the refrigerant. From the above, thermodynamic parameters of point 4 in Fig. 3.48 are as follows:

$$p_4 = 0.0073 \text{ MPa}, \quad T_4 = 39.78^\circ\text{C}, \quad h_4 = 166.64 \text{ kJ/kg}$$

So far, the entire thermodynamic process has been successfully simulated. From the above, by applying this thermodynamics-based method, calculation of the annual generating capacity can be accomplished. Furthermore, other parameter groups that are comparatively comprehensive can be obtained as well. Whereas by applying the design point method, only system energy parameters corresponding to one time point can be calculated, and the mathematical model is steady state model.

### 3.7.5 Influences of Location on Calculation of Parabolic Trough Collector Efficiency

Two definitions of transient efficiency of parabolic trough collector:

$$\eta_{DNI} = \frac{\dot{Q}}{DNI \times A}$$

$$\eta_{Gbp} = \frac{\dot{Q}}{G_{bp}A}$$

Efficiencies calculated based on these two definitions vary significantly. Considering cosine influences,  $\eta_{Gbp}$  is used in order to precisely reflect the actual thermal energy.

A calculation example on the efficiency of parabolic trough collector has been provided in this section by selecting three locations:

Badaling, Beijing ( $40^\circ22'N, 115^\circ56'E$ );

Sanya, Hainan ( $18^\circ15'N, 109^\circ30'E$ );

Hohhot, Inner Mongolia ( $41^\circN, 111^\circ45'E$ )

Annual mean efficiencies of parabolic trough collector in above areas can be calculated, from which, it can be concluded that different geographic locations have resulted in different incidence angles; influences of latitude on the efficiency can also be seen. The local solar hour is assumed to be 8:00–16:00 and the annual mean DNI of three locations is

the same fixed value (such as  $800 \text{ W/m}^2$ ). Parabolic trough collectors have been arranged on the north-south axis, with a length of 100 m. Collector's output power  $\dot{Q}$  is constant, and the efficiency of collector in case of solar normal incidence is 60%.

According to the assumption,  $\eta_{Gbp} = 60\%$ , and based on

$$G_{bp} = DNI \times \cos(\theta) \left[ 1 - \frac{f}{L} \tan(\theta) \right]$$

it can be further deduced, that  $\eta_{DNI} = \frac{\dot{Q}}{DNI \times A} = \frac{\eta_{Gbp} G_{bp}}{DNI} = \eta_{Gbp} \cos(\theta) \left[ 1 - \frac{f}{L} \tan(\theta) \right]$

The incidence angle is assumed to remain unchanged within each minute.

1. Cosine value of daily maximum incidence angle, which is shown in [Fig. 3.58](#).
2. Cosine value of daily mean incidence angle, which is shown in [Fig. 3.59](#)
3. Daily cosine value variation on a typical day, which is shown in [Fig. 3.60](#), in which 172, 266, and 356 separately refer to the summer solstice, autumnal equinox and winter solstice.
4. Annual mean corrected value of beam incidence angle
  - a. Badaling

$$\cos(\theta) \left[ 1 - \frac{f}{L} \tan(\theta) \right] = 0.8013$$

Then

$$\eta_{DNI} = \eta_{Gbp} \cos(\theta) \left[ 1 - \frac{f}{L} \tan(\theta) \right] = 0.6 \times 0.8013 = 0.4808$$

b. Sanya

$$\cos(\theta) \left[ 1 - \frac{f}{L} \tan(\theta) \right] = 0.9209$$

Then

$$\eta_{DNI} = \eta_{Gbp} \cos(\theta) \left[ 1 - \frac{f}{L} \tan(\theta) \right] = 0.6 \times 0.9209 = 0.5525$$

c. Hohhot

$$\cos(\theta) \left[ 1 - \frac{f}{L} \tan(\theta) \right] = 0.7971$$

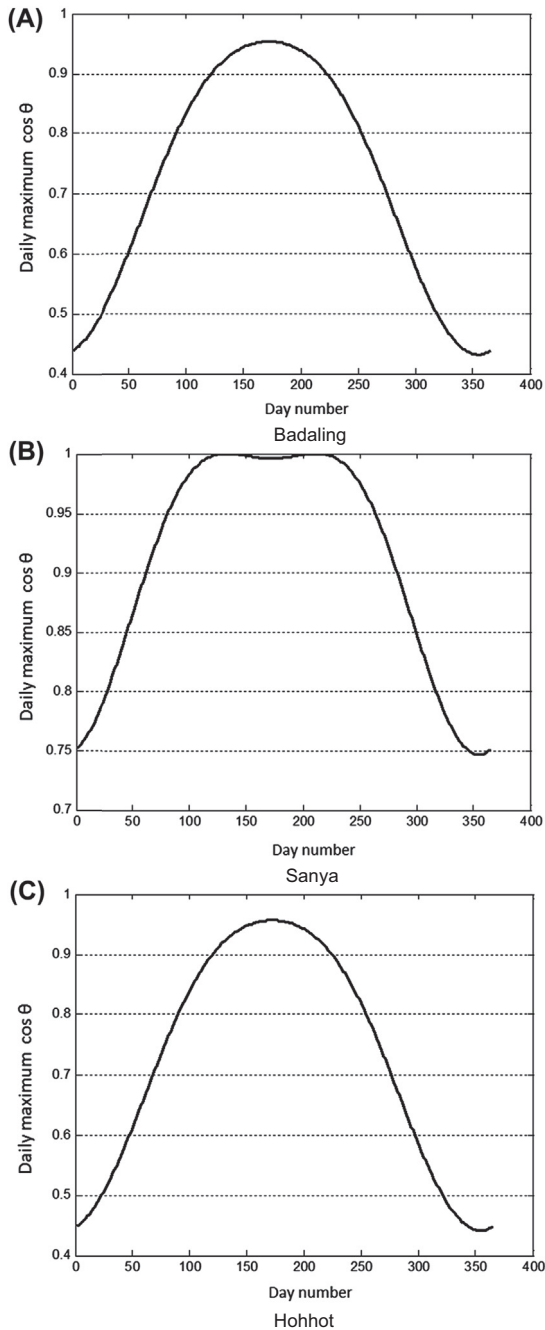


FIGURE 3.58 Cosine value of daily maximum incidence angle.

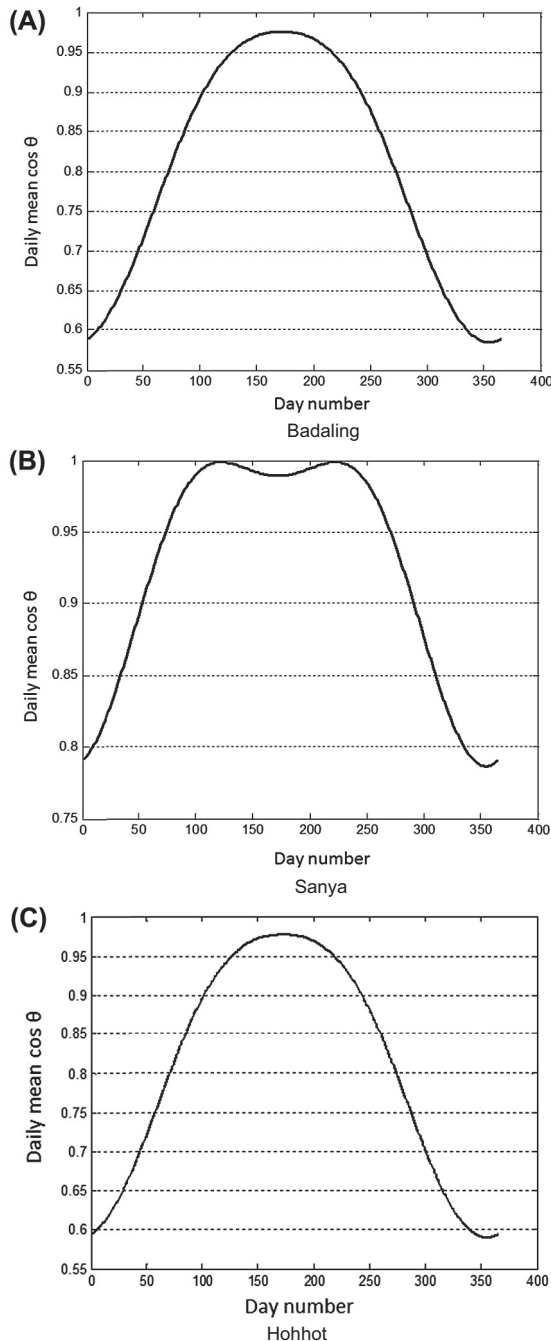


FIGURE 3.59 Cosine value of daily mean incidence angle.

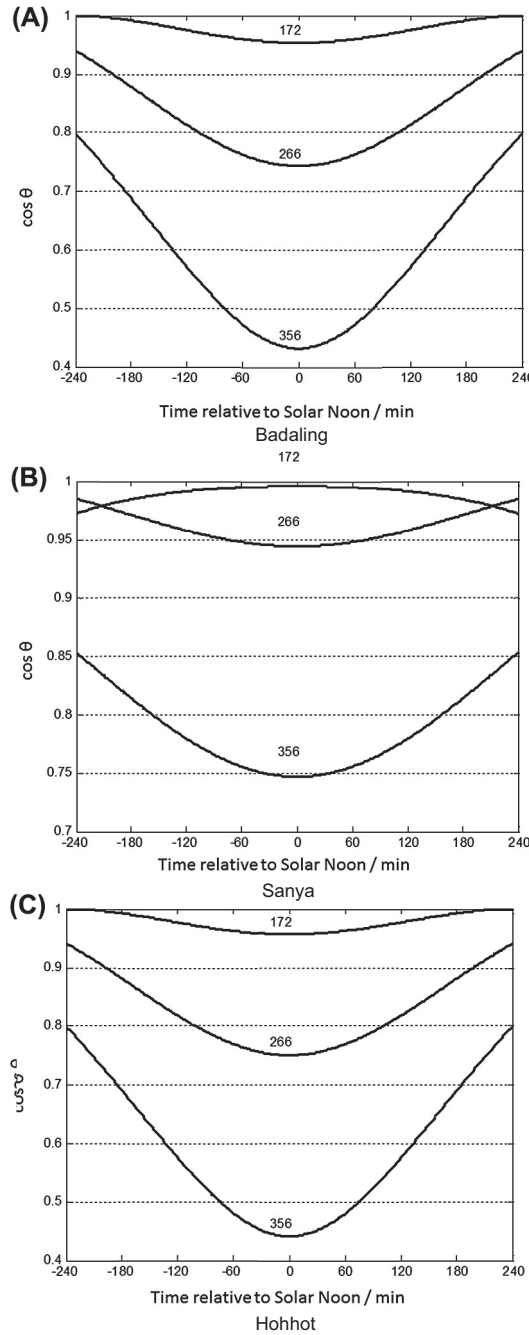


FIGURE 3.60 Daily cosine value variation on a typical day.

Then

$$\eta_{DNI} = \eta_{Gbp} \cos(\theta) \left[ 1 - \frac{f}{L} \tan(\theta) \right] = 0.6 \times 0.7971 = 0.4782$$

Badaling is close to Hohhot in latitude, thus the respective calculation results are almost the same.

### 3.8 DETERMINATION OF THERMAL STORAGE RESERVE

Thermal storage mainly aims at guaranteeing the stable and continuous operation of power plant, so as to satisfy the request of power grid and achieve the maximum economy.

#### 3.8.1 Principles of Selecting Thermal Storage Capacity

Determination of thermal storage mainly depends on the distribution of feed-in tariff against time and the requirement of power grid on peak modulation. Duration of thermal storage shall be merely determined by the full-load generating hours in sunless intervals and economy of power price. As great investments are involved, it must be calculated on a prudent basis.

Step I: Preliminary determination of thermal storage period according to the feed-in tariff and time difference of sunset.

[Fig. 3.61](#) has indicated that time interval with high power price after sunset is more or less 6 h. Thus thermal storage period can be preliminarily set as 6 h.

However, due to the application of thermal storage system, initial investment may be increased, and the generating cost of power plant may grow. Thus it is necessary to conduct Step II.

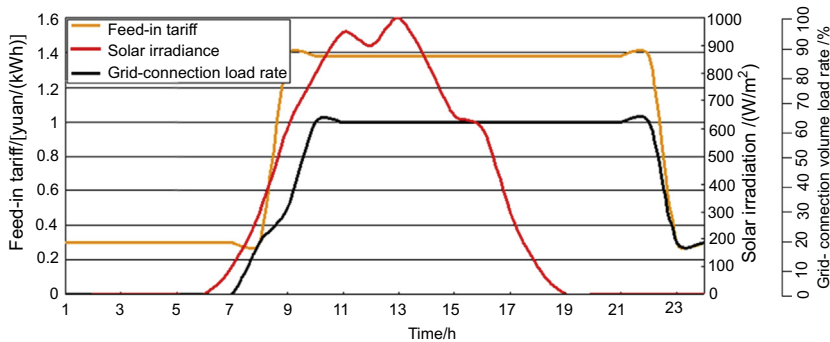


FIGURE 3.61 Determination of thermal storage period.

Step II: Calculation of influences of different thermal storage periods on generating cost.

The value of the thermal storage period direct influences on the variation in the initial investment cost of the solar power plant, which further influences the variation of generating cost. Fig. 3.62 displays the variation of leveledized cost of electricity (LCOE) under different thermal storage periods in a 50 MW parabolic trough CSP plant located in Ordos, China, in which along with the increase of thermal storage period, LCOE of the power plant drops. When the thermal storage period of the power plant in this case is 10 h, the respective power price can reach the minimum level.

Value of this minimum level mainly depends on the power plant capacity, primary investment on the thermal storage unit and local solar irradiation resources.

To sum up, based on the above analysis, setting thermal storage period of the power plant as 6 h is determined to be economically efficient, which is able to help reduce the power price. So, is it necessary to further increase the thermal storage period? According to Fig. 3.62, LCOE corresponding to the thermal storage period of 6 h is 1.32 yuan/(kWh); in this case, grid purchase price of the power plant indicated in Fig. 3.61 is 1.38 yuan/(kWh); after exceeding this time interval, namely starting from 22:00, the grid purchase price decreases to 0.30 yuan/(kWh). Thus it makes no sense to further increase the thermal storage period. According to Fig. 3.61, LCOE still can be reduced, but the feed-in tariff has exceeded 0.30 yuan/(kWh).

In case that it is necessary to optimize power price in terms of thermal storage period, such as the power price bidding project, for the case shown in Fig. 3.62, it is obviously conductive by setting the thermal storage period as 10 h of full-load power generation of a steam turbine.

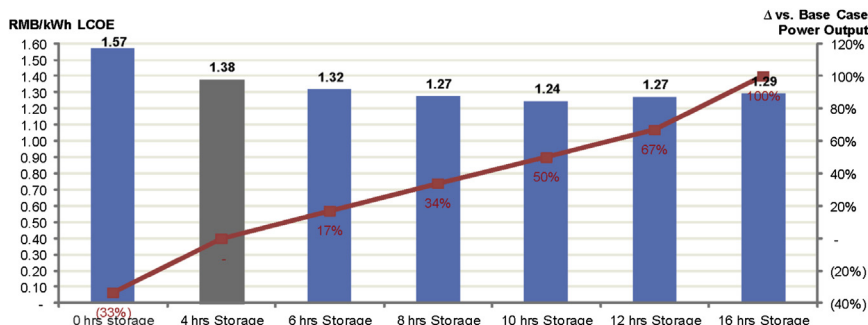


FIGURE 3.62 Relationship between thermal storage period and LCOE. Data Source: "China Solar Thermal Power Industry Research Report 2013," China National Solar Thermal Energy Alliance.

### 3.8.2 Principles of Selecting Thermal Storage Capacity

Thermal charging and discharging power of thermal storage shall be equivalent to the output power of collector field and input power of a steam turbine. Output power of collector field at the design point is equivalent to the sum of rated input thermal power of a steam turbine and the transient thermal storage power. However, input power of thermal storage still has been designed according to the maximum thermal charging power, and the thermal discharging power has been designed according to the maximum load requirement of a steam turbine.

When calculating thermal storage capacity solar multiple acts as an important concept, which comes from concentration field. In case of considering the concentration field while supplying power to the steam turbine and thermal storage, area of concentration field at the design point must be considered to be large enough. Relationship between thermal storage and receiver has been given in [Sections 3.7.1 and 3.7.4](#). While in [Section 3.7.4](#), the more precise value of thermal storage can be obtained by applying TRNSYS, and also, the thermal storage unit can be designed and the respective working status can be understood. In addition, during design of thermal storage, self-consumed energy of thermal storage unit must be considered as well, including fossil fuel backup and synthetic oil or molten-salt anti-coagulation measures.

## **3.9 MAIN POINTS FOR POWER PLANT SITE PLAN**

The overall planning can be conducted based on the location of urban areas, meteorological conditions, access route connection, HV outlet, water source, road, land coverage of concentration field and other external conditions as well as features of the plant area by integrating with specific concentrating power generation process, in which the following points shall be specified: power plant capacity, concentration field layout, steam generating area, thermal storage area, conventional generating area, location and transportation of the power plant, HV outlet orientation and passageway, water source of power plant, fuel transportation, drainage of power plant, power plant general layout and general elevation planning factors.

1. Power plant capacity. Current scale and reserved scale for site expansion shall be determined, especially for the concentration field; when the site is arranged, long-distance transmission losses of high temperature fluid and wind direction shall be considered. For a power tower plant, necessary site conditions for receiver tower installation and receiver maintenance service shall be considered.

2. Concentration field layout. Concentration field has the largest land coverage in an CSP plant. Normally, area of a heliostat concentration field is five times the sum aperture area of heliostats. Land coverage of a parabolic trough concentrator is about three times the total area of aperture of receiver of a parabolic trough concentrator.

In general cases, except for the efficiency of concentration field, fluid transportation-related problems shall also be considered during the layout of concentration field, especially the layout of parabolic trough concentration field.

An example of concentration field layout in a 50 MW parabolic trough power plant is shown below. In terms of parabolic trough thermal collection, solar radiations are concentrated in the primary loop and converted into thermal through the collector consisting of a parabolic trough concentrator with the concentration ratio of 75 times and a evacuated tube receiver; the respective heat-transfer medium is synthetic oil with the working temperature of 400°C. The secondary loop is for oil-water heat exchange, which produces superheated steam in order to drive the highly efficient steam turbine to work and generate power. A solar collector field consists of 160 parallel “thermal collection loops”; each “thermal collection loop” consists of four rows of parabolic trough “collector units” with a length of 150 m ([Fig. 3.63](#)) through series combination, which is shown in [Fig. 3.64](#). Length of thermal collection loop is determined by the solar irradiation and meteorological conditions of the working site of collectors. Normally the temperature increase of outlet/inlet loops of synthetic oil is 105°C.



FIGURE 3.63 A parabolic trough collector unit with a length of 150 M [32].

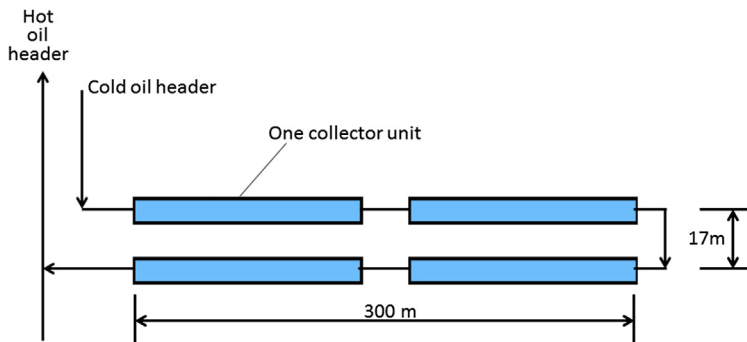


FIGURE 3.64 Parabolic trough collector loop.

Center-to-center distance between collector units in the thermal collection loop is normally three times of the width of aperture of parabolic trough concentrator. For example, in case of the width of aperture of concentrator being 5.7 m, the center-to-center distance shall be about 17–20 m.

Layout of power tower concentration field will be explained in details in [Section 4.2](#). Normally, there are two ways, namely the northward concentration field and encircled concentration field.

[Fig. 3.65](#) displays an example of the northward concentration field.

3. Steam generating area. A steam generating area includes such major equipment as feed water preheater, evaporator, superheater, and reheater. In case of the heat-transfer medium



FIGURE 3.65 Concentration field of PS10 power tower plant in Spain [32].



FIGURE 3.66 Molten-salt/steam generator of achimide power plant, Italy [2].

being fluid, like synthetic oil, molten salt, or air, it is possible to transmit the heat within the area from the primary loop to the feed water facilities in the secondary loop through a heat exchanger in order to produce qualified superheated steam, and drive the generator unit of a steam turbine to work (refer to Fig. 3.66).

4. Thermal storage area. Currently, thermal storage medium of the large-scale power plant is normally molten salt. A thermal storage system includes such major equipment as cold molten-salt storage tank, hot molten-salt storage tank, cold molten-salt circulating pump, hot molten-salt circulating pump, and oil-salt heat exchanger. Due to the high temperature of thermal storage area, space and access for emergency measures taken in case of any leakage shall be reserved, which shall be placed at the downwind area of the power plant. In the case that the distance of fluid entering into the thermal storage tank is too long, it may result in great heat losses; based on this point, thermal storage area shall not be located far away from the thermal collection area. For a parabolic trough power plant, it should be specially noted that headers connecting various outlets of thermal collection loops shall not be located too far away from the thermal storage area. Receiver of the power tower plant has been close to the thermal storage, thus the transmission distance is not a huge problem.
5. Conventional generating area. As shown in Fig. 3.67, it is an example of a power plant in Spain, according to which, partial generating units have been mounted in the middle of the concentration field.



FIGURE 3.67 Generating unit layout of Andasol-I power plant, Spain [32].

6. Location and transportation of the power plant. Identification of location of traffic hub and the distance between the traffic hub and the high-grade highways corresponding to the proposed power plant is of great significance to power plant construction. Due to the access of large-scale overheight and overweight equipment, like the thermal storage tank, steam turbine, and boiler, roads are required to have strong carrying capacities; due to the transportation of a large quantity of glass reflectors, roads are required to have high evenness. Thus grade of road, as well as dimension of roads and bridges along the line, shall be given special attention to; otherwise, it may lead to great expenses during infrastructure construction.

Upwind area of power plant shall be free of large-scale air pollution sources; otherwise, mirrors will be contaminated by dusts.

7. HV outlet orientation and passageway. Diagrams and texts for receiving station of power plant outlet, conditions of cable passageway, conditions of power outlet, etc. shall be provided.
8. Water source of power plant. Name and distance of the water supplier shall be specified, as well as the respective daily water supply capability, water price description, actual daily water supply and annual total water supply.
9. Fuel transportation. Transportation method for engineering liquid, gas or solid fuels, distance between the fuel supply point and the plant area, whether there is any road of the appropriate grade in Gobi areas for transportation; road with an uneven surface may cause danger to fuel transportation.

10. Drainage of power plant. Drainage of a solar power plant includes production water supply and domestic water supply. As the amount of water for washing the surfaces of concentrators is insignificant, site drainage can be neglected. Normally, for power plants located in Gobi areas and deserts, rainwater can be drained off in natural ways. After being treated, power condenser water can be used for irrigation and for washing mirror surfaces.
11. Power plant general lay-out planning factors. A thermal power plant normally consists of four sections, including the collector field, thermal storage area, generating area and office area.

A collector field contains both solar concentrator and thermal receiver; dimension of the concentration field shall be indicated on the general layout. For a parabolic trough system, combination pattern of thermal collection units shall be indicated, such as the quantity of units in order to constitute a fluid serial loop, and the quantity of loops in order to constitute a power plant concentration field through parallel connection. As the heliostat, concentration field layout drawing shall be prepared. The concentration field can use a northward sector layout or circumferential circular/oval layout. Position and height of receiver tower shall be marked on the concentration field drawing accordingly.

Core area of a power plant normally consists of the main powerhouse, control room, thermal storage area, power tower, etc.

The entire plant area layout shall be based on the process requirements and architectural function division while fully utilizing the limited land within the plant area.

A plant area consists of two sections, the concentrator field and the generating area. Due to large landscape in the concentration field that cannot be combined into the floorage, it shall be considered accordingly when calculating the floor area ratio of the power plant; otherwise, it may result in the conflict between it and the floor-area ratio of construction land required by the state in regulations and norms. It shall be calculated based on the forestation of the power plant and land coverage of the generating area.

12. Power plant general elevation planning factors. The concentration field of a tower power plant does not have strict requirement on the site evenness; even the slope of mountains can be utilized wisely to facilitate concentration field layout, which is very conductive for taking advantage of the mountain resources in China. For the concentration field of a parabolic trough power plant, due to the flow passage consisting of the evacuated tubes and requirements

on tracking, slope of installation site of a parabolic trough concentrator is required to be not more than 1%. Normally, in the concentration field of power plant located in the northern area of China, it is not necessary to design a drainage ditch.

A power tower plant normally uses the horizon of the receiver tower as the zero elevation, and center of the tower as center of the heliostat concentration field. For a northward concentration field, in case of being a highland to the south of the concentration field, it will facilitate the reduction of building height of the receiver tower.

It is also possible for a power tower plant to mount all equipment within the tower in order to save land. As shown in Fig. 3.68, interior of the receiver tower contains all parts except for the heliostat concentration field of the power plant (thermal receiver, thermal storage, steam generation, power generation). Such layout pattern has great reference value for the construction of a power plant while saving land. Of course, due to the increase of load, building costs of the tower will be increased; yet for areas with comparatively higher prices for land use, such layout pattern can be applied.

Concentration field of a parabolic trough power plant has a strict requirement on land evenness; the standard horizon of the entire plant area can be selected to be consistent with the horizon elevation of the concentration field. In case of concentration field wind wall being designed in the power plant, special attention shall be paid to the design



FIGURE 3.68 Solar tower and heliostats of the power tower plant of the Korean Institute of Energy Research (Located in DAEGU, Korea, October 2011).

of the shape, height of the wall, and the distance between the wall and the concentration field; otherwise, the negative pressure area created by the wind striding over the wall may aggravate the dust accumulation in the concentration field.

### **3.10 NOTICES FOR CONCENTRATION FIELD LAYOUT**

A concentration field serves as the unit for collecting, reflecting, and concentrating solar energy. During design of a heliostat field, attention shall be paid to the harms to its neighboring buildings and personnel. It is better not to construct any tall buildings on other directions around the tower besides the north direction in the concentration field.

Road layout in the concentration field and the space between concentrators shall be designed by considering the service request of equipment. For large-area heliostats, requirements for 20 t-level crane car land and road widths shall be fully considered; whereas for small-area heliostats, less large-scale transportation equipment is required for erection and hoisting. However, due to large quantity of mirrors, multiple linkage mechanisms and numerous fault points, the space necessary for frequent service shall also be fully considered.

Concentrator in the concentration field has extremely high requirement on precision; a slight shaking may have an impact on the precision. Thus when analyzing the geological conditions of the concentration field, construction site shall be free of significant geologic hazards, such as earthquake and underground cave collapse. It shall be fully considered during the foundation design for the concentrator and receiver tower.

Diameter and volume of the receiver tower shall be as small as possible. It is better to apply the scheme of steel structure tower that is permeable to light, which could minimize the shade caused the tower during functioning of the northward concentration field.

Communication and power cables in the concentration field shall be rat-proof. By using rat-proof heavy-armored cables, cable costs will be greatly increased. For areas with severe rat problems, it is suggested to apply wireless communication to achieve the connection between the concentration field and the host computer.

For a parabolic trough system, the concentration field has been integrated with the collector field; thus soil pollution caused by evacuated tube oil leakage and the respective safety preventive measures shall be fully considered. In order to facilitate the treatment for oil leakage and prevent the spilled materials from being spread, it is normally not suggested to perform any concrete or asphalt hardening on the ground

below the parabolic trough concentrators, so as to facilitate the timely replacement of contaminated soil.

Due to the short distance to the ground, and small wind resistance of concentrator, FRESNEL concentrator can be arranged without considering the introduction of wind resistance facilities while the receiver tubes over the reflectors should be considered with wind resistance.